FINAL REPORT

For

Contract No. NAG2-908

Title: Development of a Composite Tailoring Procedure for Airplane Wings

Principal Investigator: Dr. Aditi Chattopadhyay
Arizona State University
Mechanical and Aerospace Engineering

1. Introduction

The quest for finding optimum solutions to engineering problems has existed for a long time. In modern times, the development of optimization as a branch of applied mathematics is regarded to have originated in the works of Newton, Bernoulli and Euler. Venkayya has presented a historical perspective on optimization in [1]. The term 'optimization' is defined by Ashley [2] as a procedure "...which attempts to choose the variables in a design process so as formally to achieve the best value of some performance index while not violating any of the associated conditions or constraints". Ashley presented an extensive review of practical applications of optimization in the aeronautical field till about 1980 [2]. It was noted that there existed an enormous amount of published literature in the field of optimization, but its practical applications in industry were very limited. Over the past 15 years, though, optimization has been widely applied to address practical problems in aerospace design [3-5].

The design of high performance aerospace systems is a complex task. It involves the integration of several disciplines such as aerodynamics, structural analysis, dynamics, and aeroelasticity. The problem involves multiple objectives and constraints pertaining to the design criteria associated with each of these disciplines. Many important trade-offs exist between the parameters involved which are used to define the different disciplines. Therefore, the development of multidisciplinary design optimization (MDO) techniques, in which different disciplines and design parameters are coupled into a closed loop numerical procedure, seems appropriate to address such a complex problem. The

importance of MDO in successful design of aerospace systems has been long recognized. Recent developments in this field have been surveyed by Sobieszczanski-Sobieski and Haftka [6].

1.1 Multidisciplinary Design Optimization of Smart Composite Wings

The use of multidisciplinary optimization techniques in aircraft design has been increasing over the past decades. A recent survey of MDO applications in preliminary aircraft design has been presented by Kroo [7] . The analysis methods used in MDO range from simple analytical or empirical expressions to complex finite element models [8-11]. The validity of the designs obtained using MDO procedures depends strongly upon the accuracy of the analytical methods used. Therefore, it is essential to integrate accurate and efficient analysis techniques to obtain meaningful optimum designs.

Due to the high stiffness-to-weight ratio and directional stiffness and strength properties offered by advanced composites, they are increasingly being used in aircraft wing design. The deformation of the wing under load is directly related to the stacking sequence of the orthotropic composite laminae. Hence, for aircraft wings made out of composite materials, aeroelastic tailoring presents an opportunity to enhance structural, aerodynamic and control performance by utilizing their unique stiffness and strength properties. A comprehensive review of the aeroelastic tailoring technology was presented by Shirk *et al.* [12]. It was noted that aeroelastic tailoring has matured as a result of developments in composite material analysis and optimization techniques. Since aircraft wing design is a multidisciplinary problem involving the coupling of various disciplines such as aerodynamics, composite structural analysis, dynamics and

aeroelasticity, the use of MDO techniques seems appropriate. Key elements associated with the use of MDO in wing design are the development of sophisticated optimization techniques and accurate analysis methods.

1.1.1 Optimization Techniques

The design of composite wings to achieve high flutter and divergence speeds while maintaining a low structural weight and stresses within allowable limits, is a truly multidisciplinary problem. A number of optimization procedures have been developed for minimum weight design of wing structures with aeroelastic and other constraints. Most notable among these is the Automated Structural Optimization System (ASTROS) [13]. The procedure uses the finite element method for structural analysis and gradient based techniques for optimization.

In general, an optimization problem can be associated with several objective functions, constraints and design variables. However, in many existing procedures the problem is formulated with a single objective function subject to several constraints [13]. Such procedures do not allow simultaneous minimization or maximization of more than one objective. A commonly used technique for addressing multiobjective problems is to combine individual objective functions in a linear fashion using weight factors [14]. Such methods are judgmental in nature as the answer depends upon weight factors which are often hard to justify. Also, the procedures do not satisfy the Kuhn-Tucker conditions of optimality [14]. To address this issue in a mathematically rigorous way, several formal multiobjective techniques have been developed by Chattopadhyay and McCarthy [15]. In the first method, called the modified global criterion approach, the individual

objective functions are combined into a single composite function using the optimized values for each objective function. The optimized values are obtained through single objective minimization or maximization prior to multiobjective formulation. The drawback of the method is that several single objective optimizations have to be performed to obtain the optimized values. Therefore, this method is not very efficient computationally. Another method, called 'Min $\sum\beta$' (Minimum sum beta) [15], uses pseudo-design variables that represent deviations of the individual objective functions from respective target values. The objective function is then defined as a linear combination of these pseudo-design variables. An appealing feature of this approach is the fact that the objective function is a purely linear function. However, the prescription of the target values is rather arbitrary and hence prone to error.

The multiobjective optimization formulation used in the present work is based on the Kreisselmeier-Steinhauser (K-S) function technique [16]. The K-S function approach can be applied to problems with multiple objectives and inequality constraints [17]. In this approach, each of the original objective functions is transformed into reduced objective functions using the value of the original objective functions calculated at the beginning of the cycle. The reduced objective functions are analogous to constraints. A new constraint vector is defined combining the original constraints and the reduced objective functions. Using the K-S function, a new objective function is now obtained which represents the original objective functions and constraints. Thus the K-S function technique efficiently integrates the objective functions and constraints into a single envelop function. The design variable vector in this formulation remains unchanged. The resulting unconstrained problem can be solved using any of the standard techniques for nonlinear optimization [14]. The search direction vector is obtained using the

Broyden-Fletcher-Goldberg-Shanno (BFGS) algorithm. With the search direction determined, a one-dimensional search for the minimum of the K-S function is performed using the three point quadratic approximation for step length [14]. The gradients for objective functions and constraints are evaluated using the finite difference method.

Since during an optimization process, several computations of the objective functions and constraints are necessary, it is computationally expensive to use exact analysis all the time. Therefore, approximation techniques are commonly used to reduce the analysis effort. Several different approximation techniques have been used in the literature, the most notable being the linear Taylor series and the reciprocal Taylor series approximations [14]. In this research, the two-point approximation technique [18], which has been found to be well suited for nonlinear optimization problems, is used. This technique uses the gradient information from the previous and current design cycles to construct the approximate function value. In the limiting cases the expansion reduces to the first order Taylor series or the reciprocal approximation form.

In composite wings, the ply stacking sequence has a very strong influence on the design objectives and constraints. Often, ply angles are treated as continuous design variables, such as in ASTROS [13], and the resulting solution is replaced by the nearest integral value which can lead to suboptimal design. In practice, ply orientations (and ply thickness) are selected from a range of practical discrete values. Hence ply angles are best treated as discrete design variables. However, parameters such as wing span, chord and other dimensions represent continuous variables. Therefore, the composite wing optimization problem involves both continuous and discrete design variables. Recently, a hybrid optimization technique has been developed by Seeley and Chattopadhyay to simultaneously include continuous and discrete design variables in the optimization

problem [19]. Since the hybrid optimization uses a combinatorial search technique [14] for discrete design variables, the procedure can be expensive computationally. Therefore, this approach has been used for only some of the optimization problems addressed in the present research.

1.1.2 Composite Structural Analysis

The structural analysis of aircraft wings can be performed either through a detailed investigation of the wing sections comprising skins, spars, ribs etc. or through the use of reduced structural models. The detailed analysis based on a full three-dimensional finite element solution [13] is computationally very expensive and requires a large modeling time. Hence, such techniques can be impractical in design optimization or trade-off studies during the conceptual design phase. Therefore, procedures based on reduced structural models, such as 'box beam' and 'equivalent plate', are frequently used during conceptual wing design.

Among the aeroelastic analysis and optimization procedures based on reduced structural model, TSO [20] and ELAPS [21-22] have been widely used. These procedures use an equivalent plate model for structural analysis. The wing box geometry in TSO is limited to trapezoidal planforms, whereas ELAPS can analyze cranked wings through multiple trapezoidal segments. The depth of the structural box, which consists of cover skins and rib, stiffener and spar caps, can be varied over the planform using this procedure. Another procedure, named LS-CLASS [23], uses a structural model similar to ELAPS and includes analytical sensitivity derivatives for efficient aeroservoelastic optimization. However, all of these techniques are based on the Classical Laminate Theory (CLT) [24] which assumes that normals to the midplane before deformation

remain straight and normal to the plane after deformation. Thus CLT assumes deformation due entirely to bending and inplane stretching and neglects transverse shear stresses. Experimental results indicate that CLT underpredicts deflections and overpredicts natural frequencies [24]. Extensive studies comparing the results from CLT based equivalent plate models to detailed finite element models have shown serious limitations of the former approach [25-26]. The largest errors are reported in the torsional behavior. The representation of the transverse shear is identified as the principal reason for the differences. An equivalent plate model based on the First-order Shear Deformation Theory (FSDT) [24] yields a better correlation with finite element solution [25-26]. Thus, the inclusion of transverse shear in equivalent plate models is very important. The FSDT assumes constant transverse shear strain through the laminate thickness. This theory requires shear correction factors which are difficult to obtain because they depend on the lamina properties and the lamination scheme. Therefore, a more accurate description of the transverse shear stresses is necessary.

The Higher-Order Shear Deformation Theory (HSDT) is capable of accurately and efficiently predicting the transverse shear stresses in composites [24]. This theory was used to develop a composite box beam model by McCarthy and Chattopadhyay [27-29]. In this model, each wall of the box beam is analyzed as a composite plate using a refined higher-order displacement field [30]. Continuity between the displacement fields is enforced at the four corners throughout the thickness of each plate. The model accurately captures the transverse shear stresses through the thickness of each wall while satisfying stress free boundary conditions on the inner and outer surfaces. The formulation approximates three-dimensional elasticity solution so that the beam cross-sectional properties are not reduced to one-dimensional parameters. Both inplane and out-of-plane

warping are automatically included in the formulation. The finite element method is used to solve the governing equations of motion. The model has been validated extensively for thin- and thick-walled composite laminates through comparisons with experimental results, other appropriate theories and three-dimensional finite element analysis using brick elements [27-29]. This method is used in the present work for accurate and efficient composite structural analysis of aircraft wings.

1.1.3 Aeroelastic Analysis

Aeroelastic analysis plays a vital role in the design of a high performance aircraft. History of the U.S. Supersonic Transport program shows that the entire aircraft design process was driven by the aeroelastic design cycle [31]. To effectively integrate aeroelastic analysis with the design of composite wings, computationally efficient yet analytically rigorous methods are necessary. The key issues associated with the aeroelastic stability analysis include structural dynamic calculations for natural frequency and mode shapes, unsteady aerodynamic computations to obtain generalized aerodynamic forces and flutter calculation methodology. These issues are briefly discussed next.

The objective of the aeroelastic analysis is to identify the flight condition (velocity and atmospheric density or altitude) at which the aeroelastic system is neutrally stable. At this condition, the system is purely oscillatory and the aerodynamic loads calculated for simple harmonic motion are adequate. The technique for the prediction of three-dimensional unsteady aerodynamic forces for purely oscillatory motion is well developed. In the present research, the generalized aerodynamic forces are computed using the constant-pressure lifting surface method [32] at a given Mach number for specified values of reduced frequency k, assuming simple harmonic motion. This method

is based on linearized aerodynamic potential theory. The lifting surface is divided into small trapezoidal panels, with unknown constant pressure, arranged in strips parallel to the free stream. The downwash boundary condition calculated from and deflection of structural modes is satisfied at mid-span three-quarter chord point of each panel, leading to the determination of the unknown pressures and the aerodynamic forces.

Assuming that the aeroelastic system performs a simple harmonic motion and the use of purely oscillatory air loads, leads to the classical V-g method of flutter prediction [33] which has been extensively used. However, the method is iterative in nature which reduces the efficiency and the results are accurate only at the flutter boundary. To gain an insight into the physical phenomena leading to flutter, it is necessary to obtain valid damping and frequency history. The Laplace domain method of flutter analysis [34] produces root-loci of the system which affords such an insight. The principal difficulty in implementing the Laplace domain method lies in obtaining the air loads for arbitrary motions, since aerodynamic calculations are well developed only for simple harmonic motions. This problem is overcome through the use of rational function approximations (RFA's). The generalized aerodynamic forces contain transcendental terms when expressed as a function in the Laplace domain. To obtain a finite number of terms, the aerodynamic forces are approximated by a rational function of the nondimensionalized Laplace variable p. Several formulations of the RFA's are available in the literature [34-37]. The capabilities of these formulations have been extended and their performances compared in [38]. In the current work, the 'least-squares' approach of [35-36], which has been used by many researchers, has been adopted.

1.1.4 Aerodynamic Analysis

To obtain aerodynamic efficiency (lift-to-drag ratio), it is necessary to compute lift and drag for the wing. Wing drag at high subsonic or transonic Mach numbers comprises induced drag, skin-friction drag and compressibility (wave) drag. The panel method based on the constant-pressure lifting surface [32] is also capable of predicting steady normal forces. The components of the normal force along the freestream and the direction perpendicular to it yield induced drag and lift, respectively. The skin-friction drag arises from the viscous effects in the mostly turbulent boundary layer adjacent to the wing surface. The turbulent boundary layer problem is a very difficult one to solve theoretically. Instead, empirical formulae developed by von Kármán or Schlichting [39] are often employed to compute turbulent skin-friction drag. In the current study, the skin-friction drag is calculated using the Schlichting empirical formula, corrected to include the Mach number effect [40].

The compressibility drag refers to the pressure drag resulting from increase in Mach number above low subsonic value. At high subsonic or transonic Mach numbers, shocks develop on the top of the wing due to increased airflow velocity, which leads to 'drag rise'. The drag rise can be analytically predicted only through the use of sophisticated nonlinear computational aerodynamic analysis, since the linear analysis in this Mach number regime produces completely incorrect results [40]. Therefore, an empirical method described in [41] has been used in the current work to obtain the compressibility drag. This method, called the 'crest-critical Mach number method', has been used in other optimization studies [9, 42]. In this approach, the free stream Mach number which gives sonic flow at the highest point on the airfoil (tangent to the free stream) is first determined. This Mach number, called the crest-critical Mach number, is a function of airfoil thickness-to-chord ratio, lift coefficient and wing sweep. The compressibility drag

is then obtained using empirical relationship between the ratio of freestream Mach number to the crest-critical Mach number and drag rise.

1.1.5 Smart Composite Wing Design

Smart materials respond to an external stimulus, such as electric field, by changing their shape. When attached to a host structure, they cause deformation of the structure. The feasibility of using smart structures is increasing because of the availability of smart materials commercially, ease of integration with laminated structures, potential of large performance enhancement and advances in related fields [43]. Piezoelectric materials are popular for aeroelastic/aerodynamic and vibration control [44]. When a piezoelectric material is stressed mechanically by a force, it generates an electric charge. Conversely, when an electric field is applied, the material elongates or shortens depending on the polarity of the applied electric field. A piezoelectric element is therefore capable of being used both as actuators and sensors. Currently, most piezoelectric devices utilize lead zirconate titanate (PZT), which is a piezoceramic material. The desirable properties of PZT include a high level of piezoelectric activity, a wide frequency range and first-order linearity between applied voltage and induced strain [43].

Composite wings with either embedded or surface bonded PZT actuators / sensors have been investigated by researchers. Heeg [45] demonstrated analytically and experimentally that piezoelectric materials can increase the flutter speed of a simple two degree of freedom wing model. Song *et al.* [46] showed that incorporation of piezoelectric layers in a wing can improve both divergence instability and aeroelastic lift distribution. Paige *et al.* [47] used piezoelectric actuation to control panel flutter. The structural modeling issues associated with piezoelectric actuation of composite plates

have also been considered. The displacement field based on the classical laminate theory is used by Chopra [43] and Crawley and Lazarus [48]. Chattopadhyay and Seeley [49] and Seeley [50] have used the higher-order theory (HSDT) for modeling composite plates with piezoelectric actuators/ sensors. The present research uses the above higher-order plate theory to model composite box beams with surface bonded piezoelectric actuators. The formulation of the box beam (with taper and sweep) is similar to that of McCarthy [27] and McCarthy and Chattopadhyay [28, 29]. The governing equations of motion are solved using the finite element method to be able to address realistic wing geometries.

The placement and the number of actuators necessary for improved aeroelastic control require the use of formal optimization techniques. Several investigations have been reported which address the issue of actuator placement using both deterministic [51-52] and heuristic [53-55] approaches. For aeroelastic control, actuators placed at wing root have been shown to be most effective [52, 55]. Power consumption is also an important issue related to the piezoelectric actuation of structures, especially for active control with multiple actuators/sensors [56].

In the present research, a new procedure for the multidisciplinary design optimization of smart composite wings has been developed, incorporating optimization and analysis methods discussed above. The principal load carrying member of the wing is modeled as a composite box beam with surface bonded piezoelectric actuators. The optimization problem is formulated with the coupling of structural, aerodynamic, aeroelastic and control (passive) design criteria. The higher-order theory has been used for the wing structural analysis and its impact on aeroelastic results have been demonstrated through comparisons with those obtained using CLT. The effect of composite ply orientations on

flutter and divergence speeds has been studied The developed MDO procedures are demonstrated through applications to wing design.

1.2 Multidisciplinary Design Optimization of Turbomachinery Blades

High performance aircraft engine components operate under severe aerodynamic, thermal and structural environments. The design of the blade profile is one of the major aspects in engine design [57]. Engine performance is strongly affected by the aerodynamic efficiency of the blades, which can be enhanced through efficient design of the blade external shape. Sharp fluctuations in the blade (suction and pressure) surface Mach number can lead to flow separation resulting in loss of aerodynamic efficiency. Airflow velocity also impacts blade cooling and temperature distributions. The maximum and average temperatures of the blade are desired to be minimum, as the structural integrity and engine life are affected by these temperatures. From the structural point of view, it is important to maintain blade stresses and vibration levels within the allowable limits. Therefore, efficient blade design is a multidisciplinary problem that requires the integration of several disciplines such as aerodynamics, heat transfer and structures.

The direct design method, in which the designer changes the blade geometry iteratively until desired performance is achieved, affords direct control of the blade design parameters. However, this method is very laborious and requires considerable insight [58]. In the inverse design method [59], the performance is specified in terms of velocity or pressure distributions to obtain the desired blade shape. This requires a knowledge of the desired velocity or pressure distribution. Also, the imposition of constraints is not easily applicable in inverse design.

Design optimization techniques have been used by many researchers to optimize airfoil shape for aircraft wings [60-61]. However, the application of optimization procedures to turbomachinery blade design has been rather limited. Chattopadhyay *et al.* [62] developed an optimization procedure for efficient design of turbine blades which successfully eliminated the leading edge velocity spikes while maintaining the tangential force coefficient. Aerodynamic analysis was performed using a two-dimensional panel code. The pressure and suction surfaces were approximated by polynomials, whereas circular and elliptic arcs were used to describe the leading edges. The procedure was further extended by Narayan *et al.* [63] to include heat transfer criteria where coolant hole shapes and sizes were included as additional design variables. This multidisciplinary optimization procedure resulted in significant reduction in blade temperatures and smooth velocity distributions. For aerodynamic optimization, Goel *et al.* [64] used a combination of numerical optimization, hill climbing and genetic algorithm in an attempt to overcome the problem of local minima, since the turbine design problem is mutimodal. Turbine blade geometry was represented by Bezier-Bernstein polynomial [65]. Blade performance was measured by the distribution of the surface Mach number obtained through inviscid flow calculations.

The current work presents the development and application of a new multidisciplinary optimization procedure incorporating more comprehensive analysis methods for the design of turbine blades. The procedure integrates aerodynamic and heat transfer design considerations, with mechanical constraints on blade geometry. Bezier-Bernstein polynomial is used to accurately represent airfoil shape with a relatively small number of design variables. The aerodynamic analysis is based on the thin shear layer approximation of the Navier-Stokes equations [66-67]. Grid generation is accomplished

by solving Poisson equations with arbitrarily specified inner and outer boundary points [68-69]. A finite element formulation is used to calculate blade interior temperatures. Total pressure and exit kinetic energy losses are minimized through a constrained multiobjective optimization formulation using the Kreisselmeier-Steinhauser (K-S) function approach discussed earlier. The maximum and average blade temperatures and certain geometric parameters of the blade are treated as constraints.

2. Objectives

The primary objective of the present research is to develop a multidisciplinary optimization procedure for the conceptual design of composite aircraft wings with surface bonded piezoelectric actuators. The optimization problem addressed involves the coupling of structural mechanics (including smart material), aeroelasticity and aerodynamics. The validity of the designs obtained using MDO procedures depends strongly upon the accuracy of the analytical methods used. Therefore, it is essential to integrate accurate and efficient analysis techniques to obtain meaningful optimum designs within a reasonable time. Since this multidisciplinary problem has multiple nonlinear objective functions and constraints, sophisticated optimization algorithm is required for solution.

In the present research, the load carrying member of the wing is idealized and represented as a composite box beam. Each wall of the box beam is analyzed as a plate using a refined higher-order displacement field. This structural modeling accurately captures the transverse shear stresses through the thickness of each wall while satisfying stress free boundary conditions on the inner and outer surfaces of the beam. The present research extends the composite box beam model to include piezoelectric actuators bonded to top and bottom surfaces. Detailed structural modeling issues associated with piezoelectric actuation of composite structures are considered. The governing equations of motion are solved using the finite element method to analyze practical wing geometries.

For the aeroelastic stability analysis, both the classical V-g method and the Laplace domain method are utilized. The V-g method gives accurate results at the flutter boundary, but requires iterative solution. The Laplace domain method involves

approximating generalized aerodynamic forces, but it produces root-loci of the system which give an insight into the physical phenomena leading to flutter/divergence. This method can be efficiently integrated within an optimization procedure. The steady and unsteady aerodynamic forces are obtained using linearized aerodynamic potential theory for compressible flows.

The Kreisselmeier-Steinhauser (K-S) function technique is used to efficiently integrate the objective functions and constraints into a single envelop function for multiobjective optimization with continuous design variables. The resulting unconstrained problem is solved using the Broyden-Fletcher-Goldberg-Shanno algorithm for nonlinear optimization. The hybrid optimization method, though computationally expensive, includes continuous and discrete design variables simultaneously.

The secondary objective of this work is to develop a multidisciplinary optimization procedure for the design of turbomachinery blades. Aerodynamic and heat transfer design objectives are integrated along with various mechanical constraints on the blade geometry. The blade geometry is represented by Bezier-Bernstein polynomials, which results in a relatively small number of design variables for the optimization. Thin shear layer approximation of the Navier-Stokes equation is used for the viscous blade-to-blade flow calculations. Grid generation is accomplished by solving Poisson equations. The maximum and average blade temperatures are obtained through a finite element analysis. Total pressure and exit kinetic energy losses are minimized, with constraints on blade temperatures and geometry.

The specific goals of the current research are as follows:

1. Establish the significance of the refined higher-order displacement field on the aeroelastic stability of composite wings. Study the effect of composite ply orientations on flutter and divergence speeds.

2. Extend the higher-order theory based composite box beam model to include piezoelectric actuators bonded to top and bottom surfaces, considering detailed structural modeling issues associated with piezoelectric actuation of composite structures.

3. Develop a multidisciplinary optimization procedure for the conceptual design of composite aircraft wings incorporating accurate and efficient analysis methods and multiobjective optimization technique. The optimization problem is formulated with the objective of simultaneously minimizing wing weight and maximizing its aerodynamic efficiency. Design variables include composite ply orientations, ply thicknesses, wing sweep and piezoelectric actuator thickness. Constraints are placed on the flutter/divergence dynamic pressure, wing root stresses and the maximum electric field applied to the actuators.

4. Develop of an accurate and computationally efficient optimization procedure for integrated aerodynamic and heat transfer design of turbomachinery blades.

3. MDO Methodology for Smart Composite Wings

The multidisciplinary design optimization of smart composite wings involves the coupling of structural mechanics (including smart material), aeroelasticity and aerodynamics. For the developed MDO procedure to be applicable to practical problems, the analysis and the optimization techniques must be computationally efficient and sufficiently rigorous. These methods are described in the following sections.

3.1 Analysis

3.1.1 Structural Modeling

The load carrying member of the wing is represented as a single-celled rectangular box beam with taper and sweep (Figures 1 and 2). Piezoelectric actuators are bonded to top and bottom surfaces of the box beam.

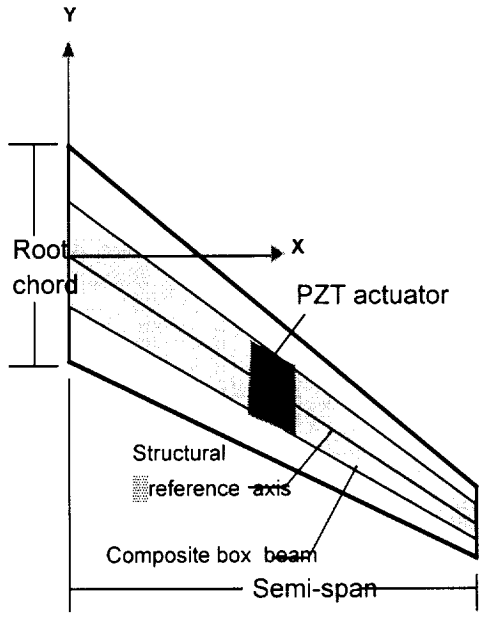

Figure 1. Wing planform

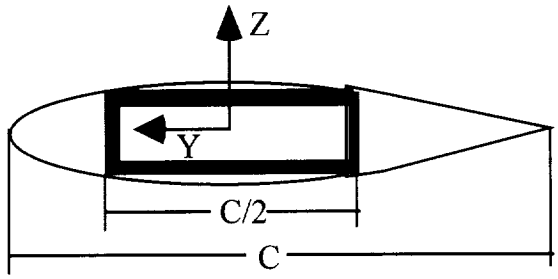

Figure 2. Wing cross section

The box beam is modeled using composite laminates to represent the four walls (Figure 3). The global coordinate system for the box beam is denoted (X, Y, Z) and the local coordinate system for the i-th wall is denoted (x_i, y_i, z_i). The subscript 'i' is omitted for convenience in the rest of the dissertation. For each of the individual walls of the box beam, the inplane displacements are represented as cubic functions of the thickness coordinate and the transverse displacement is assumed constant through the laminate thickness. The higher-order displacement field [30] described in the local coordinate system (Figure 3) is as follows.

$$u(x,y,z) = u_0(x,y) + z\psi_x(x,y) + z^2\xi_x(x,y) + z^3\zeta_x(x,y)$$

$$v(x,y,z) = v_0(x,y) + z\psi_y(x,y) + z^2\xi_y(x,y) + z^3\zeta_y(x,y)$$

$$w(x,y) = w_0(x,y) \tag{1}$$

where u_0, v_0 and w_0 denote the displacements of a point (x, y) on the midplane and ψ_x and ψ_y represent the rotations of normals to the midplane about the y and x axes, respectively. The higher-order terms ξ_x , ζ_x, ξ_y and ζ_y represent beam warping in each plane.

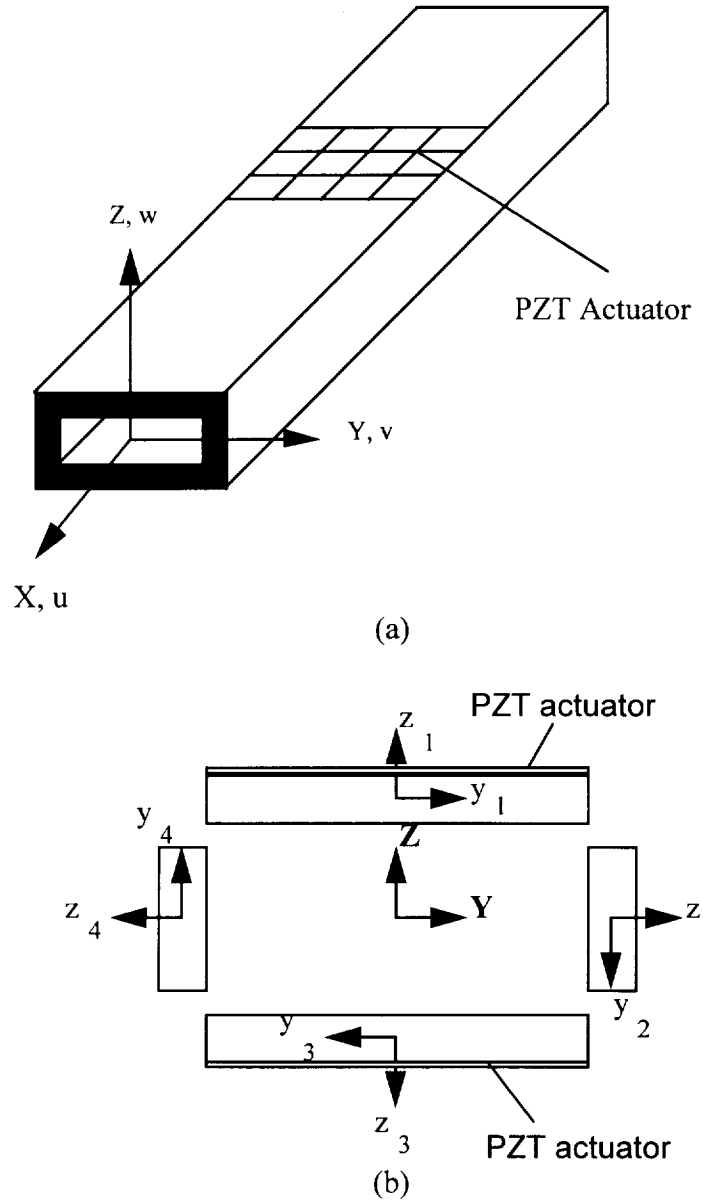

Figure 3. Smart box beam construction

The displacement field must satisfy the conditions that the transverse shear stresses, σ_{xz} and σ_{yz}, vanish on the plate top and bottom surfaces.

$$\sigma_{xz}(x,y,\pm\frac{h}{2}) = 0$$

$$\sigma_{yz}(x,y,\pm\frac{h}{2}) = 0 \tag{2}$$

where h is the plate thickness. For orthotropic composite plates, these conditions imply that the corresponding strains be zero on the surfaces. This yields the following relations.

$$\xi_x = 0$$

$$\xi_y = 0$$

$$\zeta_x = -\frac{4}{3h^2}(\frac{\partial w_0}{\partial x} + \psi_x)$$

$$\zeta_y = -\frac{4}{3h^2}(\frac{\partial w_0}{\partial y} + \psi_y) \tag{3}$$

The refined higher-order displacement field is now written as follows.

$$\begin{aligned} u &= u_0 + z\psi_x - \frac{4z^3}{3h^2}(\frac{\partial w_0}{\partial x} + \psi_x) \\ v &= v_0 + z\psi_y - \frac{4z^3}{3h^2}(\frac{\partial w_0}{\partial y} + \psi_y) \\ w &= w_0 \end{aligned} \tag{4}$$

The functions u_0, v_0, w_0, ψ_x and ψ_y represent unknown functions of x and y. It is important to note that the displacement field for the refined higher-order theory (Equation (4)) has the same number of dependent variables as those used in the first-order shear deformation theory (FSDT), although inplane displacements are cubic functions of the thickness coordinate. By making substitutions,

$$\psi_x = \phi_x - \frac{\partial w_0}{\partial x}$$

$$\psi_y = \phi_y - \frac{\partial w_0}{\partial y} \tag{5}$$

the following modified form of the displacement field is obtained.

$$u = u_0 - z\frac{\partial w_0}{\partial x} + z\left[1 - \frac{4}{3}\left(\frac{z}{h}\right)^2\right]\phi_x$$

$$v = v_0 - z\frac{\partial w_0}{\partial y} + z\left[1 - \frac{4}{3}\left(\frac{z}{h}\right)^2\right]\phi_y \qquad (6)$$

$$w = w_0$$

where ϕ_x and ϕ_y represent the additional rotations due to shear deformation about the y and x axes, respectively. It should be noted that the displacement field for the classical laminate theory can be obtained by setting ϕ_x and ϕ_y , equal to zero in equation (6).

Since there are only six unique values of the stresses and the strains due to symmetry, the following notation is used to define these quantities.

$$\begin{Bmatrix} \sigma_1 \\ \sigma_2 \\ \sigma_3 \\ \sigma_4 \\ \sigma_5 \\ \sigma_6 \end{Bmatrix} = \begin{Bmatrix} \sigma_{xx} \\ \sigma_{yy} \\ \sigma_{zz} \\ \sigma_{yz} \\ \sigma_{xz} \\ \sigma_{xy} \end{Bmatrix} \qquad (7)$$

$$\begin{Bmatrix} \varepsilon_1 \\ \varepsilon_2 \\ \varepsilon_3 \\ \varepsilon_4 \\ \varepsilon_5 \\ \varepsilon_6 \end{Bmatrix} = \begin{Bmatrix} \varepsilon_{xx} \\ \varepsilon_{yy} \\ \varepsilon_{zz} \\ 2\varepsilon_{yz} \\ 2\varepsilon_{xz} \\ 2\varepsilon_{xy} \end{Bmatrix} \qquad (8)$$

where x, y and z correspond to 1, 2 and 3 directions, respectively. Assuming small displacements and rotations, a linear strain-displacement relationship is used.

$$\varepsilon_1 = \frac{\partial u}{\partial x}, \quad \varepsilon_2 = \frac{\partial v}{\partial y}, \quad \varepsilon_3 = \frac{\partial w}{\partial z} = 0$$
$$\varepsilon_4 = \frac{\partial v}{\partial z} + \frac{\partial w}{\partial y}, \quad \varepsilon_5 = \frac{\partial u}{\partial z} + \frac{\partial w}{\partial x}, \quad \varepsilon_6 = \frac{\partial u}{\partial y} + \frac{\partial v}{\partial x} \tag{9}$$

In the above equation, ε_1 and ε_2 are inplane normal strains, ε_3 is transverse normal strain, ε_4 and ε_5 are transverse shear strains and ε_6 is inplane shear strain. Using the above strain-displacement relationships (Equation (9)) and the refined higher-order displacement field (Equation (4)), the strains can be expressed in terms of midplane displacements and curvatures as follows.

$$\begin{aligned}
\varepsilon_1 &= \varepsilon_1^0 + z\kappa_1^0 + z^3\kappa_1^2 \\
\varepsilon_2 &= \varepsilon_2^0 + z\kappa_2^0 + z^3\kappa_2^2 \\
\varepsilon_6 &= \varepsilon_6^0 + z\kappa_6^0 + z^3\kappa_6^2 \\
\varepsilon_4 &= \varepsilon_4^0 + z^2\kappa_4^2 \\
\varepsilon_5 &= \varepsilon_5^0 + z^2\kappa_5^2
\end{aligned} \tag{10}$$

where

$$\varepsilon_1^0 = \frac{\partial u_0}{\partial x}, \quad \kappa_1^0 = \frac{\partial \psi_x}{\partial x}, \quad \kappa_1^2 = -\frac{4}{3h^2}\left(\frac{\partial \psi_x}{\partial x} + \frac{\partial^2 w_0}{\partial x^2}\right)$$
$$\varepsilon_2^0 = \frac{\partial v_0}{\partial y}, \quad \kappa_2^0 = \frac{\partial \psi_y}{\partial y}, \quad \kappa_2^2 = -\frac{4}{3h^2}\left(\frac{\partial \psi_y}{\partial y} + \frac{\partial^2 w_0}{\partial y^2}\right)$$
$$\varepsilon_6^0 = \frac{\partial u_0}{\partial y} + \frac{\partial v_0}{\partial x}, \quad \kappa_6^0 = \frac{\partial \psi_x}{\partial y} + \frac{\partial \psi_y}{\partial x}, \quad \kappa_6^2 = -\frac{4}{3h^2}\left(\frac{\partial \psi_x}{\partial y} + \frac{\partial \psi_y}{\partial x} + 2\frac{\partial^2 w_0}{\partial x \partial y}\right)$$
$$\varepsilon_4^0 = \frac{\partial w_0}{\partial y} + \psi_y, \quad \kappa_4^2 = -\frac{4}{h^2}\left(\frac{\partial w_0}{\partial y} + \psi_y\right)$$
$$\varepsilon_5^0 = \frac{\partial w_0}{\partial x} + \psi_x, \quad \kappa_5^2 = -\frac{4}{h^2}\left(\frac{\partial w_0}{\partial x} + \psi_x\right) \tag{11}$$

The generalized Hooke's law is used to relate the stresses and the strains. For laminates made of orthotropic materials (with elastic symmetry parallel to the 1-2 plane) the constitutive relation [70] is written as

$$\begin{Bmatrix}\sigma_1\\ \sigma_2\\ \sigma_6\end{Bmatrix}=\begin{bmatrix}Q_{11} & Q_{12} & 0\\ Q_{12} & Q_{22} & 0\\ 0 & 0 & Q_{66}\end{bmatrix}\begin{Bmatrix}\varepsilon_1\\ \varepsilon_2\\ \varepsilon_6\end{Bmatrix}$$

$$\begin{Bmatrix}\sigma_4\\ \sigma_5\end{Bmatrix}=\begin{bmatrix}Q_{44} & 0\\ 0 & Q_{55}\end{bmatrix}\begin{Bmatrix}\varepsilon_4\\ \varepsilon_5\end{Bmatrix} \tag{12}$$

where Q_{ij}, the plane-stress reduced elastic constants in the material axes of the laminate, are related to the material engineering constants by the following equations.

$$Q_{11}=\frac{E_1}{1-\nu_{12}\nu_{21}},\quad Q_{12}=\frac{\nu_{12}E_2}{1-\nu_{12}\nu_{21}},\quad Q_{22}=\frac{E_2}{1-\nu_{12}\nu_{21}}$$
$$Q_{44}=G_{23},\quad Q_{55}=G_{13},\quad Q_{66}=G_{12} \tag{13}$$

In the above equations, there are only five independent elastic constants. For laminates consisting of multiple plies at different orientations, it is convenient to use the transformed elastic coefficients [70] in the laminate coordinate system (x, y, z). After transformation to the laminate coordinate system, the constitutive relations can be written as

$$\begin{Bmatrix}\bar{\sigma}_1\\ \bar{\sigma}_2\\ \bar{\sigma}_6\end{Bmatrix}=\begin{bmatrix}\bar{Q}_{11} & \bar{Q}_{12} & \bar{Q}_{16}\\ \bar{Q}_{12} & \bar{Q}_{22} & \bar{Q}_{26}\\ \bar{Q}_{16} & \bar{Q}_{26} & \bar{Q}_{66}\end{bmatrix}\begin{Bmatrix}\bar{\varepsilon}_1\\ \bar{\varepsilon}_2\\ \bar{\varepsilon}_6\end{Bmatrix}$$

$$\begin{Bmatrix}\bar{\sigma}_4\\ \bar{\sigma}_5\end{Bmatrix}=\begin{bmatrix}\bar{Q}_{44} & \bar{Q}_{45}\\ \bar{Q}_{45} & \bar{Q}_{55}\end{bmatrix}\begin{Bmatrix}\bar{\varepsilon}_4\\ \bar{\varepsilon}_5\end{Bmatrix} \tag{14}$$

where $\bar{Q}_{ij}$ are the transformed elastic constants.

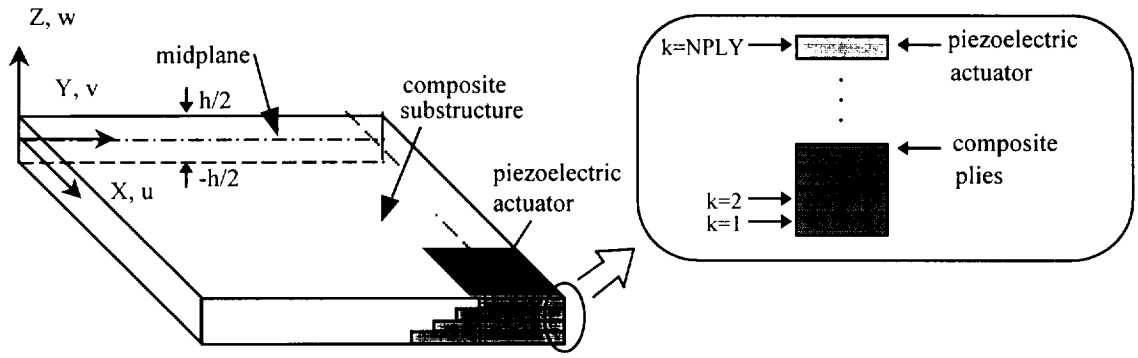

Figure 4. Composite laminate with surface bonded piezoelectric actuator

The constitutive relation for any ply of piezoelectric material is written as follows [48].

$$\bar{\sigma}_i = \bar{Q}_{ij}\left(\bar{\varepsilon}_j - \Lambda_j\right) \qquad (i, j = 1, 2, 6) \tag{15}$$

where Λ_j is the induced strain due to piezoelectric actuation. Equation (15) is applicable if the piezoelectric material thickness is small compared to the plate thickness (Figure 4). The actuation strain vector Λ_j contains inplane normal and shear strain components, and can be treated similar to thermal strain in the elasticity formulation. The induced strain is used to control extension, bending or twisting of a laminate. Generally, an electric field is applied through the thickness of the PZT used as an actuator. Also, the PZT materials are isotropic and, therefore, its orientation has no effect on the material properties. Denoting the thickness direction as '3', the induced strain for PZT material is obtained from the following relation.

$$\begin{Bmatrix} \Lambda_1 \\ \Lambda_2 \\ \Lambda_6 \end{Bmatrix} = \begin{Bmatrix} d_{31} \\ d_{31} \\ 0 \end{Bmatrix} E_3 \tag{16}$$

In equation (16), E_3 is the applied electric field and d_{31} is the mechanical-electrical coupling coefficient of the material. The applied electric field is obtained by dividing the applied voltage by the thickness of the PZT layer. The maximum applied electric field must be smaller than the coercive field to avoid depoling the material.

In the 'equivalent single layer' approach of composite analysis [70], the laminate stress resultants are obtained by integrating the stresses through the thickness as follows. The stresses also include effects due to piezoelectric actuation.

$$(N_i,\ M_i,\ P_i) = \int_{-h/2}^{h/2} \bar{\sigma}_i \left(1,\ z,\ z^3\right) dz \qquad (i = 1, 2, 6)$$

$$(Q_2,\ R_2) = \int_{-h/2}^{h/2} \bar{\sigma}_4 \left(1,\ z^2\right) dz$$

$$(Q_1,\ R_1) = \int_{-h/2}^{h/2} \bar{\sigma}_5 \left(1,\ z^2\right) dz \qquad (17)$$

The first three terms (N_i, M_i and P_i) are the inplane terms, which can be decomposed as follows.

$$\begin{aligned} N_i &= N_i^A - N_i^P \\ M_i &= M_i^A - M_i^P \quad (i = 1, 2, 6) \\ P_i &= P_i^A - P_i^P \end{aligned} \qquad (18)$$

The first terms on the right hand side equation (18) (superscript 'A') represent the stress resultants due to actual strain field, whereas the second terms (superscript 'P') represent the resultants from piezoelectric actuation.

The stress resultants due to the actual strain field can be written in terms of the elastic constants, $\bar{Q}_{ij}$, and strains, $\bar{\varepsilon}_j$, as follows.

$$\left(N_i^A,\ M_i^A,\ P_i^A\right)=\int_{-h/2}^{h/2}\overline{Q}_{ij}\bar{\varepsilon}_j\left(1,\ z,\ z^3\right)dz \qquad (i=1,2,6) \tag{19}$$

Substituting the expression for strains from equation (10), the plate constitutive relations are expressed as follows.

$$\begin{Bmatrix}\begin{Bmatrix}N_1^A\\N_2^A\\N_6^A\end{Bmatrix}\\\begin{Bmatrix}M_1^A\\M_2^A\\M_6^A\end{Bmatrix}\\\begin{Bmatrix}P_1^A\\P_2^A\\P_6^A\end{Bmatrix}\end{Bmatrix}=\begin{bmatrix}\begin{bmatrix}A_{11}&A_{12}&A_{16}\\&A_{22}&A_{26}\\\text{sym}&&A_{66}\end{bmatrix}&\begin{bmatrix}B_{11}&B_{12}&B_{16}\\&B_{22}&B_{26}\\\text{sym}&&B_{66}\end{bmatrix}&\begin{bmatrix}E_{11}&E_{12}&E_{16}\\&E_{22}&E_{26}\\\text{sym}&&E_{66}\end{bmatrix}\\&\begin{bmatrix}D_{11}&D_{12}&D_{16}\\&D_{22}&D_{26}\\\text{sym}&&D_{66}\end{bmatrix}&\begin{bmatrix}F_{11}&F_{12}&F_{16}\\&F_{22}&F_{26}\\\text{sym}&&F_{66}\end{bmatrix}\\\text{symmetric}&&\begin{bmatrix}H_{11}&H_{12}&H_{16}\\&H_{22}&H_{26}\\\text{sym}&&H_{66}\end{bmatrix}\end{bmatrix}\begin{Bmatrix}\begin{Bmatrix}\varepsilon_1^0\\\varepsilon_2^0\\\varepsilon_6^0\end{Bmatrix}\\\begin{Bmatrix}\kappa_1^0\\\kappa_2^0\\\kappa_6^0\end{Bmatrix}\\\begin{Bmatrix}\kappa_1^2\\\kappa_2^2\\\kappa_6^2\end{Bmatrix}\end{Bmatrix} \tag{20}$$

$$\begin{Bmatrix}Q_2\\Q_1\\R_2\\R_1\end{Bmatrix}=\begin{bmatrix}A_{44}&A_{45}&D_{44}&D_{45}\\&A_{55}&D_{45}&D_{55}\\&&F_{44}&F_{45}\\\text{symmmetric}&&&F_{55}\end{bmatrix}\begin{Bmatrix}\varepsilon_4^0\\\varepsilon_5^0\\\kappa_4^2\\\kappa_5^2\end{Bmatrix} \tag{21}$$

where the plate stiffnesses are defined as follows.

$$\left(A_{ij},\ B_{ij}.\ D_{ij},\ E_{ij},\ F_{ij},\ H_{ij}\right)=\int_{-h/2}^{h/2}\overline{Q}_{ij}\left(1,\ z,\ z^2,\ z^3,\ z^4,\ z^6\right)dz \quad (i,j=1,2,6) \tag{22}$$

$$\left(A_{ij},\ D_{ij},\ F_{ij}\right)=\int_{-h/2}^{h/2}\overline{Q}_{ij}\left(1,\ z^2,\ z^4\right)dz \quad (i,j=4,5) \tag{23}$$

The stress resultants due to piezoelectric actuation can be similarly defined as follows.

$$\left(N_i^P,\ M_i^P,\ P_i^P\right)=\int_{-h/2}^{h/2}\overline{Q}_{ij}\Lambda_j\left(1,\ z,\ z^3\right)dz \qquad (i = 1, 2, 6) \tag{24}$$

where the stiffness matrix, $\overline{Q}_{ij}$, includes the elastic constants of the piezoelectric material only. Using the stiffness matrices for the PZT material, the stress resultants can be expressed as

$$N^P=\begin{Bmatrix}\begin{Bmatrix}N_1^P\\N_2^P\\N_6^P\end{Bmatrix}\\\begin{Bmatrix}M_1^P\\M_2^P\\M_6^P\end{Bmatrix}\\\begin{Bmatrix}P_1^P\\P_2^P\\P_6^P\end{Bmatrix}\end{Bmatrix}=\begin{bmatrix}\begin{bmatrix}A_{11}&A_{12}&A_{16}\\&A_{22}&A_{26}\\\text{sym}&&A_{66}\end{bmatrix}&\begin{bmatrix}B_{11}&B_{12}&B_{16}\\&B_{22}&B_{26}\\\text{sym}&&B_{66}\end{bmatrix}&\begin{bmatrix}E_{11}&E_{12}&E_{16}\\&E_{22}&E_{26}\\\text{sym}&&E_{66}\end{bmatrix}\\\begin{bmatrix}0\end{bmatrix}&\begin{bmatrix}0\end{bmatrix}&\\\text{symmetric}&\begin{bmatrix}0\end{bmatrix}&\end{bmatrix}\begin{Bmatrix}\begin{Bmatrix}\Lambda_1\\\Lambda_2\\\Lambda_6\end{Bmatrix}\\\begin{Bmatrix}0\\0\\0\end{Bmatrix}\\\begin{Bmatrix}0\\0\\0\end{Bmatrix}\end{Bmatrix} \tag{25}$$

where the PZT stiffness matrices are given by the following equation.

$$\left(A_{ij},\ B_{ij}.\ E_{ij}\right)=\int_{-h/2}^{h/2}\overline{Q}_{ij}\left(1,\ z,\ z^3\right)dz \quad (i,j = 1,2,6) \tag{26}$$

The box beam equations of motion are derived using the Hamilton's principle [24] which assumes the following form, in the absence of any nonconservative forces.

$$\delta\int_{t_1}^{t_2}\left[K-(V+U)\right]dt = 0 \tag{27}$$

where δ represents the variation and K is the kinetic energy, V is the potential energy due to external forces, U is the strain energy and t_1 and t_2 are initial and final times,

respectively. Using variational principles, equation (27) may be written in terms of the individual wall (plate) quantities as follows.

$$\int_{t_1}^{t_2}\left[\sum_{i=1}^{N}\delta K_i - \delta V_i - \delta U_i\right]dt = 0 \tag{28}$$

where N is the total number of walls (N=4 for a box beam). The variations of the elastic strain energy, the potential energy and the kinetic energy, in each plate, are written as follows.

$$\delta U = \int_{-h/2}^{h/2}\int_{A}\left(\sigma_1\delta\varepsilon_1 + \sigma_2\delta\varepsilon_2 + \sigma_4\delta\varepsilon_4 + \sigma_5\delta\varepsilon_5 + \sigma_6\delta\varepsilon_6\right)dA\,dz$$

$$\delta V = \int_{A} p(x,y)\delta w\,dA$$

$$\delta K = \frac{\delta}{2}\int_{-h/2}^{h/2}\int_{A}\rho\left(\dot{u}^2 + \dot{v}^2 + \dot{w}^2\right)dA\,dz \tag{29}$$

where $(\dot{\cdot})$ denotes differentiation with respect to time, A is the plate area, ρ is the material density and p(x,y) is the distributed load. Substitution of equation (29) into equation (28), integration and collection of the coefficients of various terms, yields the following equations of motion.

$$\delta u: \quad \frac{\partial N_1}{\partial x} + \frac{\partial N_6}{\partial y} = I_1\ddot{u} + \bar{I}_2\ddot{\psi}_x - \frac{4}{3h^2}I_4\frac{\partial \ddot{w}}{\partial x}$$

$$\delta v: \quad \frac{\partial N_6}{\partial x} + \frac{\partial N_2}{\partial y} = I_1\ddot{v} + \bar{I}_2\ddot{\psi}_y - \frac{4}{3h^2}I_4\frac{\partial \ddot{w}}{\partial y}$$

$$\delta w: \quad \frac{\partial Q_1}{\partial x} + \frac{\partial Q_2}{\partial y} + p - \frac{4}{h^2}\left(\frac{\partial R_1}{\partial x} + \frac{\partial R_2}{\partial y}\right) + \frac{4}{3h^2}\left(\frac{\partial^2 P_1}{\partial x^2} + 2\frac{\partial^2 P_6}{\partial y\partial x} + \frac{\partial^2 P_2}{\partial y^2}\right)$$

$$= I_1\ddot{w} - \frac{4}{3h^2}I_7\left(\frac{\partial^2 \ddot{w}}{\partial x^2} + \frac{\partial^2 \ddot{w}}{\partial y^2}\right) + \frac{4}{3h^2}I_4\left(\frac{\partial \ddot{u}}{\partial x} + \frac{\partial \ddot{v}}{\partial y}\right) + \frac{4}{3h^2}\bar{I}_5\left(\frac{\partial \ddot{\psi}_x}{\partial x} + \frac{\partial \ddot{\psi}_y}{\partial y}\right)$$

$$\delta\psi_x : \quad \frac{\partial M_1}{\partial x}+\frac{\partial M_6}{\partial y}-Q_1+\frac{4}{h^2}R_1-\frac{4}{3h^2}\left(\frac{\partial P_1}{\partial x}+\frac{\partial P_6}{\partial y}\right)=\bar{I}_2\ddot{u}+\bar{I}_3\ddot{\psi}_x-\frac{4}{3h^2}\bar{I}_5\frac{\partial \ddot{w}}{\partial x}$$

$$\delta\psi_y : \quad \frac{\partial M_6}{\partial x}+\frac{\partial M_2}{\partial y}-Q_2+\frac{4}{h^2}R_2-\frac{4}{3h^2}\left(\frac{\partial P_6}{\partial x}+\frac{\partial P_2}{\partial y}\right)=\bar{I}_2\ddot{v}+\bar{I}_3\ddot{\psi}_y-\frac{4}{3h^2}\bar{I}_5\frac{\partial \ddot{w}}{\partial y} \tag{30}$$

where the stress resultants N_i, M_i, P_i, Q_i and R_i are as defined in equation (18) and the inertia terms are defined as

$$(I_1, I_2, I_3, I_4, I_5, I_7)=\int_{-h/2}^{h/2}\rho(1, z, z^2, z^3, z^4, z^6)dz$$

$$\bar{I}_2 = I_2-\frac{4}{3h^2}I_4$$

$$\bar{I}_5 = I_5-\frac{4}{3h^2}I_7$$

$$\bar{I}_3 = I_3-\frac{8}{3h^2}I_5+\frac{16}{9h^4}I_7 \tag{31}$$

For the solution of the equations of motion, appropriate natural or essential boundary conditions [70] needs to be specified.

The finite element method is well suited to solve the above equations of motion, accounting for discontinuities in the material properties and complex geometry. The discretized equations of motion are obtained using a two-dimensional finite element formulation in the local coordinate system of each individual wall. To maintain continuity of displacements and to ensure that the walls remain normal to each other after deformation, appropriate constraints are imposed on displacements and rotations of individual walls at the four corners of the box beam cross section (Figure 3). A four noded plate element is used with 11 degrees of freedom per node. This element is C^1 continuous in the zeroth order displacements (u_0, v_0 and w_0) and C^0 continuous in the

higher-order terms (ψ_x and ψ_y). The nodal degree of freedom vector is defined as follows.

$$q = \left[u_0, \frac{\partial u_0}{\partial x}, \frac{\partial u_0}{\partial y}, v_0, \frac{\partial v_0}{\partial x}, \frac{\partial v_0}{\partial y}, w_0, \frac{\partial w_0}{\partial x}, \frac{\partial w_0}{\partial y}, \psi_x, \psi_y \right]^T \tag{32}$$

Using shape functions, each of the unknowns is interpolated over the element as follows.

$$U^e(x,y) = \sum_{i=1}^{n} N_i^e(x,y) q_i^e \tag{33}$$

where n is the number of nodes (n=4), N_i^e is the shape function and superscript 'e' denotes elemental representation. Bilinear shape functions are used for u_0, v_0, ψ_x and ψ_y, whereas a 12 term cubic polynomial is used for the transverse displacement w_0. The variations of kinetic, strain and potential energies, in terms of the elemental quantities, are obtained and the elemental matrices are assembled leading to the following equations of motion.

$$M\ddot{q} + \overline{K}q = f + F_P \tag{34}$$

where the global mass and stiffness matrices are given by

$$M = \sum_{i=1}^{4} \left[\int_V \rho S^T S dV \right] \tag{35}$$

$$\overline{K} = \sum_{i=1}^{4} \left[\int_V B^T \overline{Q} B dV \right] \tag{36}$$

and the force vectors are as follows.

$$f = \sum_{i=1}^{4} \left[\int_A N^T p(x,y) dA \right] \tag{37}$$

$$F_P = \sum_{i=1}^{4}\left[\int_A N^T N^P dA\right] \tag{38}$$

In equations (35) to (38), the summation is performed over walls 1 through 4 (number of walls=4 for a box beam) and V and A represent volume and surface areas; respectively. The material density is denoted ρ and p(x,y) is the distributed load (such as, aerodynamic pressure). The matrix $\overline{Q}$ is the material stiffness matrix and matrices B and S relate the nodal degree of freedom vector to strains and displacements, respectively. The term N^T denotes transpose of the shape functions, N^P is the stress resultant due to piezoelectric actuators and F_P is the corresponding force vector. Since the accurate prediction of structural damping is difficult, it is ignored in the present analysis. Also, its effect is usually small on aeroelastic stability and ignoring it generally leads to conservative results [34].

3.1.2 Aeroelastic Analysis

The objective of the aeroelastic analysis is to obtain velocity and atmospheric density or altitude where the aeroelastic system is neutrally stable. The V-g (velocity - damping) method of flutter prediction [33] is the classical method which has been extensively used over the past decades. It assumes that the aeroelastic system performs a simple harmonic motion and uses the purely oscillatory air loads. Since these assumptions are valid at the flutter condition, this method yields accurate results for flutter boundary.

V-g method

The equations of motion for the wing structural-aerodynamic system is solved with the aeroelastic forces represented by the force vector f. Assuming simple harmonic

motion, wing elastic deformation and aeroelastic forces are represented by $q = \bar{q}e^{i\omega t}$ and $f = \bar{f}e^{i\omega t}$, respectively. Substituting the above into equation (34) yields

$$(-\omega^2 M + K)\bar{q} = \bar{f} \tag{39}$$

where the stiffness term, K, now also includes the piezoelectric actuation effects. The unsteady aerodynamic force, $\bar{f}$, can be expressed as a linear combination of $\bar{q}$ as follows.

$$\bar{f} = q_\infty F(i\omega)\bar{q} \tag{40}$$

where $F(i\omega)$ is the aerodynamic influence coefficient and q_∞ denotes freestream dynamic pressure. Substituting for $\bar{f}$ in equation (40) results in the following equation.

$$(-\omega^2 M + K - q_\infty F(i\omega))\bar{q} = 0 \tag{41}$$

Equation (41) represents an eigenvalue problem and the solution of the following determinant

$$\left|-\omega^2 M + K - q_\infty F(i\omega)\right| = 0 \tag{42}$$

provides the roots which determine the stability of the system. To solve the above problem, artificial damping, g, is introduced and equation (42) is rewritten as

$$\left|-\omega^2 M + (1+ig)K - q_\infty F(i\omega)\right| = 0 \tag{43}$$

The problem size for flutter solution can be reduced by using the modal approach. It is well known that only the low frequency modes govern wing flutter characteristics and the high frequency modes have little effect on the flutter solution [33]. Using the first several low frequency modes, equation (43) is transformed into modal coordinates and is rewritten as follows.

$$\left|-\omega^2 M^* + (1+ig)K^* - q_\infty F^*(i\omega)\right| = 0 \tag{44}$$

where M^*, K^* and F^* are the generalized mass, stiffness and aerodynamic influence coefficient, respectively. The generalized aerodynamic forces are computed using the constant-pressure lifting surface method [32] at a given Mach number for specified values of the reduced frequency *k*, assuming simple harmonic motion. This method is based on the linearized aerodynamic potential theory [33]. The lifting surface is divided into small trapezoidal panels, with unknown constant pressure, arranged in strips parallel to the freestream. The downwash boundary condition calculated from the deflection of structural modes is satisfied at mid-span three-quarter chord point of each panel. The procedure is implemented in the 'ZONA6' computer code [71] which is used in the present research. The solution of equation (44) yields the variations of damping and frequency with respect to the freestream velocity. At the flutter point, the artificial damping, g =0.

Laplace domain method

The V-g method gives accurate results at the flutter point, but it does not generate reliable frequency and damping histories since the assumed harmonic motion is not valid at other conditions. Also, this method requires iterative calculations to arrive at the 'matched flutter point', which poses difficulty in using it within an optimization procedure. The Laplace domain method of flutter analysis [34] produces valid damping and frequency history and, thereby, affords an insight into the physical phenomena leading to flutter. This method is non-iterative and suitable for automated optimization procedures. However, the Laplace domain method requires the air loads for arbitrary motions. Since aerodynamic calculations are well developed only for simple harmonic

motions, approximations are necessary to define air loads. These approximations reduce the accuracy of flutter prediction, but the method is still very useful.

Laplace transformation of the governing equation of motion (Equation (34)) yields the following.

$$(s^2M + K)q(s) = f(s) \tag{45}$$

where s denotes the complex Laplace variable. The aeroelastic load f(s) can be expressed as a linear combination of q(s) as follows.

$$f(s) = q_\infty F(p)q(s) \tag{46}$$

where p is the nondimensionalized Laplace variable and F(p) can be regarded as the aerodynamic transfer function. Substituting for q(s) in equation (45) gives

$$(s^2M + K - q_\infty F(p))q(s) = 0 \tag{47}$$

Equation (47) can be transformed into modal coordinates and rewritten, using several low frequency modes as follows.

$$(s^2M^* + K^* - q_\infty F^*(p))\xi(s) = 0 \tag{48}$$

where M^*, K^* and F^* are the generalized mass, stiffness and aerodynamic forces respectively and $\xi(s)$ denotes the generalized coordinate.

The unsteady aerodynamic forces are obtained assuming simple harmonic motion [32, 71] similar to the V-g flutter calculations. However, $F^*(p)$ contains transcendental terms when expressed as a function in the Laplace domain. To obtain a finite number of terms, the aerodynamic forces are approximated by a rational function of the

nondimensionalized Laplace variable p. Following the method of [35-36], the approximating function for $F^*(p)$ is expressed as

$$\hat{F}(p) = A_0 + A_1 p + A_2 p^2 + \sum_{l=1}^{n} (A_{l+2}) \frac{p}{p + b_l} \tag{49}$$

where n is the number of partial fractions (order of fit). The partial fractions approximate the time delays inherent in unsteady aerodynamics [36]. The denominator coefficients b_l in equation (49) are selected from the range of reduced frequencies for which unsteady aerodynamic forces are computed. Substituting ik for p along the imaginary axis, the coefficients, A_0, A_1, etc. are computed from the available generalized forces such that the approximation error is minimized in the least-squares sense. Substituting equation (49) into equation (48), the equations of motion are reduced to a series of 6N first-order equations [36] of the form

$$sX = AX \tag{50}$$

where N is the number of normal modes used. The eigenvalues of matrix A provide the roots of the flutter equation. For stability of the system, all real roots should be negative. At flutter condition, one of the roots is purely imaginary. The above procedure is implemented in the computer code 'Interaction Structures, Aerodynamics, and Controls' (ISAC) [72] and is used for flutter analysis in this research.

3.1.3 Aerodynamic Analysis

Lift and drag for the wing are calculated to define its aerodynamic efficiency (lift-to-drag ratio). The constant-pressure lifting surface method [32, 71], used for unsteady aerodynamic calculations, can also predict steady normal forces with the value of the reduced frequency being set to zero. Induced drag and lift are obtained by resolving the

normal force along the freestream and the direction perpendicular to it. The other two components of wing drag at high subsonic or transonic Mach numbers include skin-friction drag and compressibility (wave) drag.

The skin-friction drag arises from the viscous effects in the mostly turbulent boundary layer adjacent to the wing surface. First, a flat-plate skin-friction drag coefficient (C_f) is calculated, which is multiplied by a 'form factor' (FF) to account for the viscous separation effects. The flat-plate skin-friction coefficient depends upon the Reynolds number, the Mach number and the skin roughness. For turbulent flow, which is generally the case at high subsonic or transonic Mach numbers, the flat-plate skin-friction coefficient is determined using the Schlichting empirical formula, corrected to include the Mach number effect [40], as follows.

$$C_f = \frac{0.455}{(\log_{10} R)^{2.58}(1 + 0.144M^2)^{0.65}} \tag{51}$$

where M is the Mach number and the Reynolds number (R) is defined by

$$R = \rho V \ell / \mu \tag{52}$$

where ρ is the atmospheric density, V is the velocity, ℓ is the mean aerodynamic chord length and μ is the coefficient of viscosity. For relatively rough surfaces, the friction coefficient is higher. Therefore, a 'cut-off Reynolds number' is determined using the mean aerodynamic chord, ℓ, and a surface roughness parameter, κ.

$$R_{cut-off} = 44.62(\ell / \kappa)^{1.053} M^{1.16} \tag{53}$$

The lower of the cut-off Reynolds number and the actual Reynolds number is used in equation (51). The form factor for the wing is obtained as follows.

$$FF = \left[1 + \frac{0.6}{(x/c)_m}\left(\frac{t}{c}\right) + 100\left(\frac{t}{c}\right)^4\right]\left[1.34M^{0.18}(\cos\Lambda_m)^{0.28}\right] \tag{54}$$

where $(x/c)_m$ denotes the chordwise location of the airfoil maximum thickness point, $\left(\frac{t}{c}\right)$ is the airfoil thickness to chord ratio and Λ_m refers to sweep of the maximum thickness line. The skin-friction drag coefficient can now be calculated from the following equation.

$$C_{D_{skin-friction}} = \frac{C_f FF S_{wet}}{S_{ref}} \tag{55}$$

where

$$\frac{S_{wet}}{S_{ref}} = \left[1.977 + 0.52\left(\frac{t}{c}\right)\right] \qquad \left(\frac{t}{c}\right) > 0.05 \tag{56}$$

represents the ratio of 'wetted area' to 'reference area'.

The compressibility drag refers to the pressure drag resulting from increase in Mach number above low subsonic value. At high subsonic (or higher) Mach numbers, the local velocities on the upper surface of the wing may become sonic or even supersonic. This may lead to shock formation on the top of the wing which increases drag due to reduction in the total pressure through shock waves. Drag may also increase due to thickening or separation of the boundary layer as a result of the severe adverse pressure gradient caused by the presence of shocks. An empirical method, called the 'crest-critical Mach number method' [41], has been used in this research to obtain the compressibility drag. The 'crest' is the point on the airfoil upper surface to which the freestream is tangent. In this method, the freestream Mach number which gives sonic flow at or behind the crest of the airfoil is first determined. The crest-critical Mach number is a function of airfoil thickness-to-chord ratio, lift coefficient and wing sweep. At a Mach number 2 - 4 percent

(depending on wing sweepback angle) higher than the crest-critical Mach number, the drag rises abruptly. This Mach number is called the 'drag divergence Mach number', which can be determined from the crest-critical Mach number. The compressibility drag coefficient is then calculated using the ratio of freestream Mach number to the crest-critical Mach number and empirical data (based on existing transport aircraft) for the increment in drag.

3.2 Optimization Technique

The optimization techniques described next are suitable for multiobjective optimization with objective function/constraint approximation and continuous/discrete design variables.

3.2.1 K-S Function Approach

The K-S function technique [16] is used to efficiently integrate the objective function and constraints into a single envelop function. The resulting unconstrained nonlinear optimization problem is solved using the Broyden-Fletcher-Goldberg-Shanno (BFGS) algorithm [14]. The derivatives of the objective functions and the constraints, with respect to the design variables, are calculated using the forward finite difference technique.

Using the K-S approach, each of the original objective functions is transformed into reduced objective functions as follows.

$$F_i^*(\Phi) = \frac{F_i(\Phi)}{F_i^0} - 1.0 - g_{max} \le 0, \qquad i=1,...,NOBJ \tag{57}$$

where F_i^0 is the value of the original objective function F_i calculated at the beginning of the cycle, Φ is the design variable vector and g_{max} is the value of the largest constraint and is held constant during each cycle. It is assumed that the constraints $g_j(\Phi)$ (j = 1, 2, ··· , NC) are scaled to lie between -1 and 1. The reduced objective functions are analogous to constraints. A new constraint vector $f_m(\Phi)$ (m=1,.., M where M = NC + NOBJ) is defined by combining the original constraints and the reduced objective functions. The new objective function is defined as follows.

$$F_{KS}(\Phi) = f_{max} + \frac{1}{\rho}\log_e \sum_{m=1}^{M} e^{\rho(f_m(\Phi) - f_{max})} \tag{58}$$

where f_{max} is the maximum value of $f_m(\Phi)$ and remains constant during the optimization cycle. The scalar multiplier ρ is similar to draw-down factor of penalty function methods. Larger values of ρ move the K-S function curve closer to the largest constraint [14]. The initial value of this parameter is user supplied and its value is increased as the optimization proceeds. The new objective function $F_{KS}(\Phi)$, which represents an envelope function representing the original objective functions and constraints, can now be minimized using any unconstrained optimization technique. In this research, the search direction vector is obtained using the Broyden-Fletcher-Goldberg-Shanno (BFGS) algorithm which is a quasi-Newton technique [14]. This is followed by a one-dimensional search for the minimum of the K-S function using the three point quadratic approximation for step length calculation [14].

3.2.2 Approximation Technique

During the one-dimensional search to minimize the composite K-S function, several evaluations of the objective functions and constraints are necessary. It is computationally expensive to carry out exact analysis all the time. Therefore, an approximation technique

is used to provide objective function and constraint values during the one-dimensional minimization. The two-point approximation technique [18], which has been found to be well suited for nonlinear optimization problems, is applied. This technique uses the gradient information from the previous and current design cycles to obtain the exponent used in the expansion. The technique is formulated as follows.

$$\hat{F}(\Phi) = F(\Phi_0) + \sum_{n=1}^{NDV}\left[\left(\frac{\phi_n}{\phi_{0n}}\right)^{p_n} - 1.0\right]\frac{\phi_{0n}}{p_n}\frac{\partial F}{\partial \phi_n}(\Phi_0) \tag{59}$$

where $\hat{F}(\Phi)$ is the approximation to the objective function $F(\Phi)$ at a neighboring design point Φ (vector of ϕ_n design variables) based on its values and gradients at the current design point Φ_0 and the previous design point Φ_1. The exponent p_n, considered as a 'goodness of fit' parameter, explicitly determines the trade-offs between traditional and reciprocal Taylor series expansions. In the limiting case of $p_n = 1$, the expansion is the first order Taylor series, and when $p_n = -1$, the two-point exponential approximation reduces to the reciprocal expansion form. The exponent p_n is obtained from the following equation.

$$p_n = \frac{\log_e\left\{\frac{\partial F}{\partial \phi_n}(\Phi_1)\right\} - \log_e\left\{\frac{\partial F}{\partial \phi_n}(\Phi_0)\right\}}{\log_e\{\phi_{1_n}\} - \log_e\{\phi_{0_n}\}} + 1.0 \tag{60}$$

The exponent p_n is defined to lie between +1 and -1. If any singularity is encountered, the exponent is set to +1 to obtain linear Taylor series expansion. A similar approximation is obtained for the constraint vector too.

3.2.3 Hybrid Optimization

The inclusion of both continuous and discrete design variables significantly complicates the optimization problem. This is because the discrete design variables are not compatible with traditional gradient based optimization methods. Similarly, the continuous variables are not compatible with combinatorial optimization methods, such as branch and bound techniques, which require discrete values to operate. Therefore, a hybrid optimization technique developed by Seeley and Chattopadhyay [19] which combines both types of design variables is used.

The general continuous/discrete optimization problem can be mathematically stated as follows.

$$\text{Minimize } f(\Phi_c, \Phi_d) \tag{61}$$

$$\text{Subject to } g(\Phi_c, \Phi_d)_j \leq 0 \qquad (j = 1, 2, \ldots, \text{NCON}) \tag{62}$$

$$\text{Side constraints } \quad \Phi_{c_l} \leq \Phi_c \leq \Phi_{c_u}$$

$$\Phi_d \in [\Phi_{1_q}, \Phi_{2_q}, \Phi_{3_q}, \ldots, \Phi_{d_q}] \tag{63}$$

where f is the objective function, g_j are the constraints, Φ_c are the continuous design variables and Φ_d are the discrete design variables which can be selected from among a set of q preselected values. The hybrid optimization procedure is based on Simulated Annealing (SA) [73] where the design space is sampled by repeatedly perturbing the discrete design variables. At each iteration of the SA procedure, the objective function is minimized with respect to the continuous variables using a BFGS search algorithm [14]. This significantly improves the efficiency of the hybrid algorithm by directing the search using the gradient information when available. The constrained problem is formulated using a penalty function approach [14].

4. MDO Applications for Smart Composite Wings

The analysis techniques and optimization methods described in the preceding chapter have been applied to the design of a composite wing, with and without smart materials [74-80]. The aeroelastic stability of composite wings was investigated using the V-g method in [74-75] and the Laplace domain method in [76]. A hybrid optimization technique (combining both continuous and discrete design variables) was adopted for the wing designs investigated in [77-78]. Multidisciplinary optimizations of business jet type composite wing and smart composite wing are reported in [79] and [80], respectively. These applications, from the current research, are presented in the following sections.

4.1 Aeroelastic Stability Using Higher-Order Laminate Theory

First, it is necessary to investigate the effect of higher-order theory on aeroelastic stability of composite wings. To demonstrate this, aeroelastic analysis is performed for a simple scaled wing model shown in Figure 5. The wing semi-span and root chord are 90 and 20 inch, respectively. The aspect ratio and the taper ratio of the wing are 12 and 0.5, respectively, and the mid-chord is unswept. It is assumed that the box beam is the principal load-carrying member of the wing which extends through the entire semi-span and is fixed at the root. The width and the height of the box beam are assumed to be 50 and 10 percent of the local wing chord; respectively. The center of the beam coincides with the mid-chord of the wing. Each wall of the box beam is made up of eight unidirectional composite laminates (each consisting of several plies with identical orientation), which are symmetric about the mid-surface. The composite material (Gr-Ep T300) properties are listed in Table 1 [81]. The material density is multiplied by a factor of eight to account for the non-structural mass of the wing. The walls have a uniform spanwise thickness of 0.80 inch. The top and the bottom walls have $(0/90/30/30)_S$ lay-up,

while the vertical wall ply angles are $(45/-45/45/-45)_S$. The direction of positive ply angle is indicated in Figure 5.

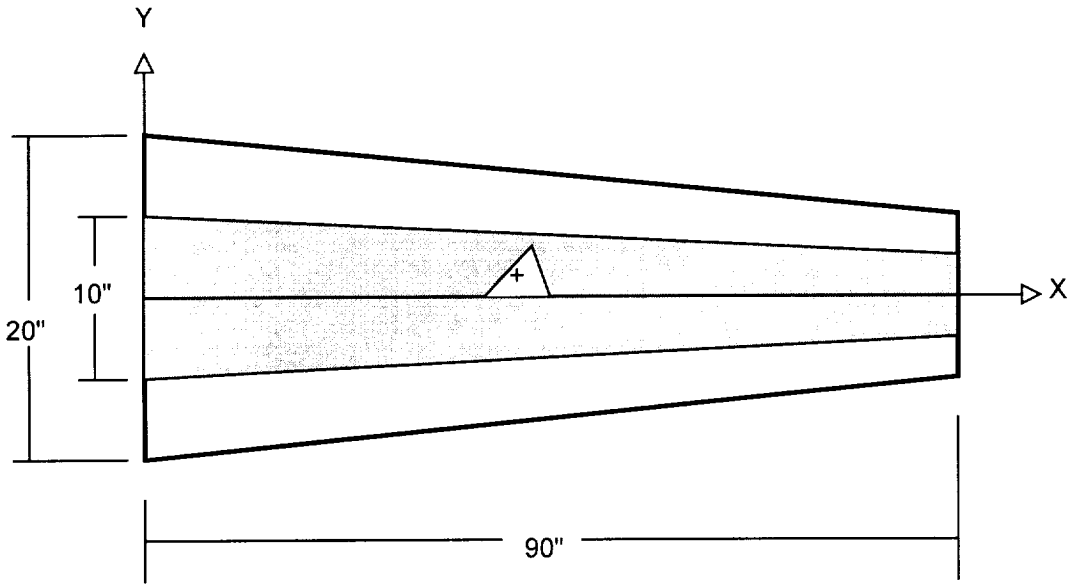

Figure 5. Wing planform for aeroelastic stability analysis

Table 1. Material properties (Gr-Ep T300)

E_L (msi)	19.00
E_T(msi)	1.50
G_{LT}(msi)	1.00
G_{TT}(msi)	0.90
ν_{LT}	0.22
ρ (slugs/in^3)	$1.68*10^{-3}$

The structural analysis of the box beam is performed with 15 elements spanwise and a single element chordwise. The structural degrees of freedom for the box beam are 664 and 844 using the CLT and the present approach, respectively. The first ten normal modes of vibration are used in the subsequent analysis and the natural frequencies are presented in Table 2. Although, bending-torsion coupling exists due to the ply

orientations used, for identification purposes only the dominant mode shapes are indicated in Table 2. Table 2 shows that the natural frequencies of the beam bending modes (B1, B2, B3, B4 and B5) are somewhat higher for the CLT compared to the present approach. The torsional mode (T1) exhibits the largest difference in the natural frequency (about three hertz), the CLT value being higher again. This is due to the fact that the transverse shear stresses are ignored by the CLT, but are efficiently modeled in the present approach. The frequencies of the chordwise bending modes (C1, C2, C3 and C4), which are not used in the flutter analysis, are identical using both theories.

Table 2. Natural frequency (Hz) and modes

Mode Number	Mode Type	Higher-order Theory	Classical Theory
1	B1	5.34	5.37
2	C1	18.17	18.17
3	B2	27.75	27.94
4	B3	71.42	71.99
5	C2	84.07	84.07
6	B4	130.71	132.36
7	T1	134.43	137.23
8	C3	202.32	202.32
9	B5	205.75	207.70
10	C4	256.42	256.42

Legend: B- Beam bending, C- Chordwise bending, T- Torsion

Mode shapes for the first beam bending (Mode 1) and the first torsion (Mode 7) are presented in Figures 6 and 7 for the CLT and Figures 8 and 9 for the present theory. The

mode shapes are normalized such that the generalized mass equals unity. Mode 1 is a pure beam bending mode, whereas Mode 7 is a coupled fourth bending/first torsion mode in both cases. These two modes are selected for comparison because of their contribution in wing flutter as will be shown later. The response of Mode 1 is nearly identical (as are the natural frequencies, see Table 2) using both theories, but differences are observed in Mode 7. The present approach shows somewhat higher bending displacements in this mode, whereas the torsional displacements are slightly lower compared to CLT.

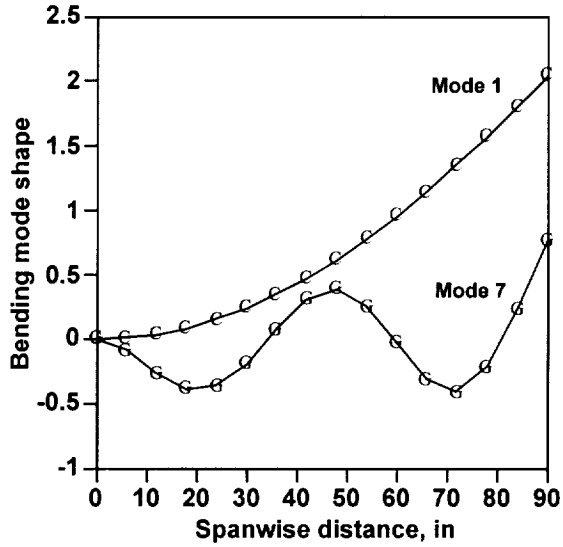

Figure 6. Bending mode shape (CLT)

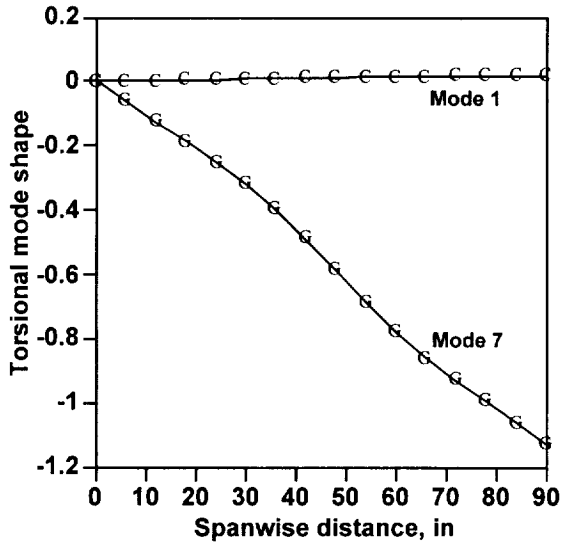

Figure 7. Torsional mode shape (CLT)

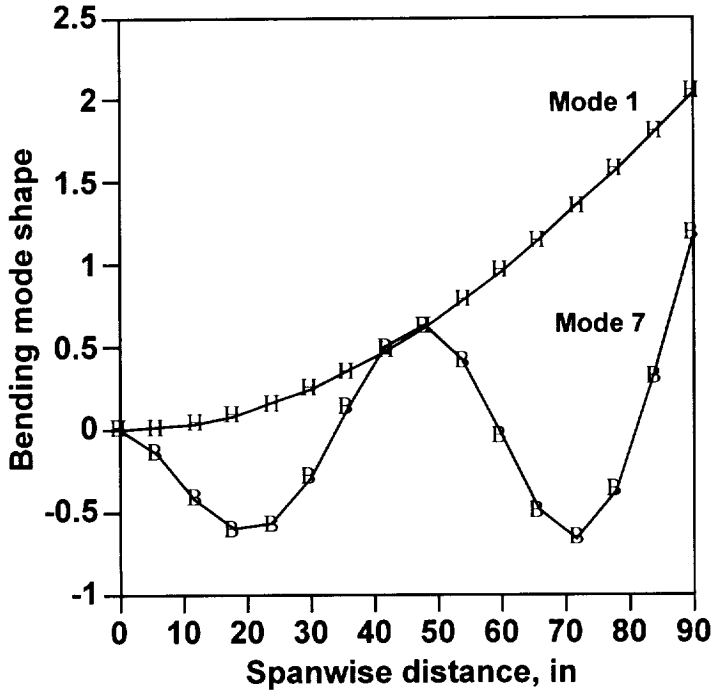

Figure 8. Bending mode shape (present theory)

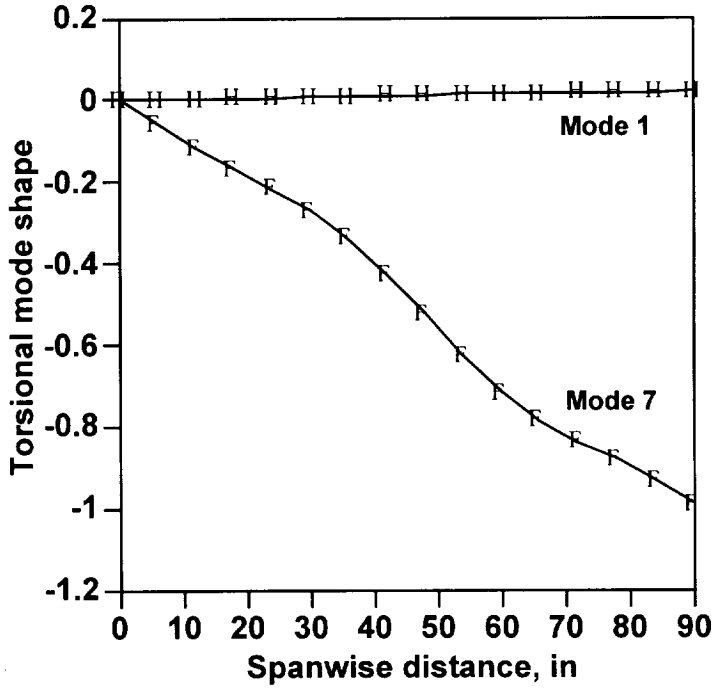

Figure 9. Torsional mode shape (present theory)

The generalized aerodynamic forces are computed at M=0.95 with the wing divided into 48 panels. Flutter solution is obtained using the V-g method for various values of the atmospheric density (an input parameter) till the flutter speed and the air speed match each other ('matched flutter point'). The flutter results, in terms of variations of frequency and damping with airspeed, are presented in Figures 10 and 11 using both CLT and the present approach.

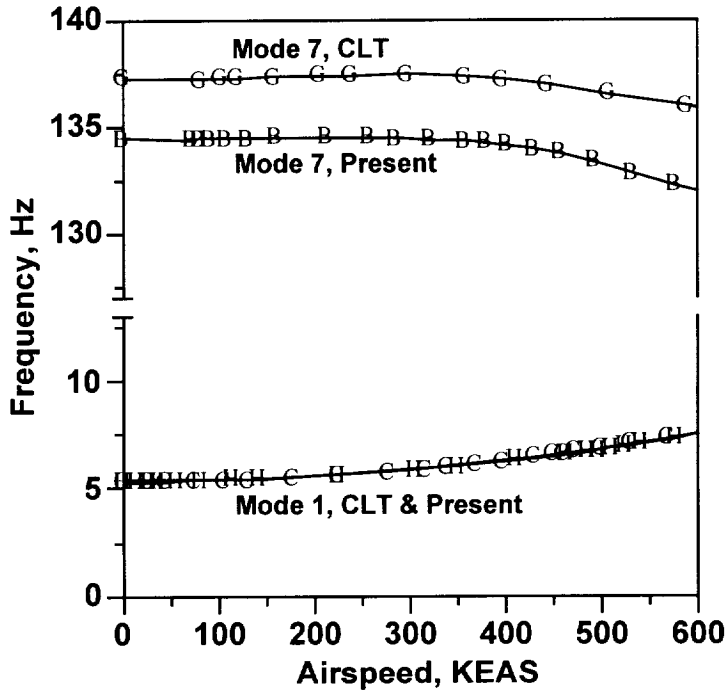

Figure 10. Frequency vs. Airspeed

Flutter is often caused by the coupled bending and torsional motion of aircraft wings, wherein the frequencies of these two modes come close or coalesce around the critical flutter speed and the damping of either of the modes goes to zero [82]. Figure 10 shows the tendency of the first bending (Mode 1) and the first torsion (Mode 7) modes to get close to each other. For the present approach, the separation between the two frequencies is smaller and the tendency to come close is more pronounced compared to the CLT.

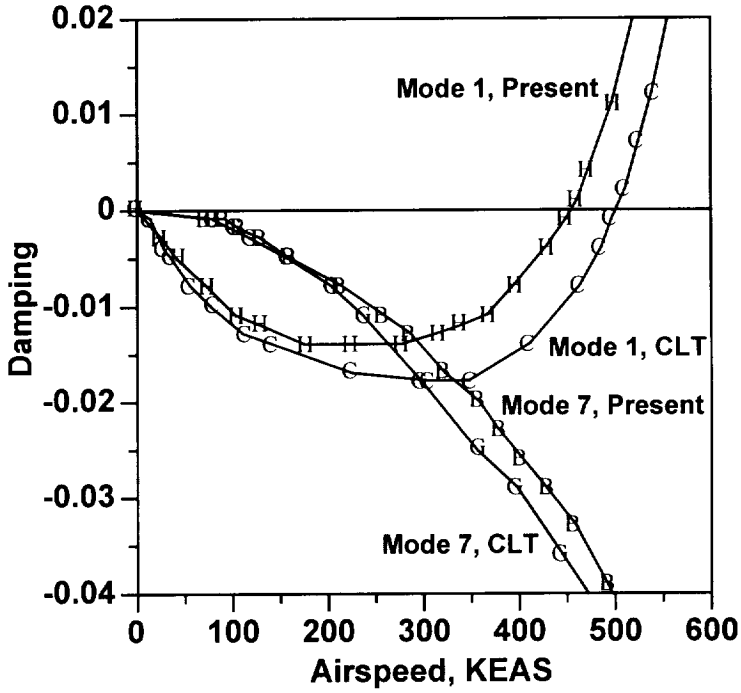

Figure 11. Damping vs. Airspeed

As a result, the damping of one of the modes (Mode 1) becomes zero at lower airspeed, as predicted by the present approach (Figure 11). The flutter speeds, using the present approach and the CLT, are 455 and 503 KEAS, respectively. This significant difference in flutter speed of 48 KEAS (about 10 percent) is very critical. Further, it is important to note that the CLT results are nonconservative. This establishes the need for using refined structural modeling techniques since flutter is a catastrophic phenomenon.

4.2 Effects of Ply Orientations on Aeroelastic Stability

To study the effects of elastic couplings on aeroelastic stabilty of composite wings, various ply orientations are investigated. The wing geometry is the same as in the previous section (Figure 5), with the exception that the walls now have an uniform

spanwise thickness of 0.16 inch and non-structural masses are not included in the analysis.

Three types of ply lay-ups, $(0/90/0/90)_S$, $(0/90/30/30)_S$ and $(0/90/-30/-30)_S$, are used for the top and the bottom flanges of the wing. The vertical webs have the cross-ply orientations of $(0/90/0/90)_S$ in all cases. For the cross-ply lay-up there is no elastic coupling, whereas the $(0/90/30/30)_S$ orientation displays negative bending-twist coupling, that is, upward bending causes nose down twist. The stacking sequence $(0/90/-30/-30)_S$ displays positive bending-twist coupling, that is, upward bending generates nose up twist. The structural analysis of the box beam is performed with 10 elements spanwise and a single element chordwise. The first six normal modes of vibration are used in the subsequent analysis. The natural frequencies and the associated modes are listed in Table 3. The first, third and fourth modes are beam bending modes and the fifth mode represents the first torsion mode in all cases. The second and the sixth modes are chordwise bending modes for $(0/90/30/30)_S$ and $(0/90/-30/-30)_S$ orientations. For the cross-ply case, the second mode is a chordwise bending mode, whereas the sixth mode is a torsion mode.

Table 3. Natural frequency (rad/sec) and modes for different ply lay-ups

Mode	$(0/90/0/90)_S$	$(0/90/-30/-30)_S$	$(0/90/30/30)_S$
1	75, B	66, B	66, B
2	289, C	269, C	269, C
3	331, B	309, B	309, B
4	761, B	738, B	738, B
5	875, T	1028, T	1028, T
6	1134, T	1195, C	1195, C

Legend: B- Beam bending, T- Torsion, C- Chordwise bending

The generalized aerodynamic forces are computed at M=0.8 for values of the reduced frequency between 0 and 1. The wing is divided into 48 panels. The Laplace domain method is used in the flutter calculations. Rational function approximation of the generalized aerodynamic forces (tabular data) is performed using four denominator coefficients. These coefficients are selected to be 0.2, 0.4, 0.6 and 0.8 and produce a very good fit. Figures 12-15 show a comparison of the tabular data with s-plane fit for real and imaginary parts of the two of the aerodynamic influence coefficients, F(1,1) and F(2,2). These comparisons are typical of the rest of the coefficients. The approximation error for the aerodynamic forces is generally less than one percent and it never exceeds six percent. Total least-square error for the rational function approximation equals 0.36 percent.

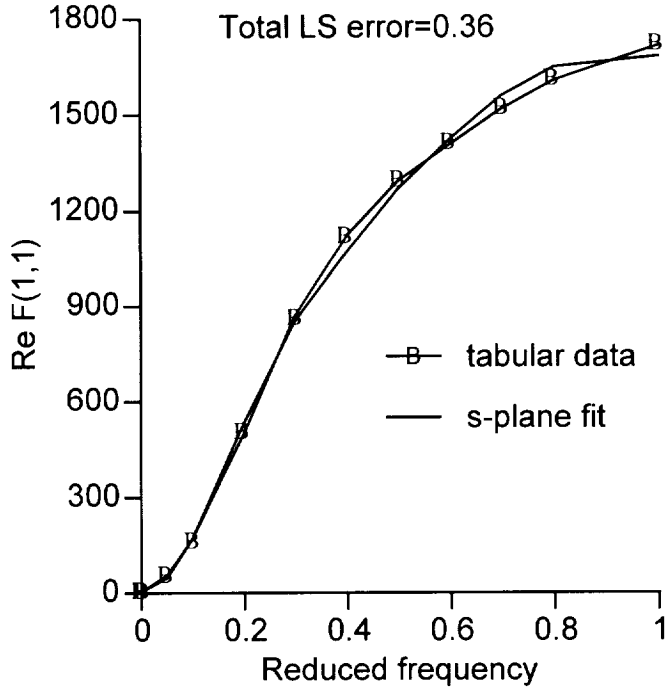

Figure 12. RFA of real F(1,1) aerodynamic coefficient

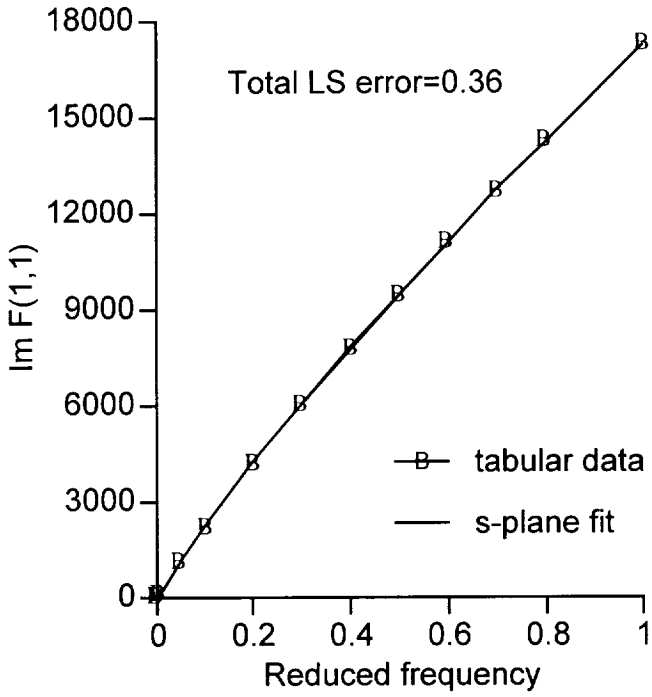

Figure 13. RFA of imaginary F(1,1) aerodynamic coefficient

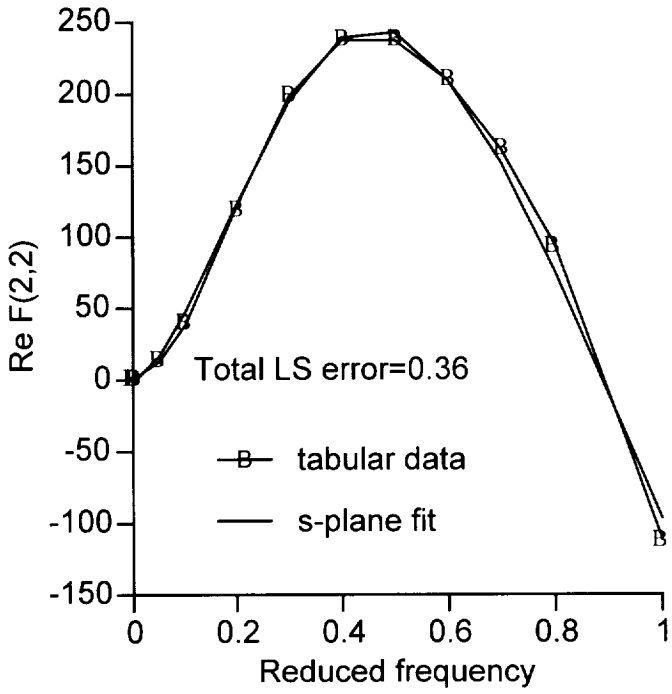

Figure 14. RFA of real F(2,2) aerodynamic coefficient

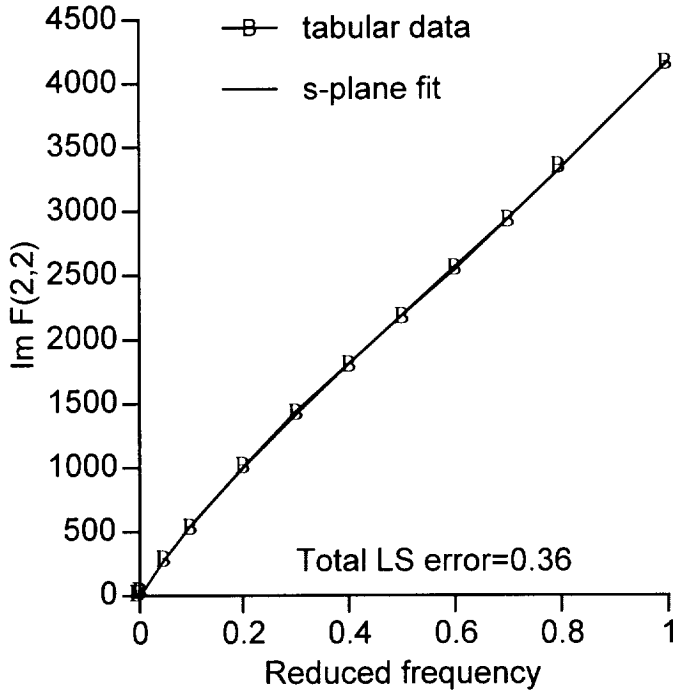

Figure 15. RFA of imaginary F(2,2) aerodynamic coefficient

The eigenvalues of the characteristic equation vary with dynamic pressure. A root locus constructed by varying the altitude for a given Mach number gives flutter dynamic pressure when one of the real roots becomes zero and the imaginary root is non-zero. Divergence is indicated when both the real and the imaginary roots of any one mode reduce to zero. The variations of frequency and damping with dynamic pressure provide an insight into flutter and divergence onset. Figures 16-24 show the dynamic pressure root locus, frequency history and damping history for the three different ply lay-ups.

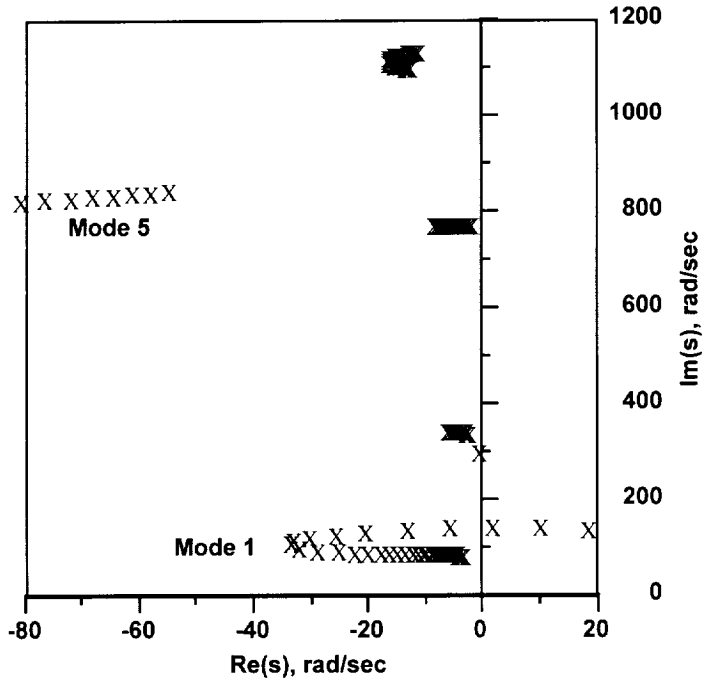

Figure 16. Dynamic pressure root locus for $(0/90/0/90)_S$ ply angle

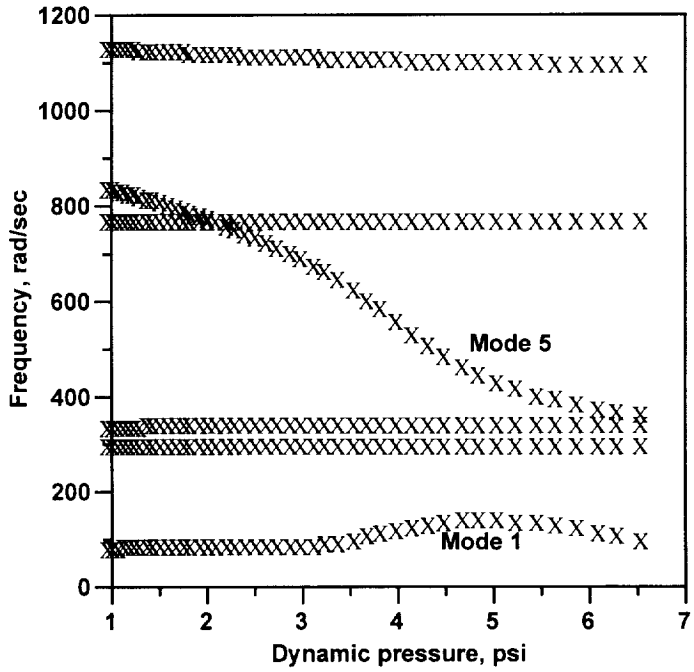

Figure 17. Frequency versus dynamic pressure for $(0/90/0/90)_S$ ply angle

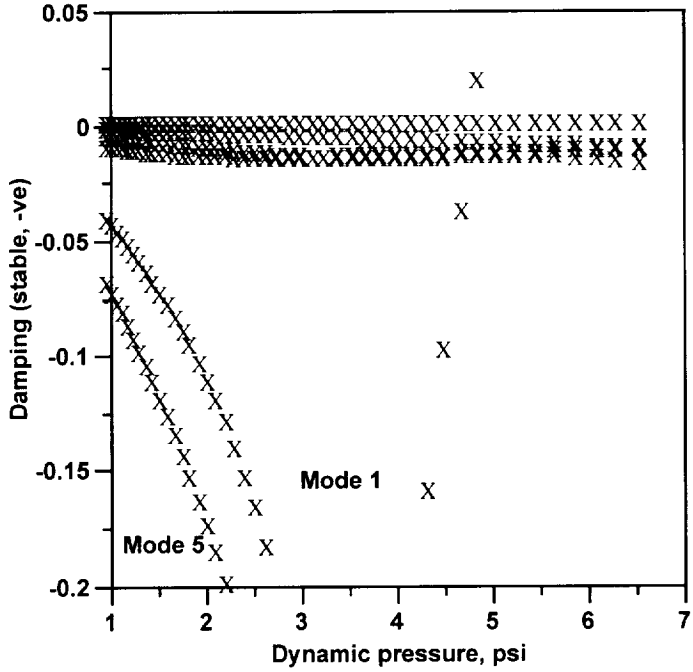

Figure 18. Damping versus dynamic pressure for $(0/90/0/90)_S$ ply angle

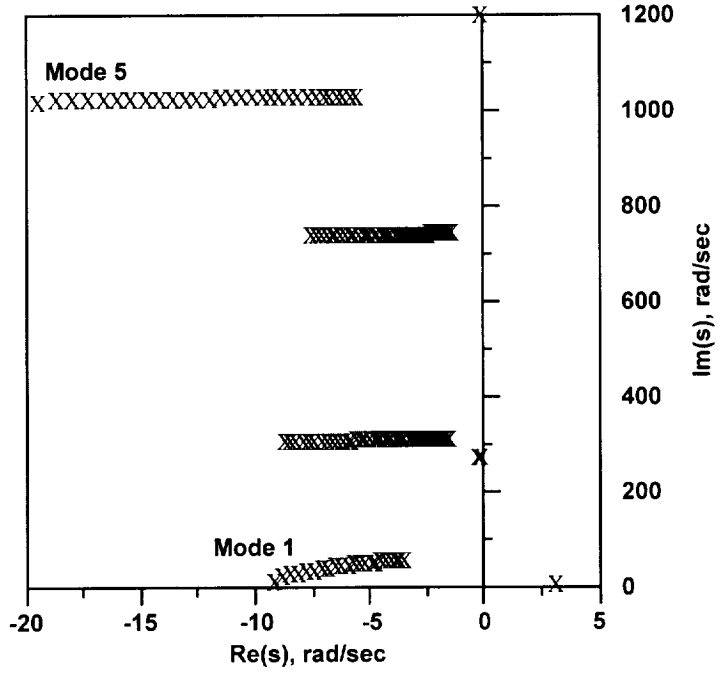

Figure 19. Dynamic pressure root locus for $(0/90/-30/-30)_S$ ply angle

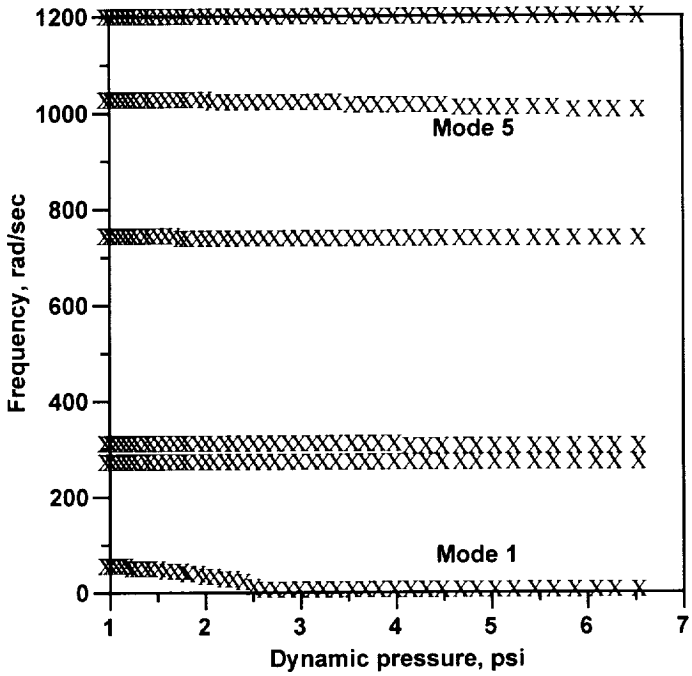

Figure 20. Frequency versus dynamic pressure for $(0/90/-30/-30)_S$ ply angle

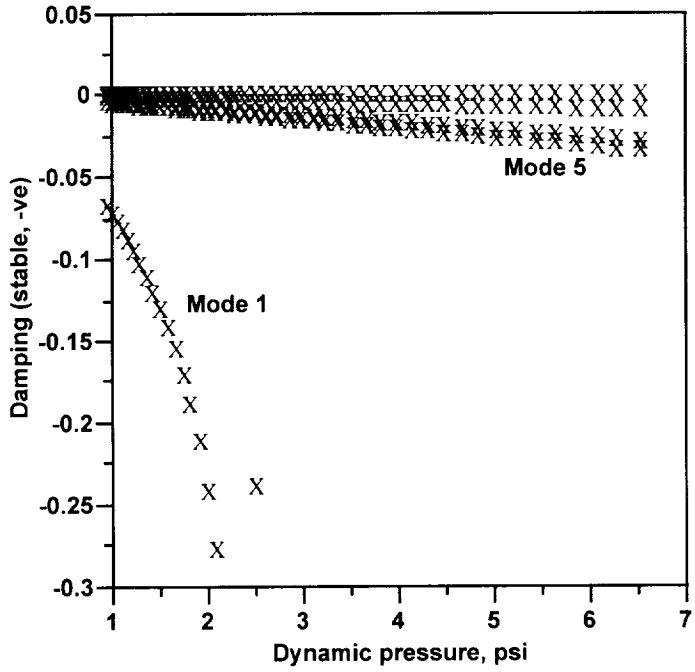

Figure 21. Damping versus dynamic pressure for $(0/90/-30/-30)_S$ ply angle

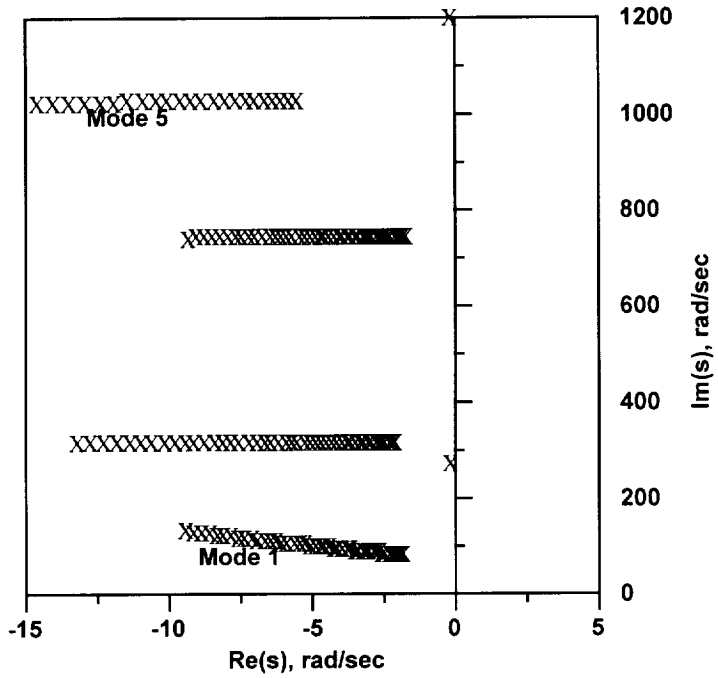

Figure 22. Dynamic pressure root locus for $(0/90/30/30)_S$ ply angle

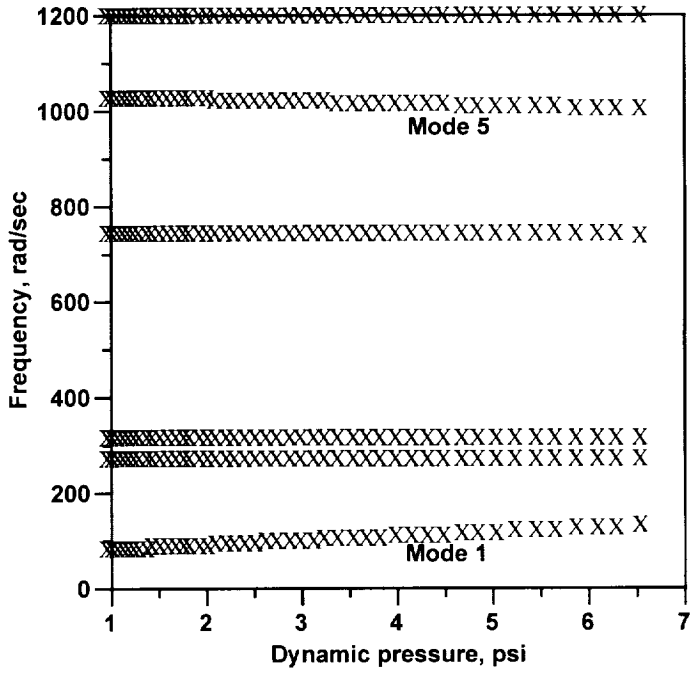

Figure 23. Frequency versus dynamic pressure for $(0/90/30/30)_S$ ply angle

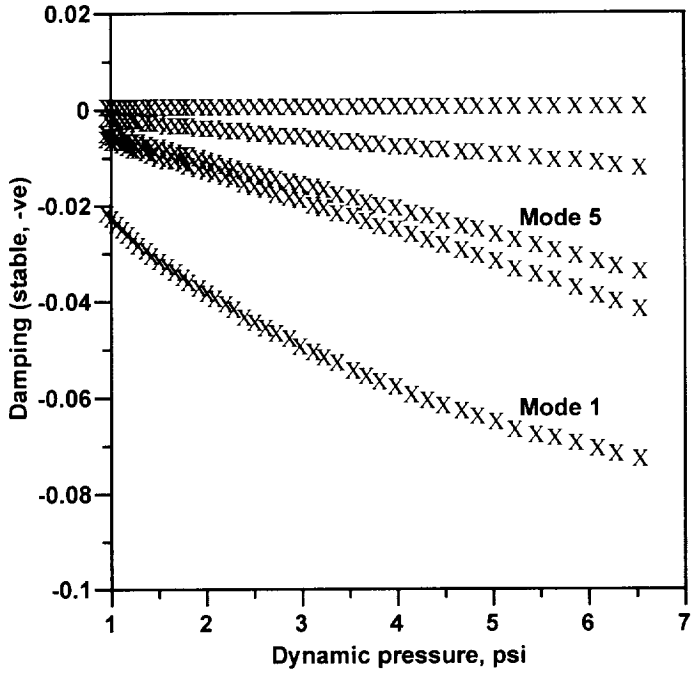

Figure 24. Damping versus dynamic pressure for $(0/90/30/30)_S$ ply angle

The cross-ply lay-up wing with $(0/90/0/90)_S$ ply orientation flutters at 4.88 psi when the frequencies of the first and the fifth modes come close and the damping of the first mode becomes zero (Figures 16-18). This lay-up has uncoupled elastic modes and the fifth mode is the first torsion mode for this wing. The wing with $(0/90/-30/-30)_S$ ply orientation does not show flutter, but due to a positive bending-twist coupling, it is prone to divergence. As the flight dynamic pressure increases, the frequency and the damping of the first bending mode reduce to zero at 2.66 psi (Figures 19-21). For the wing with $(0/90/30/30)_S$ ply angles, flutter or divergence is not encountered at the Mach number investigated (Figures 22-24). As mentioned earlier, this lay-up has negative bending-twist coupling which prevents divergence. Similar trends for the effects of ply orientation on flutter and divergence have been observed by other researchers [83].

4.3 Application of Hybrid Optimization Technique

The hybrid optimization technique has been applied in the continuous/discrete design variable optimization of a composite wing. The wing weight is used as objective function which is minimized with constraints on flutter/divergence speed and stresses at the wing root due to the specified air loads. Wing root chord and wall thickness are used as continuous design variables, whereas the ply orientations are treated as discrete variables.

4.3.1 Optimization Problem

The wing geometry, for this optimization problem, has unswept mid-chord (similar to Figure 5), an aspect ratio of 20 and a taper ratio of 0.5. The root chord is varied during the optimization and consequently, the wing span and area also vary. The objective is to minimize the weight of the box beam which represents the structural member in the wing. Therefore, in the optimization problem,

$$f = \overline{W} \tag{64}$$

where $\overline{W}$ is the weight of the box beam. The weight of the remaining components in the wing, such as the skin, is not considered in this work. Constraints are placed on the flutter speed and the maximum allowable stresses. The flutter/divergence speed (V_f) is constrained to be greater than 450 knots equivalent air speed (KEAS) at a flight condition of Mach=0.7 at sea level. This constraint is expressed as follows.

$$g_1 = 1 - \frac{V_f}{450} \leq 0 \tag{65}$$

The Tsai-Wu failure criterion [84] is imposed on the critical ply stresses at the root section where material failure is most likely to occur. The criterion states that failure initiates when the following inequality is violated.

$$F_c = F_i\sigma_i + F_{ij}\sigma_i\sigma_j \leq 1 \quad (i,j = 1,2,...,6) \tag{66}$$

where σ_i represents stresses in the material coordinate system and Fi and Fij are related to the tensile and compressive yield strengths of the material (Table 4). This constraint is expressed as follows.

$$g_2 = F_c - 1 \leq 0 \tag{67}$$

The static lift and drag are computed empirically [40] for the above flight condition at an angle of attack of 3.5°. This results in a lift force of 2350 lb and a drag force of 110 lb for the reference wing. This load is assumed to remain constant during the optimization. The spanwise load distribution is assumed to be elliptical over the wing planform. The root chord (c_r) is defined as a continuous design variable as follows.

$$c_r = \phi_1 \qquad 15" \leq \phi_1 \leq 25" \tag{68}$$

where the upper and lower bounds are also indicated above. The actual dimensions of the wing, such as the semi-span (s), the tip chord (c_t) and the wing area (A) are all computed from c_r so as to retain the aspect ratio and the taper ratio values mentioned earlier. The box beam is constructed from Carbon-PEEK composite material [81]. Material properties are presented in Table 4.

The box beam walls are assumed to be made of several unidirectional composite plies with thickness t_p=0.005". The quantity N, which denotes the number of two-ply layers in each laminate, is an integer value and is defined as a discrete variable

$$N = \phi_2 \tag{69}$$

where ϕ_2 = [4,5,6,..,14]. The box beam wall thickness, h, is then determined as

$$h = 2Nt_p \tag{70}$$

where it is assumed that all four walls have the same thickness. Therefore, the total number of plies in each wall is $8 \leq 2N \leq 28$ and h ranges between values of $0.04" \leq h \leq 0.14"$.

Table 4. Material properties (Carbon-PEEK)

E_L (msi)	19.40
E_T(msi)	1.29
G_{LT}(msi)	0.74
G_{TT}(msi)	0.50
gLT	0.28
density (slug/inch^3)	1.8×10^{-3}
Ultimate Strengths	
XT(ksi)	309.0
XC(ksi)	160.0
YT(ksi)	11.6
YC(ksi)	29.0
S(ksi)	23.2

Four design variables $(\phi_3,\phi_4,\phi_5,\phi_6)$ are used to describe the stacking sequence in each of the box beam walls as follows.

Top wall $[\theta_1/\theta_2]_N = [\phi_3/\phi_4]_N$

Bottom wall $[\theta_1/\theta_2]_N = [-\phi_3/-\phi_4]_N$

Left side wall $[\theta_1/\theta_2]_N = [\phi_5/\phi_6]_N$

Right side wall $[\theta_1/\theta_2]_N = [-\phi_5/-\phi_6]_N$

where the material axes for the plies in each wall are referenced to their respective local coordinate systems (Figure 3). In the global coordinate system, the top and the bottom walls have the same ply angles, as is the case for the two side walls. The ply angles are allowed to vary from within a range of pre-selected values ϕ_d=[-45°, 0°, 45°, 90°]. All four walls are assumed to have the same thickness, which does not vary along the span or the chord.

4.3.2 Results and Discussions

Results obtained using the hybrid optimization procedure are presented in Table 5 and in Figures 25-28. Optimization results are compared with a reference design, which is selected based on engineering judgment. It should be noted that the optimum design is independent of the initial design due to the probabilistic nature of the hybrid optimization procedure. The penalty function optimization iteration history is presented in Figure 25 at each iteration of the simulated annealing algorithm which consists of several BFGS evaluations. Both the trial designs and the best design obtained are presented.

Table 5 Hybrid optimization results

	Reference	Optimum
Number of plies	28	18
Root chord (in.)	15.0	15.4
Wall thickness (in)	0.14	0.09
Stacking sequence		
top and bottom walls	[0°/90°]14	[0°/-45°]9
side walls	[45°/-45°]14	[0°/0°]9
Natural frequency (hz)	9.4, 34.1, 50.7, 116.9, 154.7, 163.6	8.75, 34.7, 46.8, 107.7, 159.5, 170.1
Flutter point	29 hz, 2nd mode	74 hz, 5th mode

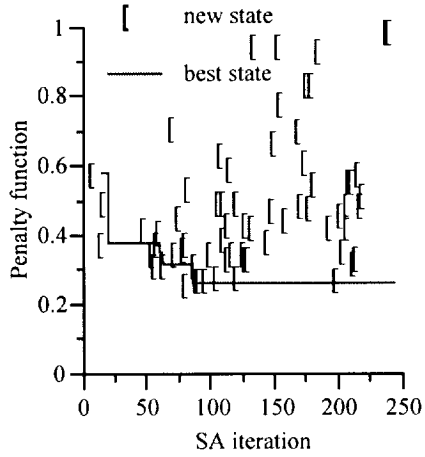

Figure 25. Penalty function iteration history

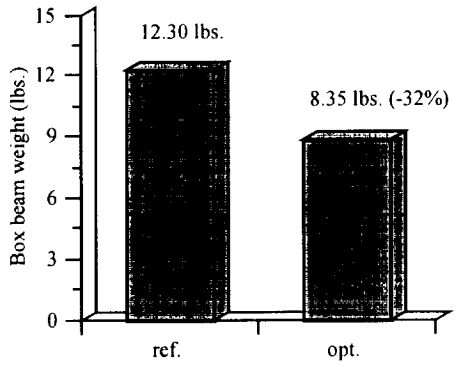

Figure 26 Weight reduction through hybrid optimization

Initially, the flutter constraint is violated which results in very large values of the penalty function which are not presented due to the scale of the graph. Due to heuristic nature of the optimization algorithm, a large number of function evaluations are required which make it computationally expensive. The optimum state is reached in less than 100 iterations and the optimization procedure is terminated after 250 iterations since no better design could be found. There is a significant reduction in the weight of the structural member of the wing (32 percent, Figure 26) along with a large improvement in the flutter speed (75 percent, Figure 27) due to the optimization. The Tsai-Wu stress criterion is satisfied by the reference as well as the optimal design (Figure 28). Since the wing root chord for the reference and the optimal wings are nearly same (Table 5), weight reduction is due to the fewer number of plies in the optimal wing. Through optimization of the stacking sequence, even a lower wall thickness provides higher flutter speed.

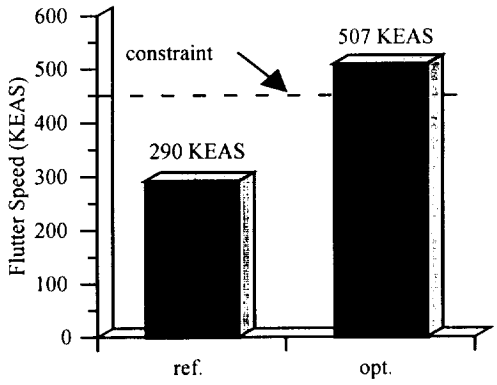

Figure 27. Flutter speed constraint for hybrid optimization.

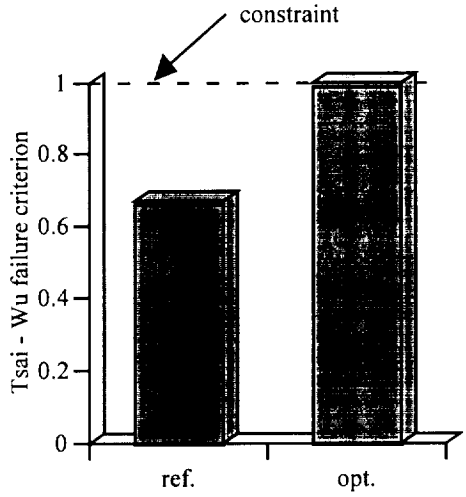

Figure 28. Tsai-Wu failure criterion for hybrid optimization

Study of the frequencies and modes for flutter show important trends (Table 6). For the reference wing, the second mode, which is a coupled bending and lag mode with a natural frequency of 34 Hz, flutters at 29 Hz. The first torsion mode is the sixth mode with a natural frequency of 164 Hz. At the flutter condition, the frequencies of the second and the sixth modes almost coalesce and the sixth mode also flutters at a slightly higher speed. For the optimal wing, flutter occurs at the fifth mode (at 74 Hz), which is the first torsion mode with the natural frequency of 160 Hz. The first four modes are

bending or coupled bending/lag modes. Thus optimization essentially stiffens the bending modes to increase the flutter speed.

Since the aspect ratio and taper ratio are fixed in this study, smaller root chord also means smaller span and lower wing area. The optimal value of the wing root chord is very near to the minimum value specified to achieve higher stiffness. This trend is expected in the absence of other design considerations such as wing loading (which affects landing/take-off speed, maneuverability etc.) and internal fuel volume.

4.4 MDO of Composite Wings

The developed MDO procedure with refined analysis and optimization technique (gradient bassed) is applied to the design of a composite wing. The wing configuration of a high speed business jet type airplane is selected for the optimization. Though the developed procedure is capable of handling multiple objective functions (and constraints), the example considered here includes only one objective function (with two constraints). The Laplace domain method of flutter analysis is used in this optimization.

4.4.1 Optimization Problem

The objective is to minimize the weight (W) of the box beam which represents the load carrying structural member of the wing. The cruise Mach number and altitude are assumed to be 0.85 and 26000 ft, respectively. In accordance to established design practice, the flutter/divergence speed is required to exceed 1.20 times the cruise speed. Therefore, the flutter/divergence dynamic pressure (q_f) is constrained to be at least 3.7 psi. Constraints are imposed on the maximum allowable stresses due to static loading of the wing corresponding to a 3g maneuver. An elliptic spanwise load distribution is assumed. The Tsai-Wu failure criterion [84] is imposed on the ply stresses at the root

section. The objective function and constraints are expressed in a similar manner as in the previous section (Equations (64) - (67)). The composite ply angles and laminate thicknesses are used as continuous design variables.

4.3.2 Results and Discussions

The selected reference wing has aspect ratio of 10, taper ratio of 0.35 and mid-chord sweep of 30° (Figure 29). The wing geometry is held fixed during optimization. The width of the box beam is assumed to equal half the wing chord. The wing thickness-to-chord ratio is assumed to be 12 percent, which accommodates the box beam with height to width ratio of 20 percent. The box beam is constructed from Carbon-PEEK composite material [81] whose properties are presented in Table 4.

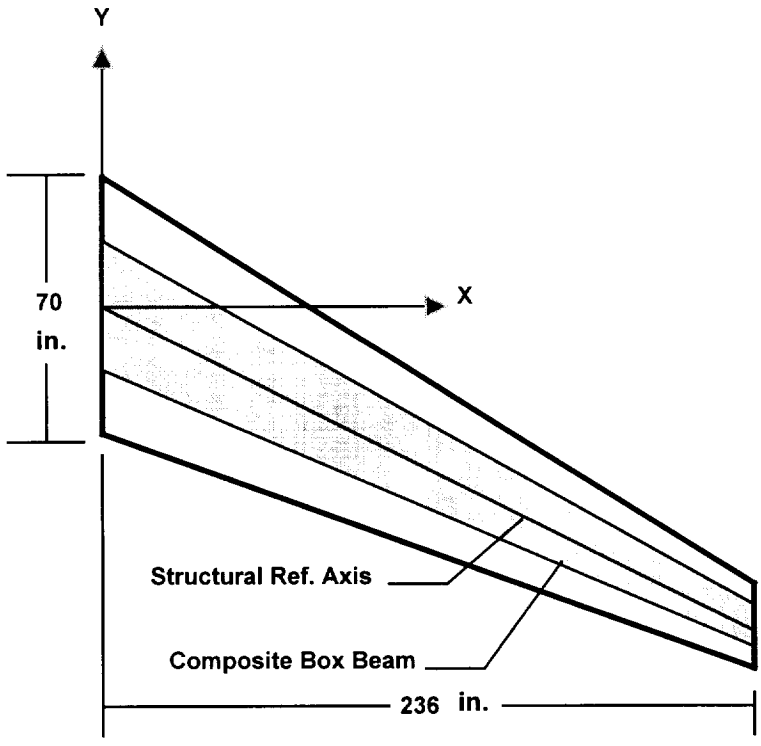

Figure 29. Wing geometry for MDO of composite wings

The box beam walls are assumed to be made of eight unidirectional composite laminates (each consisting of several plies of identical orientation), stacked symmetrically. It is assumed that the laminates in all four walls have the same thickness and that the thicknesses do not vary spanwise or chordwise. The top and the bottom walls have the same ply angles, as is the case for the two side walls. The ply angles and laminate thicknesses are allowed to vary, thus resulting in 12 design variables. The ply angles are allowed to vary between -90° and +90° and the laminate thicknesses vary between 0.006 inch and 0.048 inch during optimization. A reference configuration with conventional ply orientations of $(0°/90°/+45°/-45°)_S$ for each wall and uniform laminate thickness of 0.024 inch is used as the initial design.

The structural analysis of the box beam is performed with 10 elements spanwise and a single element chordwise. The first six normal modes of vibration are used in the subsequent analysis. The mode shapes are normalized such that the generalized masses are unity. The generalized aerodynamic forces (GAF) are computed at M=0.85 for 20 values of the reduced frequency between 0 and 1. The wing is divided into 48 panels. Rational function approximation of the GAF's is performed using four denominator coefficients. These coefficients are selected to be 0.2, 0.4, 0.6 and 0.8 which produce a very good fit. Convergence is reached in 10 cycles during which the objective function and the constraints are evaluated 208 times. The total time taken is 2 hr. 50 min. on Sun Ultra 1 workstation. Results obtained using the optimization procedure are presented in Table 6 and in Figure 30.

Table 6. Optimization results for MDO of composite wings

	Reference	Optimum
Stacking Sequence		
top /bottom walls	$(0°/90°/+45°/-45°)_S$	$(-8°/70°/28°/-13°)_S$

side walls	$(0°/90°/+45°/-45°)_S$	$(15°/48°/-5°/-24°)_S$
Laminate thickness (all walls, in.)	$(0.024/0.024/0.024/0.024)_S$	$(0.019/0.023/0.024/0.023)_S$
Wall thickness (in.)	0.192	0.178
Natural frequency (first six modes, Hz)	1.34, 5.55, 15.20, 22.63, 31.94, 37.94	1.58, 6.45, 17.44, 22.30, 35.79, 37.51
Wing structural weight (lb)	129.2	119.1
Flutter dynamic pressure (psi)	3.0	3.7
Tsai-Wu failure criteria	1.32	0.89

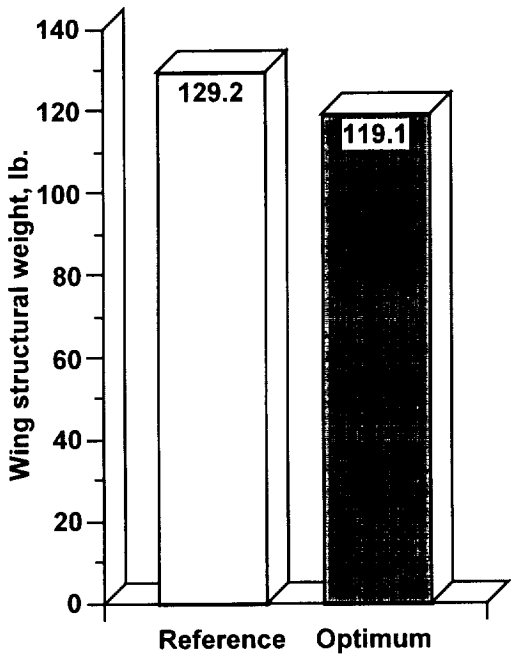

(a)

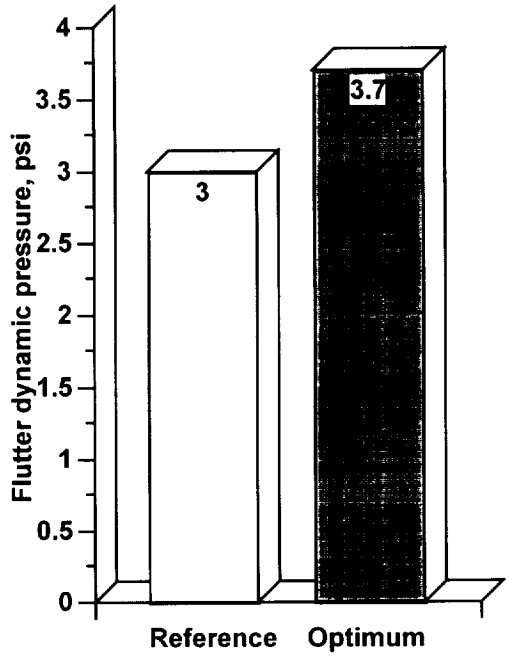

(b)

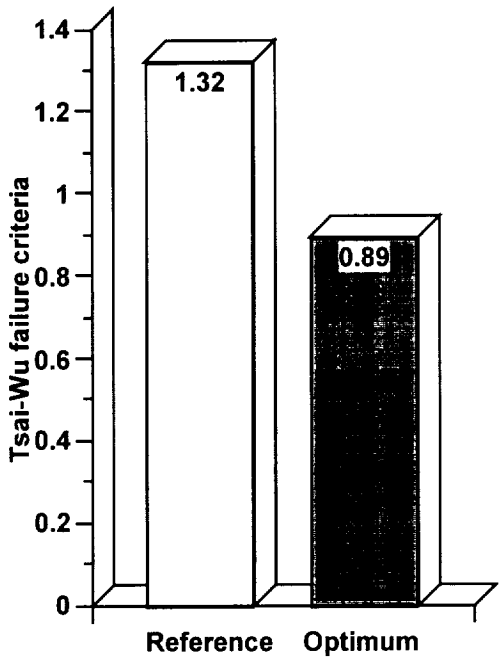

(c)

Figure 30. Optimization results for MDO of composite wings

The structural weight of the wing reduces by eight percent from 129.2 lb. to 119.1 lb. (Figure 30(a)), whereas the flutter dynamic pressure increases by 23 percent from 3.0 psi to 3.7 psi (Figure 30(b)). Also, from Table 6 and Figure 30(c), it is observed that the Tsai-Wu stress criterion is strongly violated in the reference design (F_c=1.32). Through optimization of the stacking sequence, even a lower wall thickness (resulting in reduced weight) satisfies the stress constraint (F_c=0.89). The ply angles for the optimized wing are $(-8°/70°/28°/-13°)_S$ in the top and bottom walls and $(15°/48°/-5°/-24)_S°$ in the side walls. It should be noted that the buckling constraits are not imposed in this optimization. The laminate thicknesses remain almost unchanged, except for the surface laminates in each wall. It is to be noted that in a practical design, standard ply angles and thickness are used. Therefore, the nearest values available must be used.

Study of the mode shapes (Figures 31-34) indicates similarity between reference and optimum designs. Modes 1, 2, 3 and 5 are bending modes and modes 4 and 6 are pitching modes. There is very little coupling between the two types of modes. However, the natural frequencies (Table 6) indicate an important change from reference to optimum wing. The frequencies for the bending modes increase by about 15 percent, whereas those for the pitching modes decrease slightly. As discussed later, it is the bending modes that exhibit particular flutter characteristics in this wing.

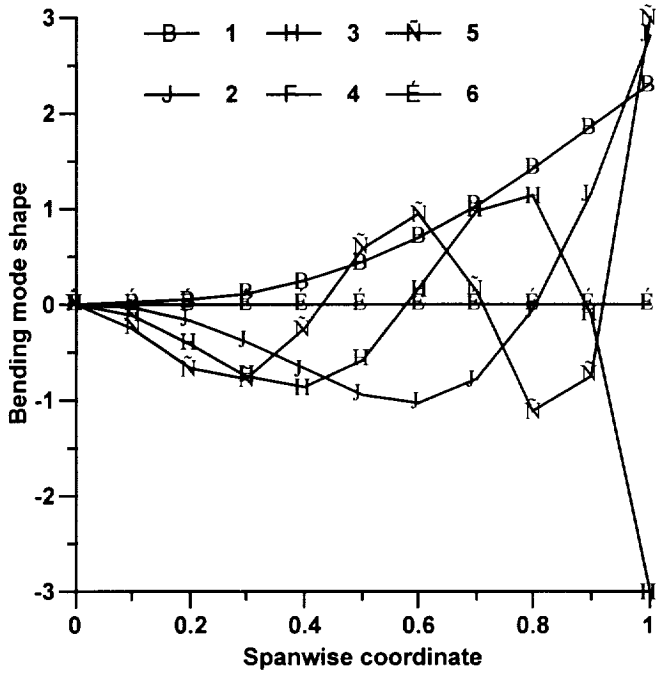

Figure 31. Bending mode shape for reference composite wing

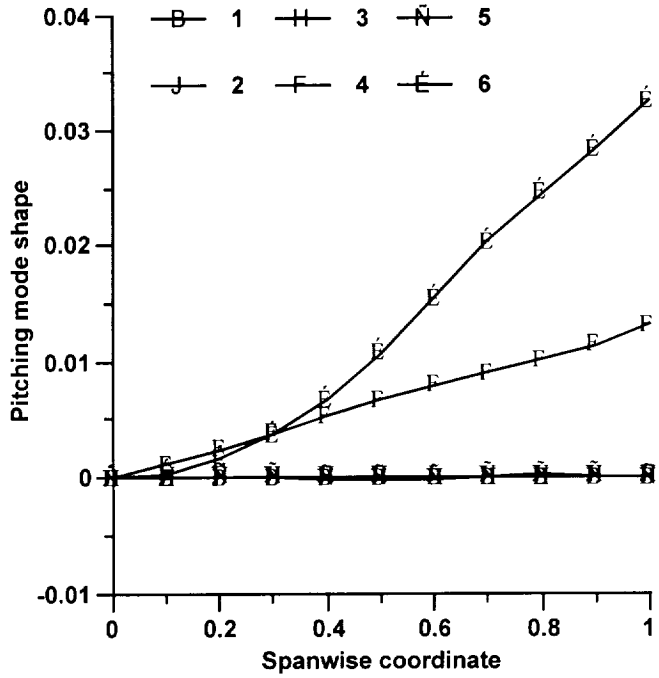

Figure 32. Pitching mode shape for reference composite wing

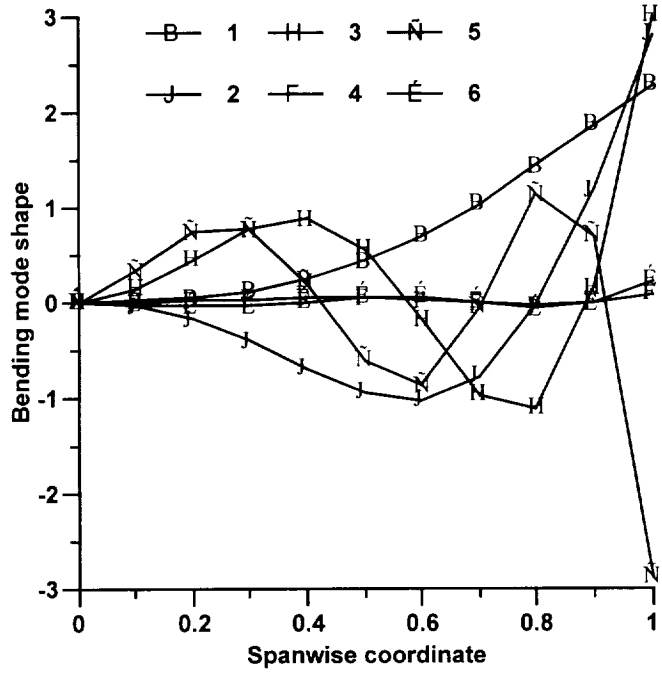

Figure 33. Bending mode shape for optimized composite wing

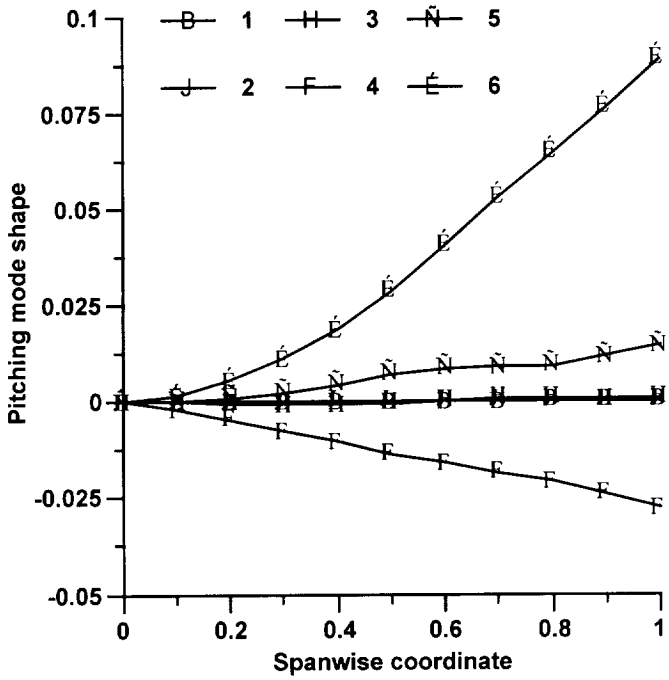

Figure 34. Pitching mode shape for optimized composite wing

Flutter is often caused when the frequencies of any two modes coalesce and the damping of either of the modes goes to zero. For divergence, the frequency also drops to zero along with the damping. Figures 35-40 present root loci and frequency and damping history for the reference and the optimized wings. In both cases, frequencies of modes 1 and 2 coalesce and the damping of mode 1 becomes unstable. The optimized wing has larger modal damping and somewhat wider separation between these two modes, leading to higher flutter dynamic pressure.

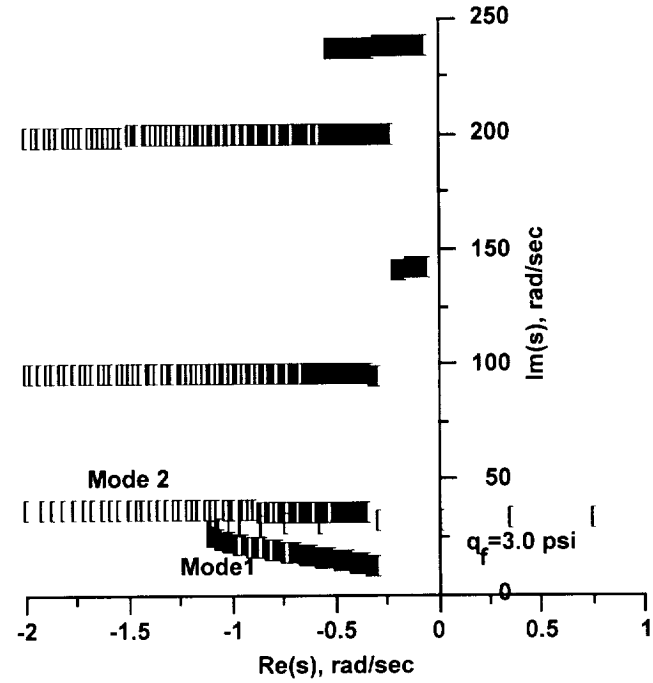

Figure 35. Dynamic pressure root locus for reference composite wing

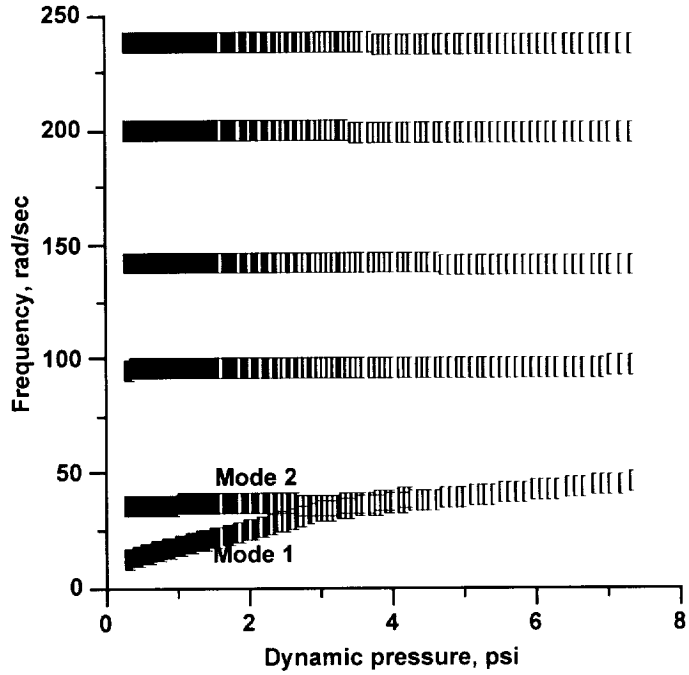

Figure 36. Frequency vs. dynamic pressure for reference composite wing

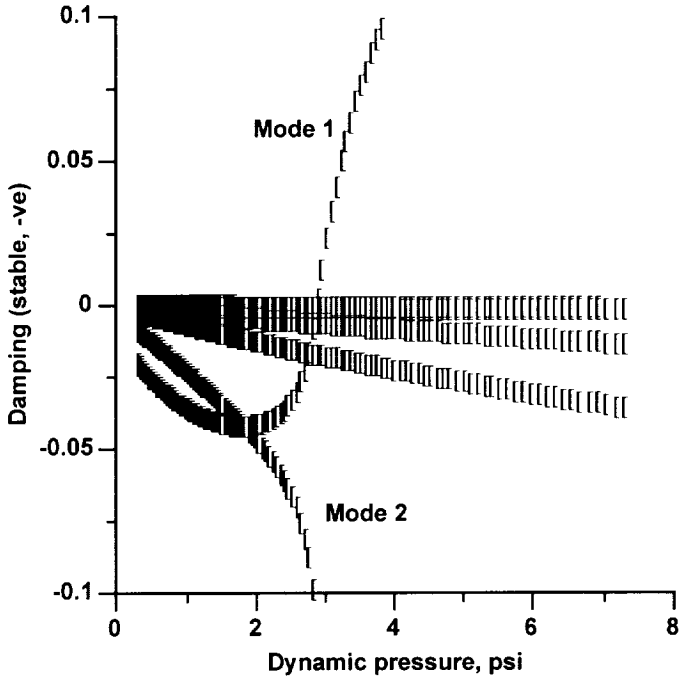

Figure 37. Damping vs. dynamic pressure for reference composite wing

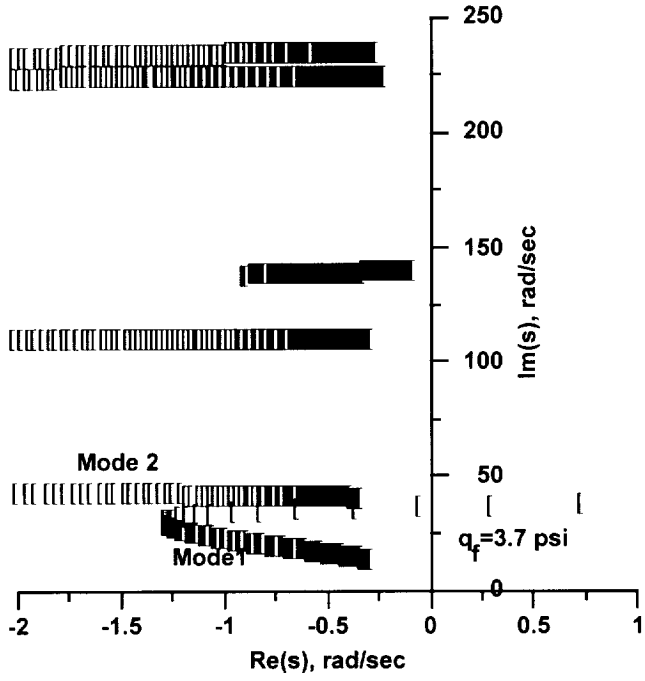

Figure 38. Dynamic pressure root locus for optimized composite wing

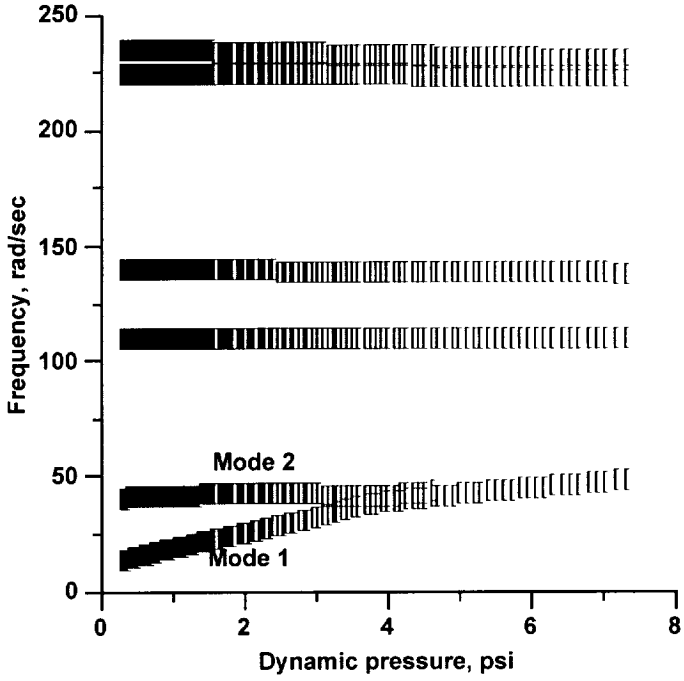

Figure 39. Frequency vs. dynamic pressure for optimized composite wing

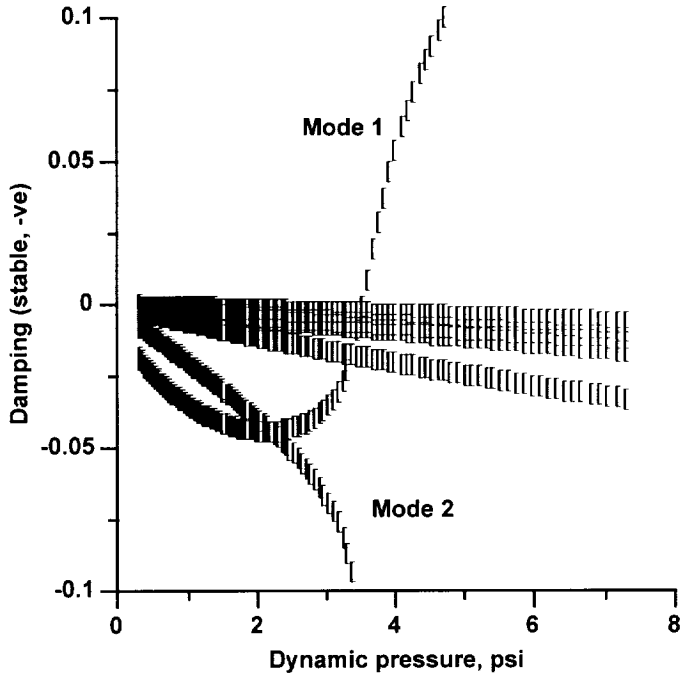

Figure 40. Damping history for optimized composite wing

4.5. MDO of Smart Composite Wings

The developed MDO procedure is applied to the design of a smart composite wing, with PZT actuators / sensors bonded to top and bottom surfaces of the box beam. The wing configuration is similar to a long range high speed business jet. The dimensions are scaled down to reduce the number of finite elements and aerodynamic panels. The optimization problem now is associated with multiple objective functions and constraints. All design variables are treated as continuous variables.

4.5.1 Optimization Problem

The objective is to minimize the structural weight of the wing while maximizing the aerodynamic efficiency (lift-to-drag ratio). Wing sweep, wall thickness of the box beam, ply orientations and the thickness of PZT actuators / sensors are design variables. The problem is formulated as a minimization problem and the two objective functions are as follows.

$$\begin{aligned} \text{Minimize:} \quad & f_1 = W \\ & f_2 = D/L \end{aligned} \tag{71}$$

where W is the weight of the box beam (including actuators), D is the drag and L is the lift. The cruise Mach number and altitude are assumed to be 0.90 and 30000 ft, respectively. It is required that the aircraft does not encounter flutter/divergence anywhere within the flight envelope. Therefore, a constraint is imposed on the flutter dynamic pressure (q_f) which is stated as follows.

$$g_1 = 1 - \frac{q_f}{8.0} \leq 0 \tag{72}$$

This constraint implies that the flutter dynamic pressure must not be less than 8.0 psi (M=0.9, SL). The wing strength constraint is based on a 3g maneuver at the cruise Mach number and altitude. The use of wing loading, suitable for this class of aircraft (70 lb./sq. ft.), and the selected wing area, the ultimate load for design (ultimate load factor = 4.5) is determined. The spanwise load distribution is obtained from the panel code [71] described earlier. A strength constraint is imposed on the ply stresses at the root section where material failure is most likely to occur. The Tsai-Wu failure criterion (discussed earlier in section 4.3) is used and this constraint is stated as follows.

$$g_2 = F_c - 1 \leq 0 \tag{73}$$

The box beam walls are assumed to be made of eight unidirectional Graphite-Epoxy (Table 1) composite laminates (each consisting of several plies of identical orientation), stacked symmetrically. In an effort to reduce the computational expense, the following assumptions are made about the ply orientations. The top and the bottom walls are assumed to have identical ply orientations. The ply angles for the two side walls are also maintained identical (but may be different from the top/bottom walls). Therefore, eight design variables are used to completely describe the stacking sequence.

Top/bottom walls: $$(\theta_1/\theta_2/\theta_3/\theta_4)_s = (\phi_1/\phi_2/\phi_3/\phi_4)_s \tag{74}$$

Side walls: $$(\theta_1/\theta_2/\theta_3/\theta_4)_s = (\phi_5/\phi_6/\phi_7/\phi_8)_s \tag{75}$$

where the ply angles are allowed to vary between -90 deg. and +90 deg. It is assumed that the laminates thicknesses do not vary spanwise or chordwise and all four walls have the same thickness. The laminate thickness design variables are defined as follows.

$$(t_1/t_2/t_3/t_4)_s = (\phi_9/\phi_{10}/\phi_{11}/\phi_{12})_s \tag{76}$$

where the thickness of each laminate can vary between 0.01 in. and 0.03 in. The mid-chord sweep of the wing is defined as a design variable with the upper and lower bounds specified as follows.

$$\Lambda_{c/2} = \phi_{13} \qquad 25^{o} \le \phi_{13} \le 40^{o} \tag{77}$$

It is assumed that a pair of actuators / sensors are surface bonded to the top and the bottom of the box beam (covering the area of the first element along the wing root). The thickness of the actuators / sensors (t_p), assumed to be identical, is used as a design variable.

$$t_p = \phi_{14} \qquad 0.005^{"} \le \phi_{14} \le 0.015^{"} \tag{78}$$

4.5.2 Results and Discussions

The reference wing has root chord of 50 in., semi-span of 160 in., aspect ratio of 9.5, taper ratio of 0.35, thickness-to-chord ratio of 11 percent and mid-chord sweep of 30 degree. The wing sweep is varied during the optimization and all other parameters are held constant. The length of the box beam and the side wall areas change as wing sweep is varied. The width of the box beam is assumed equal to half the wing chord. A reference configuration with conventional ply orientations of $(0°/90°/+45°/-45°)_S$ for each wall and uniform laminate thickness of 0.02 in. (wall thickness = 0.16 in.) is used as the initial design. The structural characteristics of the PZT actuators / sensors (G-1195) [48], which affect mass and stiffness of the wing, as well as the induced strain are included in the analysis. The applied voltage is such that the maximum electric field for PZT materials (15000 volts/in.) is not exceeded.

The structural analysis of the box beam is performed with 10 elements spanwise and a single element chordwise. The first six normal modes of vibration are used for the

subsequent analysis. The mode shapes are normalized such that the generalized masses are unity. The generalized aerodynamic forces (GAF) are computed at M=0.90 for 20 values of the reduced frequency between 0 and 1. The wing is divided into 48 panels. Rational function approximation of the GAF's is performed using four denominator coefficients (equation (49)). These coefficients are selected to be 0.2, 0.4, 0.6 and 0.8 which produce a very good fit.

Table 7. Optimization results for MDO of smart composite wing

	Reference	Optimum
Stacking Sequence		
top /bottom walls	$(0°/90°/+45°/-45°)_S$	$(-1°/90°/32°/-44°)_S$
side walls	$(0°/90°/+45°/-45°)_S$	$(2°/90°/44°/-36°)_S$
Laminate thickness (all walls, in.)	$(0.02/0.02/0.02/0.02)_S$	$(0.025/0.011/0.013/0.012)_S$
Wall thickness (in.)	0.160	0.122
Mid-chord sweep (deg.)	30	39
PZT actuator thickness (in.)	0.005	0.011
Applied voltage (volt)	75	165
Natural frequency (first six modes, Hz)	1.64, 7.56, 21.84, 33.29, 46.35, 52.37	1.46, 6.53, 18.43, 27.27, 38.09, 44.02
Wing structural weight (lb)	58.62	47.28
Lift-to-drag ratio	11.24	14.71
Flutter dynamic pressure (psi)	6.9	8.0
Tsai-Wu failure criteria	0.79	0.71

The developed MDO procedure is computationally efficient as each run takes approximately one minute on Sun Ultra 1 workstation for the numerical example presented. Convergence is reached in 12 cycles during which the objective function and the constraints are evaluated 259 times. Figure 41 shows the reference and the optimum wing geometries. The optimization results are summarized in Table 7 and Figure 42. The structural weight of the wing (box beam with actuator / sensor) reduces by 19 percent (from 58.62 lb. to 47.28 lb.) and the lift-to-drag ratio increases by 31 percent (from 11.24 to 14.71). The flutter dynamic pressure for the optimized wing increases from 6.9 psi to 8.0 psi and, therefore, satisfies the design constraint. The Tsai-Wu strenght constraint is well satisfied by both the reference and the optimized designs.

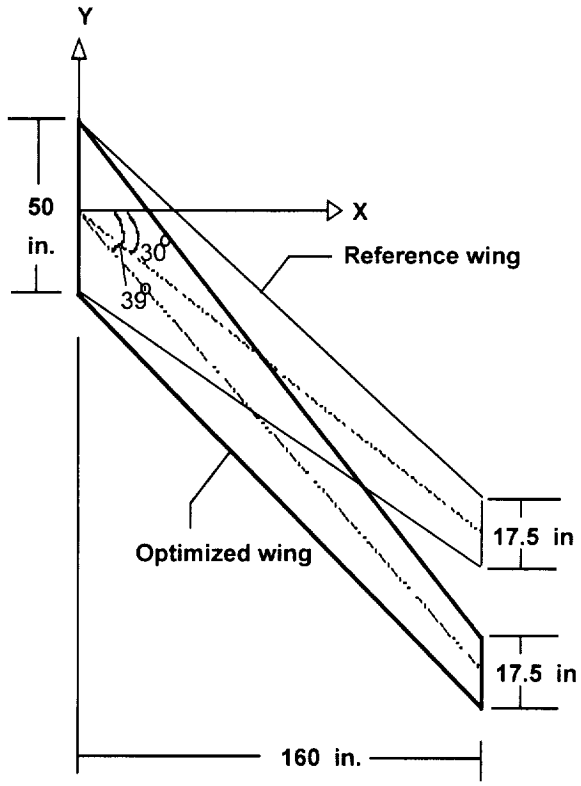

Figure 41. Reference and optimized geometry for smart composite wing

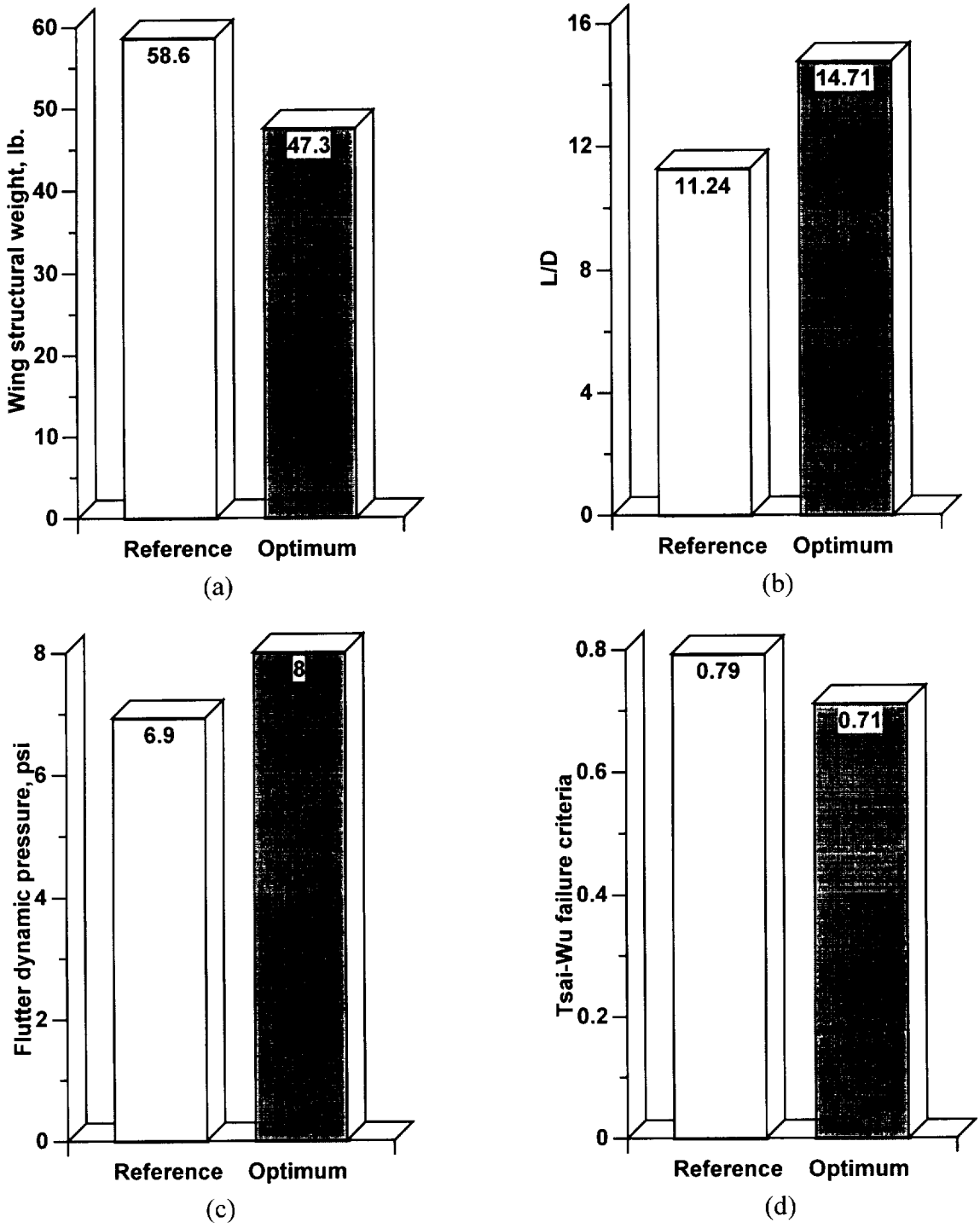

Figure 42. Optimization results for MDO of smart composite wing

The reduction in the weight is achieved through lower wall thickness, which reduces from 0.160 in. to 0.122 in. Even with lower thickness of the box beam walls, due to the optimized ply orientations, laminate thicknesses and (increased) actuator thickness, the flutter dynamic pressure increases to the required value in the optimum configuration. These design variables actually contribute more to the flutter dynamic pressure than is apparent from the final results. The higher sweep angle of the optimized wing (39 deg.) has a detrimental effect on flutter, but it reduces the compressibility drag. Though the higher wing sweep produces larger induced drag, the total drag reduces to enhance aerodynamic efficiency of the wing substantially. Study of the ply orientations shows relatively small changes in the positive angle plies (+45 deg. to +32 deg.) for the top/bottom walls and negative angle plies (-45 deg. to -36 deg.) for the side walls. The other ply angles remain nearly unchanged. However, the changes in the laminate thicknesses are significant. The thickness of the zero degree laminate increases to 0.025 in., whereas that for other laminates decreases to about 0.012 in. As shown later, flutter is caused by the first two bending modes which are stiffened due to increased thickness of the zero degree laminates. It is to be noted that in a practical design, standard ply angles and thickness are used. Therefore, the nearest values available must be used. Through optimization of the ply angles and laminate (ply) thicknesses, even a lower wall thickness (resulting in reduced weight) reduces the maximum stress in the laminates.

Study of the mode shapes (not shown) indicates similarity between reference and optimum designs. Modes 1, 2, 3 and 5 represent bending modes and modes 4 and 6 represent pitching modes. The natural frequencies reduce from reference to optimum design, largely due to the increased wing sweep. The eigenvalues of the characteristic equation vary with dynamic pressure. A root locus constructed by varying the altitude for a given Mach number yields flutter dynamic pressure when one of the real roots becomes zero and the imaginary root is non-zero. The variations in frequency and modal damping

with dynamic pressure provide an insight into the onset of flutter/divergence. Flutter is often caused when the frequencies of any two modes coalesce and the damping of either of these modes goes to zero. For divergence, the frequency also drops to zero along with the damping. Figures 43-48 present root loci and frequency and damping histories for reference and optimized wings. In both cases, frequencies of modes 1 and 2 coalesce and the damping of mode 1 becomes unstable. The optimized wing has larger modal damping leading to higher flutter dynamic pressure, although the frequency separation is smaller between these two modes.

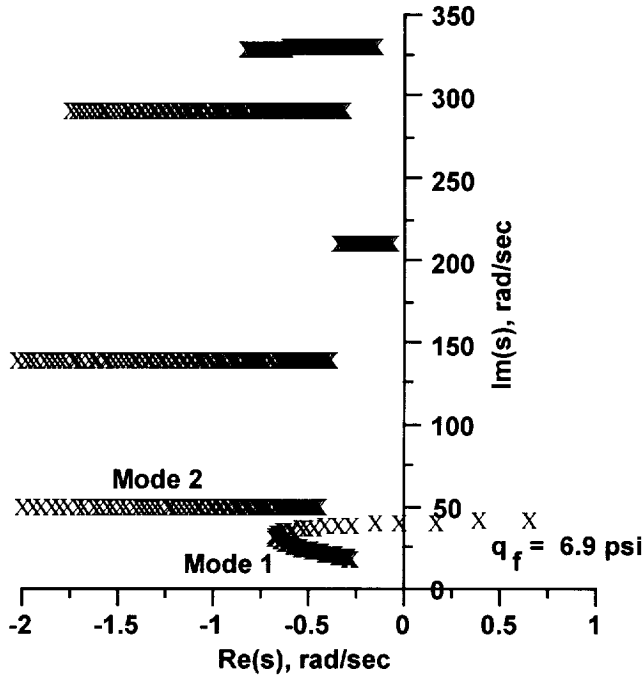

Figure 43. Root locus for smart composite wing (reference design)

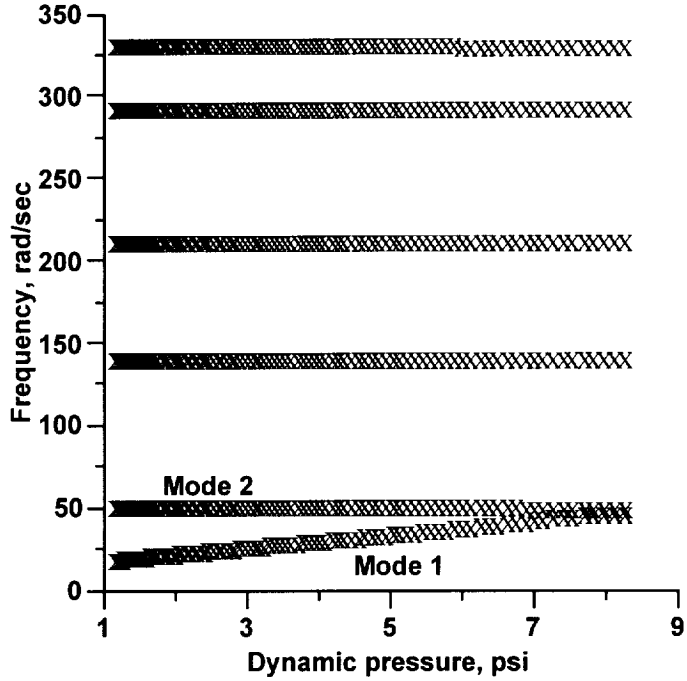

Figure 44. Frequency history for smart composite wing (reference design)

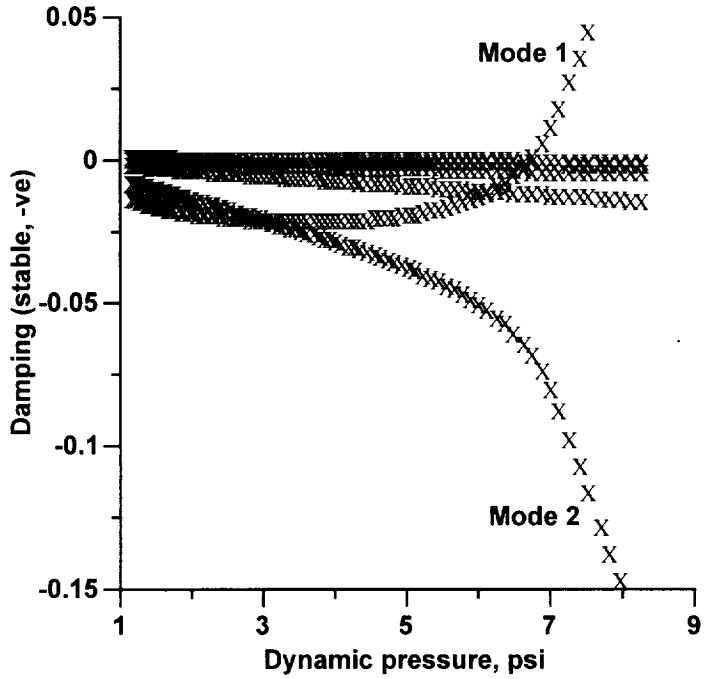

Figure 45. Damping history for smart composite wing (reference design)

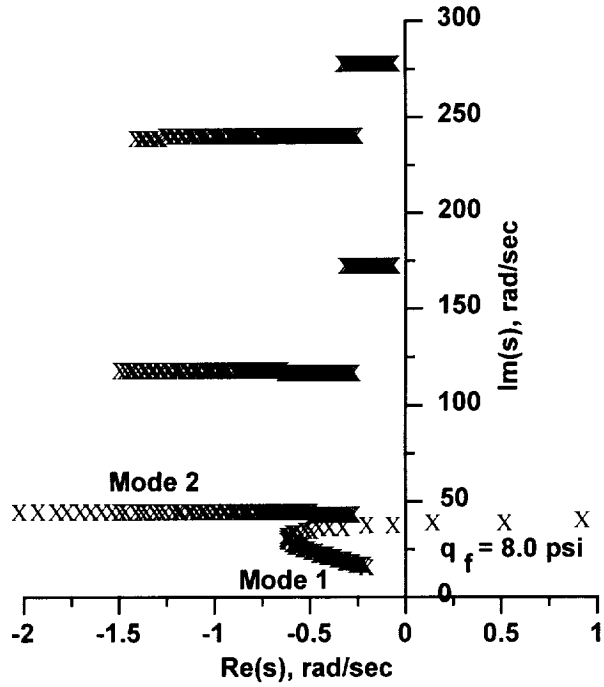

Figure 46. Root locus for smart composite wing (optimum design)

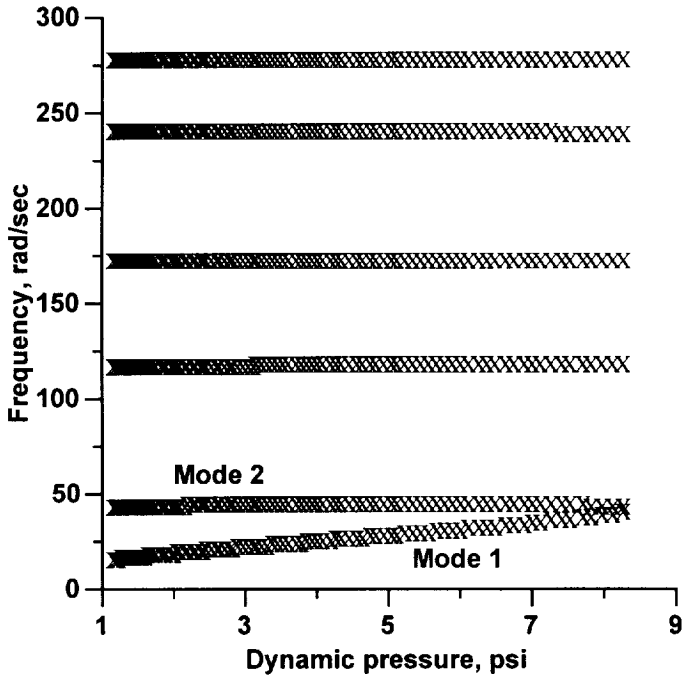

Figure 47. Frequency history for smart composite wing (optimum design)

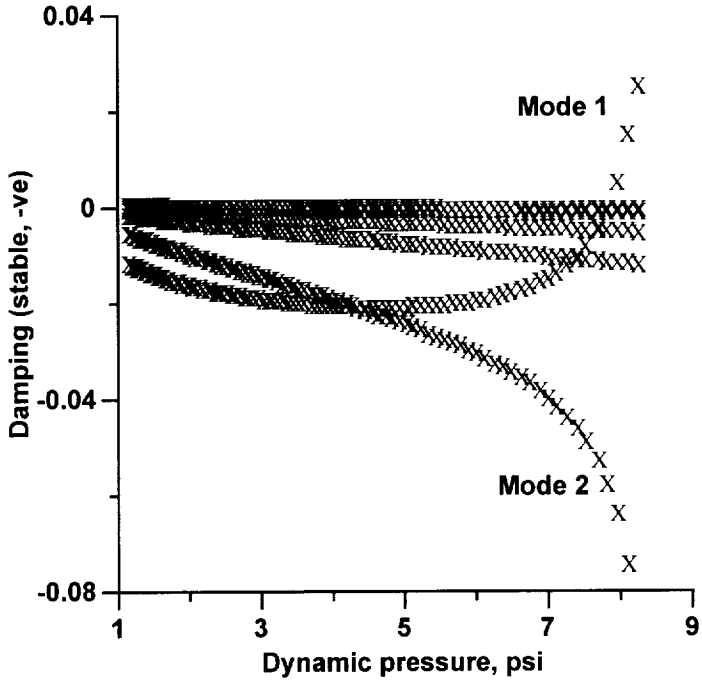

Figure 48. Damping history for smart composite wing (optimum design)

5. MDO of Turbomachinery Blades

Aerodynamic and heat transfer design objectives are integrated along with various mechanical constraints on the blade geometry for the multidisciplinary design optimization of turbine blade profile. The K-S function method is used for multiobjective optimization. The methods used for blade geometric modeling and aerodynamic and heat transfer analyses are briefly described. A numerical example is presented showing the benefits of application of the developed MDO procedure.

5.1 Blade Modeling

Bezier curves have properties that make them ideal choice to represent complex shapes [65]. These curves can be explicitly expressed through the use of Bernstein polynomials. The representation of airfoil geometry by Bezier-Bernstein polynomials has been successfully used for shape optimization [61, 64]. A two-dimensional boundary is defined by Bezier-Bernstein curve of degree n as follows.

$$b^n(t) = \sum_{j=o}^{n} b_j B_j^n(t) \tag{79}$$

The vector of Bezier control points b_j, consisting (n+1) values of x and y coordinates of the control points, are varied to generate different Bezier curves. The n-th degree Bernstein polynomials are given by

$$B_j^n(t) = \frac{n!}{j!(n-j)!} t^j (1-t)^{n-j} \tag{80}$$

where the values of interpolation points t lie between 0 and 1.

This approach can accurately represent a complex shape with relatively small number of geometric control points (Figure 49), which are used as design variables. Hence, a reduced number of design variables may be adopted in the design optimization procedure. The Bezier curves also possess high order of continuity and the end points pass through the first and last control points.

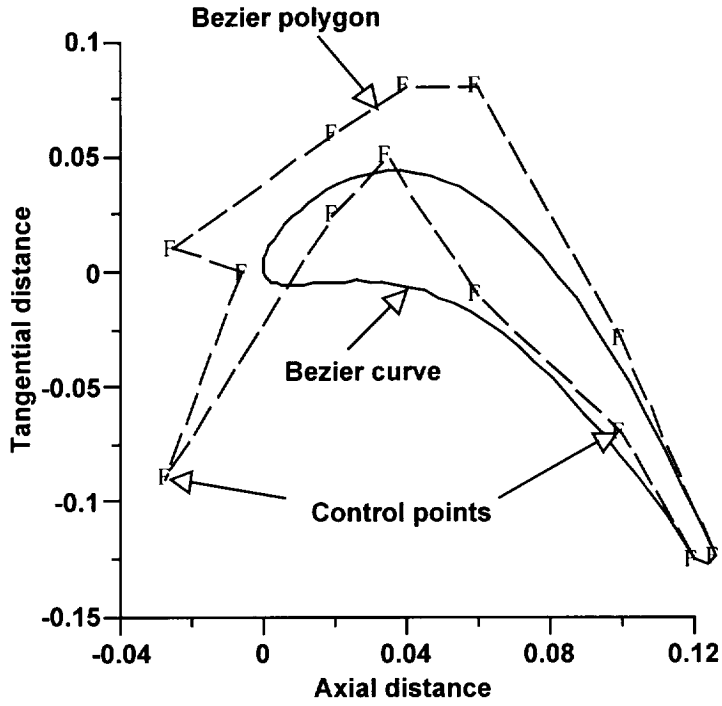

Figure 49. Bezier-Bernstein representation of turbine blade geometry

5.2 Analysis

5.2.1 Aerodynamic Analysis

Since the results of the optimization procedure depend on the accuracy of the analysis techniques used, it is important to integrate reliable analyses within the optimization loop. The complex flow environment in turbomachinery components can be best described by three-dimensional analysis. However, the coupling of such codes within a closed loop

optimization procedure can be computationally very expensive. In the current research, the aerodynamic analysis is performed using the RVCQ3D (Rotor Viscous Code Quasi-3-D) code [66-67]. It is a rapid code capable of analyzing blade-to-blade viscous flows in turbomachines. The analysis is based on the thin shear layer approximation of the Navier-Stokes equations. The flow equations are mapped to a body-fitted coordinate system and a periodic C-shaped grid is used. Second-order finite differences and an explicit multistage Runge-Kutta scheme are implemented for time marching flow solution. For turbulent flow calculations, the Baldwin-Lomax turbulence model is available. The method includes the quasi-three-dimensional effects of rotation, radius change and stream surface thickness variation. The code has been validated for several test cases and has been used for many applications [85].

Grid generation is accomplished using the GRAPE (GRids about Airfoils using Poisson's Equation) code [68-69]. This code performs grid generation by solving Poisson equations with arbitrarily specified inner and outer boundary points. The desired grid spacing and intersection angles at the boundaries are obtained through proper choice of the forcing terms in the Poisson equations.

5.2.2 Heat Transfer Analysis

The temperature distribution in the blade interior [86] is obtained by solving the following equation of two-dimensional heat conduction.

$$\frac{\partial}{\partial x}\left(k\frac{\partial T}{\partial x}\right)+\frac{\partial}{\partial y}\left(k\frac{\partial T}{\partial y}\right)=0 \tag{81}$$

In the above equation, T is the local blade temperature and k is the thermal conductivity of the blade material. The finite element method is used to solve the boundary value

problem. The computational domain is discretized using linear triangular elements. The mesh is regenerated as the blade geometry changes during optimization. The temperature obtained from the RVCQ3D solution is used to specify the Dirichlet type nodal boundary condition. Using the Galerkin approach, the boundary value problem is reduced to the following system of linear equations

$$KT = f \tag{82}$$

which is solved for the unknown nodal temperatures T. The coefficient matrix K and the vector f are evaluated using the finite element formulation.

5.3 Optimization Problem

The developed multidisciplinary optimization procedure [87] has been applied to the design of a subsonic turbine blade. The objectives are to minimize the total pressure loss and maximize the kinetic energy efficiency [85] for the blade-to-blade flow by changing the blade profile. The total pressure loss is defined as

$$\omega = 1 - P_{02} / P_{01} \tag{83}$$

where subscripts 1 and 2 refer to conditions at inlet and exit, respectively. The kinetic energy efficiency is defined by the following equation.

$$\eta_{KE} = V_2^2 / V_{2\,ideal}^2 \tag{84}$$

where V_2 is the relative flow velocity at exit and

$$V_{2\,ideal}^2 = 2C_p T_{01}\left(1 - \left(\frac{P_2}{P_{01}}\right)^{\frac{\gamma-1}{\gamma}}\right) \tag{85}$$

Since no coolant hole or film cooling is considered in the present design, minimization of average and maximum blade temperatures was not included as an objective. The blade temperature was treated as a constraint. The maximum and average blade temperatures are constrained not to exceed that of the reference blade. Blade chord, trailing edge thickness and stagger angle are kept constant during the optimization. Accordingly, the two control points at the trailing edge and the leading edge control point are not varied. The tangential coordinates of the remaining ten control points are treated as design variables, while their axial coordinates remain fixed. The area of the blade section is constrained to lie within ten percent of the reference blade area to assure structural integrity and to prevent large weight increase.

5.4 Results and Discussions

The reference blade (Figure 50) represents a standard section used for turbine design. The blade has a finite trailing edge thickness and its chord length and stagger angle are 0.122 ft and 45 degrees, respectively. The annular cascade is assumed to have 36 blades rotating at 2000 rpm. The following flow parameters are specified: Reynolds number = $6x10^6$ per ft, inlet Mach number (absolute) = 0.21, inlet flow angle (absolute) = 0°, inlet total temperature = 1500 K, exit static pressure ratio = 0.70, and relative flow angle at trailing edge = -65 degrees. The external flow field around the blade is discretized using the GRAPE code with 97 points around the blade and 31 points normal to the blade. The flow calculations are done with RVCQ3D utilizing four stage Runge-Kutta scheme. The blade interior is discretized with approximately 2100 elements for computing the temperature distribution.

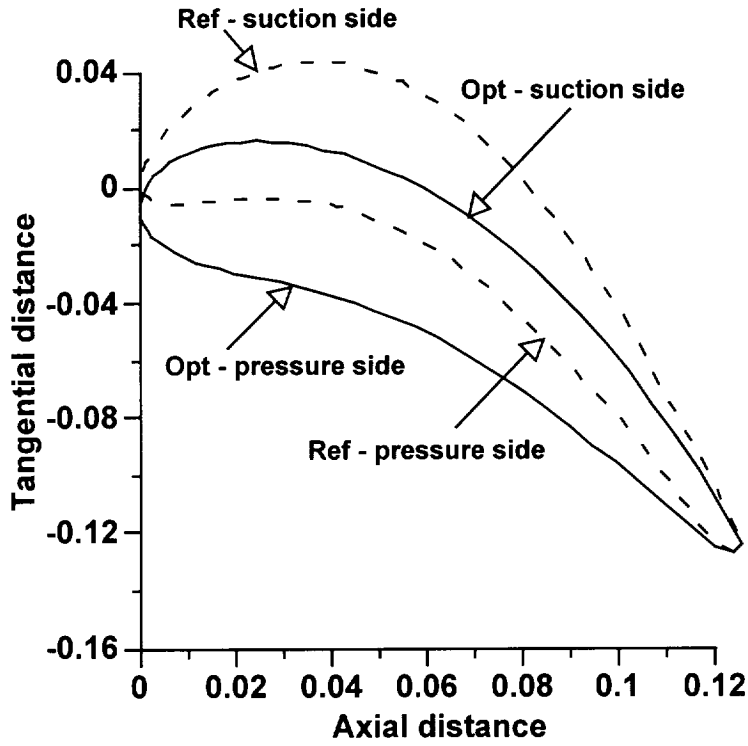

Figure 50. Reference and optimum blade geometry

The optimization results are presented in Figures 50-57. The reference and optimized blade profiles are shown in Figure 50. Significant changes to the suction and the pressure surfaces are observed, though the airfoil area remains unchanged. The optimized blade profile represents the most efficient aerodynamic shape at the flow conditions specified. In a practical application of the developed MDO procedure, additional constraints may be imposed on the blade geometry from other design considerations. The surface Mach number and static pressure distributions are shown in Figures 51 and 52, respectively. On the pressure side, the small adverse pressure gradient and flow deceleration in the leading edge region are eliminated, resulting in a smoother velocity profile. The pressure gradient on the suction side is more favorable and hence the flow accelerates to higher Mach number near the leading edge. The pressure and the Mach number variations

remain non-smooth at the blade trailing edge, because its geometry was held fixed during the optimization

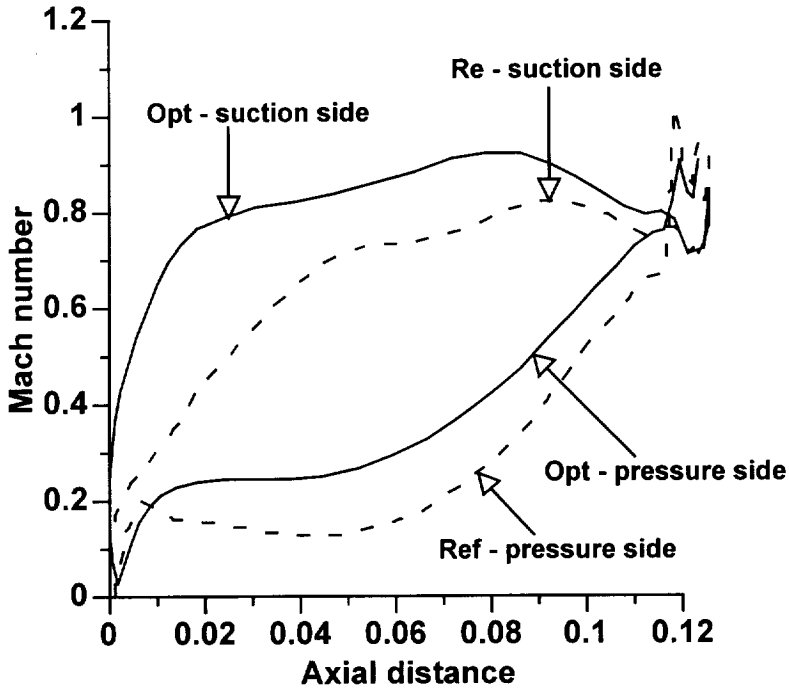

Figure 51. Mach number distribution

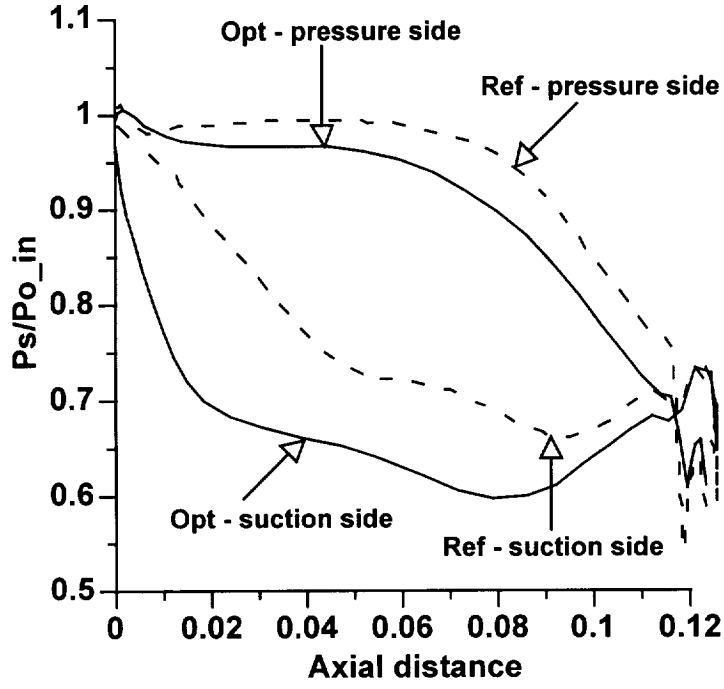

Figure 52. Static pressure distribution

The total pressure ratios P_{02} / P_{01} are plotted in Figure 53 for reference and optimized blades. The total pressure loss is reduced from 2.9 percent to 1.1 percent. It should be noted that even a small reduction in the turbine loss has a significant effect on the overall performance of the engine. There is a substantial increase (5.5 percent) in the kinetic energy efficiency due to optimization (Figure 54). The temperature distribution in the blade interior are presented in Figures 55 and 56 for reference and optimized profiles, respectively. The blade temperature constraint is satisfied as shown in Figure 57, where the temperature of the optimized blade is normalized with respect to that of the reference blade.

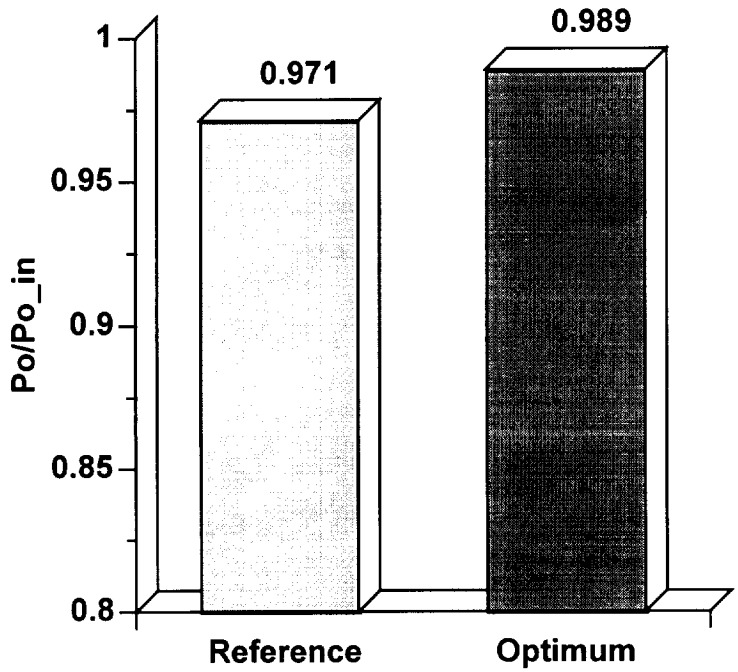

Figure 53. Exit total pressure ratio

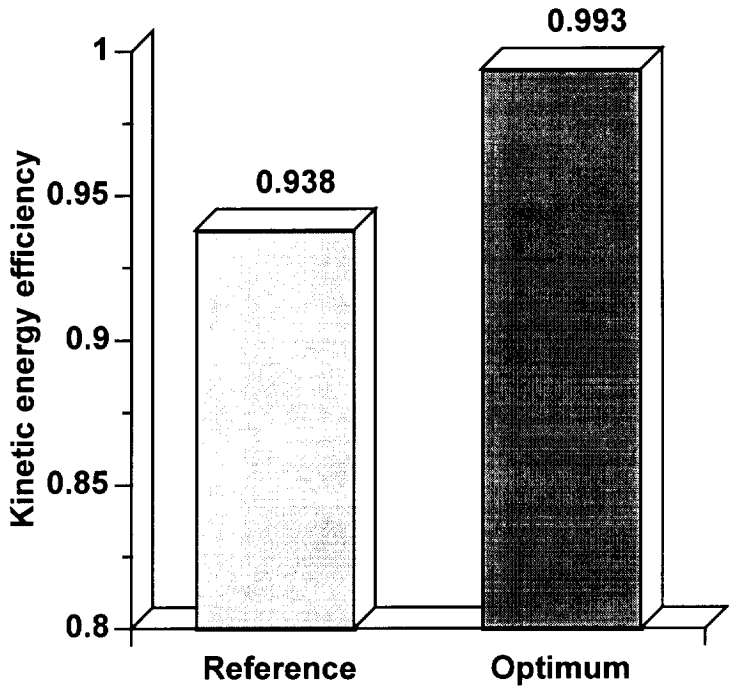

Figure 54. Exit kinetic energy efficiency

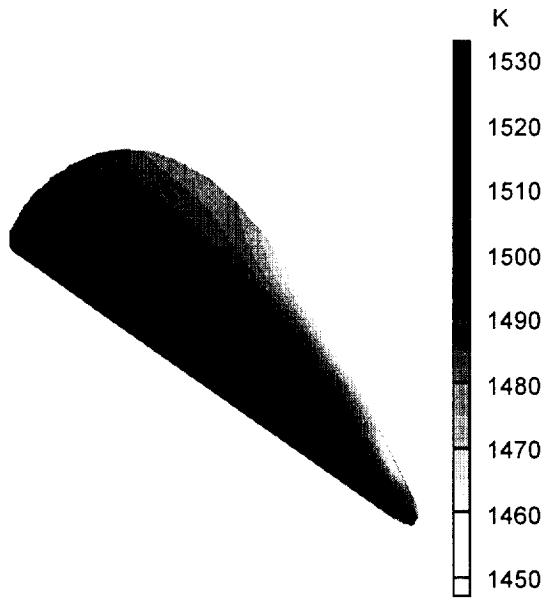

Figure 55. Reference blade temperature distribution

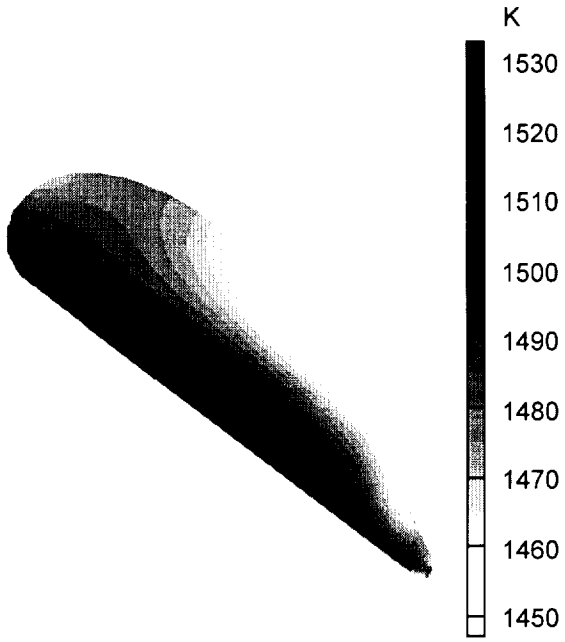

Figure 56. Optimum blade temperature distribution

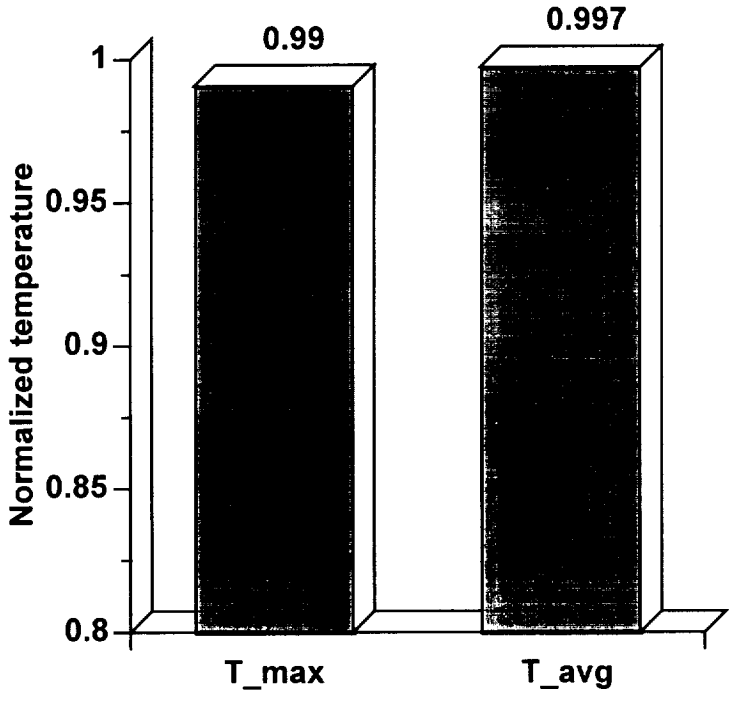

Figure 57. Maximum and average temperature (optimum blade)

6. Concluding Remarks

A new multidisciplinary design optimization procedure has been developed for the conceptual design of composite wings with surface bonded piezoelectric actuators / sensors. The analysis and optimization methods used are computationally efficient and sufficiently rigorous for using the developed MDO procedure for actual design applications. The optimization procedure for smart composite wing design involves the coupling of structural mechanics (including smart material), aeroelasticity and aerodynamics. The load carrying member of the wing is idealized and represented as a composite box beam. Each wall of the box beam is analyzed as a composite laminate using a refined higher-order displacement field to account for the variations in transverse shear stresses through the thickness. Detailed structural modeling issues associated with piezoelectric actuation of composite structures are included. This structural model is suitable for analyzing both thin- or thick-walled constructions. The governing equations of motion are solved using the finite element method to analyze practical wing geometries.

The wing steady and unsteady aerodynamic loads are obtained using a panel code based on the constant-pressure lifting surface method. This method utilizes the linearized aerodynamic potential theory for compressible flows. Two methods for flutter/divergence analysis have been implemented. The V-g method has been used to predict accurate flutter/divergence speed. The Laplace domain method of flutter prediction involves approximating generalized aerodynamic forces, but it produces root-loci of the system which give an insight into the physical phenomena leading to flutter/divergence.

In the gradient based optimization procedure, the Kreisselmeier-Steinhauser (K-S) function approach is used to efficiently integrate the objective functions and constraints into a single envelope function. The resulting unconstrained optimization problem is solved using the Broyden-Fletcher-Goldberg-Shanno algorithm. For optimization problems involving both continuous and discrete design variables, a procedure has been developed using the hybrid optimization technique. Based on the several numerical examples presented, the following important observations are made.

1. Flutter solution is obtained for an example wing using the present approach and the classical laminate theory (CLT), which neglects transverse shear stresses. The flutter speed using CLT is about 10 percent higher compared to that using the present approach. This significant difference in flutter prediction between the two theories can be a very critical issue since the flutter phenomenon is catastrophic in nature. The difference in the flutter speed is obviosly due to the presence of through-the-thickness transverse shear stresses which are ignored by CLT. This example establishes the significance of the refined higher-order displacement field on the aeroelastic stability of composite wings.

2. The effect of composite ply orientations on flutter/divergence dynamic pressure has been studied, using the Laplace domain method. It has been shown that the existence of various coupling modes, for different ply orientations, strongly influence the wing aeroelastic characteristics.

3. In the numerical example for the hybrid optimization technique, wing root chord and wall thickness are used as continuous design variables, whereas the ply orientations are treated as discrete variables. The wing weight is used as objective function which is minimized with constraints on flutter/divergence speed and

stresses at the wing root due to the specified air loads. The optimized design reduces the wing weight by 32 percent while satisfying the constraints. However, due to the use of simulated annealing within the optimization algorithm, a large number of function evaluations are required. This makes the procedure computationally expensive.

4. The developed MDO procedure with refined analysis methods and sophisticated (gradient bassed) optimization technique has been applied to the design of a composite wing. The wing configuration of a high speed business jet type airplane is selected for the optimization. The optimization converges in 10 cycles taking only 2 hr. 50 min. on Sun Ultra 1 workstation. The optimized design has significantly lower wing weight (eight percent) and higher flutter dynamic pressure (23 percent). The wing strength constraint, though severely violated in the initial design, is met by the optimized design.

5. The higher-order theory based composite box beam model has been extended to include piezoelectric actuators / sensors bonded to top and bottom surfaces. The optimization problem is formulated with the objective of simultaneously minimizing wing weight and maximizing its aerodynamic efficiency. Design variables include composite ply orientations, ply thicknesses, wing sweep, and piezoelectric actuator thickness. Constraints are placed on the flutter/divergence dynamic pressure and wing root stresses. The maximum electric field applied to the actuators is restricted by the coercive field of the PZT material. The developed MDO procedure is computationally efficient as each run takes approximately one minute on Sun Ultra 1 workstation for the numerical example presented. Convergence is reached in 12 cycles during which the objective function and the constraints were evaluated 259 times. The optimal design shows

physically meaningful results. The weight of the wing is reduced by 19 percent and the lift-to-drag ratio increases by 31 percent. The flutter dynamic pressure for the optimized wing increases from 6.9 psi to 8.0 psi and the Tsai-Wu strenght constraint is well satisfied. The wing sweep is increased to 39 degree for reduced compressibility drag (hence increased aerodynamic efficiency). The thickness of zero degree plies is substantially increased which enhances the damping of bending modes leading to higher flutter dynamic pressure. The larger thickness of the PZT actuators also helps increase flutter dynamic pressure.

The development of a new multidisciplinary optimization procedure for the design of turbine blades is presented. The procedure integrates aerodynamic and heat transfer design objectives along with mechanical constraints on blade geometry. Bezier-Bernstein representation of the blade profile leads to a relatively small set of design variables. Viscous blade-to-blade flow is calculated through thin shear layer approximation of the Navier-Stokes equation. A Poisson's equation based grid generator provides the grid for the flow solution. The maximum and average blade temperatures are obtained through a finite element analysis. Total pressure loss is minimized and the exit kinetic energy efficiency is maximized with constraints on blade temperatures and geometry. The K-S function approach is used to solve the multiobjective constrained nonlinear optimization problem. The results for the numerical example show significant improvements after optimization. The total pressure loss is reduced by 1.8 percent and there is 5.5 percent increase of the kinetic energy efficiency. The maximum and average blade temperatures for the optimum blade are lower than the reference case. Other design constraints such as airfoil area, chord, trailing edge thickness and stagger angle are satisfied.

7. References

1. Venkayya, V. B., "Introduction: Historical Perspective and Future Directions," *Structural Optimization: Status and Promise*, edited by M. P. Kamat, Vol. 150, *Progress in Astronautics and Aeronautics*, AIAA, Washington, D. C., 1993, pp. 1-10.

2. Ashley, H., "On Making Things the Best - Aeronautical Uses of Optimization," *Journal of Aircraft*, Vol. 19, No. 1, Jan. 1982, pp. 5-28.

3. Miura, H. and Neill, D. J., "Applications to Fixed-Wing Aircraft and Spacecraft," *Structural Optimization: Status and Promise*, edited by M. P. Kamat, Vol. 150, *Progress in Astronautics and Aeronautics*, AIAA, Washington, D. C., 1993, pp. 705-742.

4. Duysinx, P. and Fleury, C., "Optimization Software: View from Europe," *Structural Optimization: Status and Promise*, edited by M. P. Kamat, Vol. 150, *Progress in Astronautics and Aeronautics*, AIAA, Washington, D. C., 1993, pp. 807-850.

5. Johnson, E. H., "Tools for Structural Optimization," *Structural Optimization: Status and Promise*, edited by M. P. Kamat, Vol. 150, *Progress in Astronautics and Aeronautics*, AIAA, Washington, D. C., 1993, pp. 851-864.

6. Sobieszczanski-Sobieski, J. and Haftka, R. T., "Multidisciplinary Aerospace Design Optimization: Survey of Recent Developments," AIAA 96-0711, *Proc.* 34th Aerospace Sciences Meeting and Exhibit, Jan. 1996, Reno, Nevada.

7. Kroo, I., "MDO Applications in Preliminary Design: Status and Directions," AIAA 97-1408, *Proc.*, 38th AIAA/ASME/ASCE/AHS/ASC Strctures, Structural Dynamics, and Materials Conference, April 7-10, 1997, Kissimmee, Florida.

8. Mason, W., "Analytic Models for Technology Integration in Aircraft Design," AIAA Paper 90-3262, Sept. 1990.

9. Wakayama, S. and Kroo, I., "Subsonic Wing Planform Design Using Multidisciplinary Optimization," *Journal of Aircraft*, Vol. 32, No. 4, 1995, pp. 746-753.

10. Barthelemy, J. -F. M., Wrenn, G. A., Dovi, A. R. and Coen, P. G., "Integrating Aerodynamics and Structures in the Minimum Weight Design of a Supersonic transport Wing," AIAA 92-2372, *Proc.*, 33rd AIAA/ASME/AHS/ASC Strctures, Structural Dynamics, and Materials Conference, April 13-15, 1992, Dallas, Texas.

11. Grossman, B., Haftka, R. T., Kao, P. -J., Polen, D. M., Rais-Rohani, M. and Sobieszczanski-Sobieski, J., "Integrated Aerodynamic-Structural Design of a Transport Wing," *Journal of Aircraft*, Vol. 27, No. 12, 1990, pp. 1050-1056.

12. Shirk, M. H., Hertz, T. J. and Weisshaar, T. A., "Aeroelastic Tailoring - Theory, Practice, and Promise, " *Journal of Aircraft*, Vol. 23, January 1986, pp 6-18.

13. Johnson, E. H., Venkayya, V. B., "Automated Structural Optimization System, Volume I - Theoretical Manual," AFWAL-TR-88-3028, 1988, pp 102 and 177-179.

14. Haftka, R. T., Gürdal, Z. and Kamat, M. P., "*Elements of Structural Optimization,*" Kluwer Academic Publishers, Boston, 1990.

15. Chattopadhyay, A. and McCarthy, T., "Multiobjective Design Optimization of Helicopter Rotor Blades with Multidisciplinary Couplings," *Structural Systems and Industrial Applications*, Ed. S. Hernandez and C. A. Brebbia, 1991, pp. 451-461

16. Kreisselmeier, A. and Steinhauser, R., "Systemic Control Design by Optimizing a Vector Performance Index," *Proc.*, IFAC Symposium on Computer Aided Design of Control Systems, Zurich, Switzerland, 1979, pp. 113-117.

17. Wrenn, G. A., "An Indirect Method for Numerical Optimization Using the Kreisselmeier-Steinhauser Function," NASA CR-4220, 1989.

18. Fadel, G. M., Riley, M. F. and Barthelemy, J. F. M., "Two-Point Exponential Approximation Method for Structural Optimization," *Structural Optimization*, 2, 1990, pp. 117-124.

19. Seeley, C. E. and Chattopadhyay, A., "Development of a Hybrid Technique for Continuous/Discrete Optimization," *Proc.*, 6th AIAA/USAF/NASA/ISSMO Symposium on Multidisciplinary Analysis and Optimization, Bellevue, WA, Sept. 4-6, 1996.

20. Lynch, R. W., Rogers, W. A. and Brayman, W. W., "Aeroelastic Tailoring of Advanced Composite Structures for Military Aircraft," U. S. Air Force Flight Dynamics Lab. Rept. AFFDL-TR-76-100, April 1977.

21. Giles, G. L., "Equivalent Plate Analysis of Aircraft Wing Box Structures with General Planform Geometry," *Journal of Aircraft*, Vol. 23, No. 11, 1986, pp. 859-864.

22. Giles, G. L., "Further Generalization of an Equivalent Plate Representation for Aircraft Structural Analysis," *Journal of Aircraft,* Vol. 26, No. 1, 1989, pp. 67-74.

23. Livne, E., Schmit, L. A. and Friedmann, P. P., "Integrated Structure/Control/Aerodynamic Synthesis of Actively Controlled Composite Wings," *Journal of Aircraft*, Vol. 30, No. 3, 1993, pp. 387-394.

24. Reddy, J. N., "*Energy and Variational Methods in Applied Mechanics,*" Chapters 2 and 4, John Wiley & Sons, New York, 1984.

25. Livne, E., "Recent Developments in Equivalent Plate Modeling for Wing Shape Optimization," AIAA 93-1647, *Proc.*, 34th Structures, Structural Dynamics, and Materials Conference, La Jolla, CA, April 19-22, 1993, pp. 2998-3011.

26. Livne, E., Sels, R. A. and Bhatia, K. G., "Lessons from Application of Equivalent Plate Structural Modeling to an HSCT Wing," *Journal of Aircraft*, Vol. 31, No. 4, 1994, pp. 953-960.

27. McCarthy, T. R., "A New Higher-Order Composite Theory for Analysis and Design of High Speed Tilt-Rotor Blades," NASA CR 196703, October 1996.

28. McCarthy, T. R. and Chattopadhyay, A., "A Refined Higher-Order Composite Box Beam Theory," *Composites Part B* **28B** (1997), pp.523-534.

29. McCarthy, T. R. and Chattopadhyay, A., "Investigation of Composite Box Beam Dynamics Using a Higher-Order Theory," *Composite Structures*, 41(1998), pp. 273-284.

30. Reddy, J. N., "A Simple Higher-Order Theory for Laminated Composite Plates," *Journal of Applied Mechanics*, Vol. 51, December 1984, pp. 745-752.

31. Bhatia, K. G. and Wertheimer, J., "Aeroelastic Challenges for a High Speed Civil Transport," AIAA-93-1478-CP.

32. Chen, P. C., Lee, H. W. and Liu, D. D., "Unsteady Subsonic Aerodynamics for Bodies and Wings with External Stores Including Wake Effects," Journal of Aircraft, Vol. 30, No. 5, 1993, pp. 618-628.

33. Bisplinghoff, R. L., Ashley, H. and Halfman, R. L., "*Aeroelasticity,*" Chapters 3 and 5, Addison-Weslwy Publishing Co., Inc., Cambridge, 1955.

34. Karpel, M., "Design for Active and Passive Flutter Suppression and Gust Alleviation," NASA CR 3482, 1981.

35. Roger, K. L., "Airplane Math Modeling Methods for Active Control Design," Structural Aspects of Active Controls, AGARD-CP-228, August 1977, pp. 4.1-4.11.

36. Abel, I., "An Analytical Technique for Predicting the Characteristics of a Flexible Wing Equipped With an Active Flutter-Suppression System and Comparison With Wind-Tunnel Data," NASA TP-1367, 1979.

37. Vepa, R., "Finite State Modeling of Aeroelastic Systems," NASA CR-2779, 1977.

38. Tiffany, S. H. and Adams, W. M., Jr., "Nonlinear Programming Extensions to Rational Function Approximation Methods for Unsteady Aerodynamic Forces," NASA TP 2776, July 1988.

39. von Kármán, T., "Turbulence and Skin Friction," *Journal of the Aeronautical Sciences*, Vol. 1, No. 1, 1934, pp. 1-20.

40. Raymer, D. P., "*Aircraft Design: A Conceptual Approach*," Chapter 12, AIAA, Washington, D. C., 1989.

41. Shevell, R. S., "*Fundamentals of Flight*," Chapter 12, 2nd ed., Prentice-Hall, Englewood Cliffs, NJ, 1989.

42. Gallman, J. W., Kaul, R. W., Chandrasekharan, R. M. and Hinson, M. L., "Optimization of an Advanced Business Jet," *Journal of Aircraft*, Vol. 34, No. 3, May-June 1997, pp. 288-295.

43. Chopra, I., "Review of Current Status of Smart Structures and Integrated Systems," *Proc.*, SPIE Vol. 2717, SPIE's 3rd Annual International Symposium on Smart Structures and Materials, 1996, pp. 20-62.

44. Weisshaar, T. A., "Aeroservoelastic Control Concepts with Active Materials", *Proc.*, International Mechanical Engineering Congress and Exposition, Chicago, IL, Nov. 1994.

45. Heeg, J., "An Analytical and Experimental Investigation of Flutter Suppresssion via Piezoelectric Actuation", *Proc.*, AIAA 33rd Dynamics Specialists Meeting, Washington D.C., pp. 237-247, 1992.

46. Song, O., Librescu, L. and Rogers, C. A., "Application of Adaptive Technology to Static Aeroelestic Control of Wing Structures" *AIAA Journal*, Vol. 30, No. 12, pp. 2882-2889, December 1992.

47. Paige, D. A., Scott, R. C. and Weisshaar, T. A., "Active Control of Composite Panel Flutter Using Piezoelectric Materials" *Proc.*, SPIE's 1993 North American Conference on Smart Materials and Structures, Albuquerque, NM, Feb. 1-4, 1993

48. Crawley, E. F. and Lazarus, K. B., "Induced Strain Actuation of Isotropic and Anisotropic Plates" *AIAA Journal*, Vol. 29, No. 5, June 1991, pp. 944-951.

49. Chattopadhyay, A. and Seeley, C. E., "A Higher Order Theory for Modeling Composite Laminates with Induced Strain Actuators" *Composites Part B* (accepted for publication).

50. Seeley, C. E., "Analysis and Optimization of Smart Composite Structures Including Debonding," Ph. D. Thesis, Arizona State University, May 1997.

51. Lim, K. B. and Gawronski, W., "*Control and Dynamic Systems*," Vol. 57, Academic Press Inc, 1993, Actuator and Sensor Placement for Control of Flexible Structures.

52. Nam, C., Kim, Y. and Weisshaar, T. A., "Optimal Sizing and Placement of Piezo Actuators for Active Flutter Supression," SPIE Vol. 2443, SPIE's 2nd Annual International Symposium on Smart Structures and Materials, 1995, pp. 40-51.

53. Chen, G., Bruno, R. J. and Salama, M., "Optimal Placement of Active/Passive Members in Truss Structures Using Simulated Annealing" *AIAA Journal*, Vol. 29, No. 8, pp. 1327-1334, 1991.

54. Rao, S. S., Pan, T. and Venkayya, V. B., "Optimal Placement of Actuators in Actively Controlled Structures Using Genetic Algorithms," *AIAA Journal,* Vol. 29, No. 6, pp. 942-943, 1991.

55. Chattopadhyay, A., Seeley, C. E. and Jha, R., "Aeroelastic Tailoring Using Piezoelectric Actuation and Hybrid Optimization," *Smart Materials and Structures*, February 1999.

56. Zhou, S. W. and Rogers, C. A., "Power Flow and Consumption in Piezoelectrically Actuatuated Structures" *AIAA Journal*, Vol. 33, No. 7, July 1995.

57. Glassman, A. J., "Turbine Design and Application," Vols. 1 and 2, NASA SP 290, 1972.

58. Wilson, D. G. and Korakianitis, T., "*The Design of High-Efficiency Turbomachinery and Gas Turbines*," Chapter 7, Second Edition, Prentice Hall, New Jersey, 1998.

59. Meauze, G., "Overview on Blading Design Methods," in "Blading Design for Axial Turbomachines," AGARD Lecture Series 167, 1989.

60. Vanderplaats, G. N.,"*Numerical Optimization Techniques for Engineering Design: with Applications*," McGraw-Hill, New York, 1984.

61. Burgreen, G. W. and Baysal, O., "Three-Dimensional Aerodynamic Shape Optimization of Supersonic Delta Wings," AIAA-94-4271, 1994.

62. Chattopadhyay, A., Pagaldipti, N. and Chang, K. T., "A Design Optimization Procedure for Efficient Turbine Airfoil Design," *Computers and Mathematics with Applications*, Vol. 26, No. 4, 1993, pp. 21 - 31.

63. Narayan, J. R.,. Chattopadhyay, A., Pagaldipti, N. and Zhang S., "Integrated Aerodynamic and Heat Transfer Optimization Procedure for Turbine Blade Design," AIAA Paper No. 95-1479, *Proc.*, 35th AIAA/AHS/ASCE/ASME Structures, Structural Dynamics and Materials Conference, New Orleans, Louisiana, April 1995.

64. Goel, S., Cofer, J. I. and Singh, H., " Turbine Airfoil Design Optimization," ASME Paper 96-GT-158, *Proc.*, International Gas Turbine and Aeroengine Congress and Exposition, June 13-16, 1996, Birmingham, UK.

65. Farin, G., "*Curves and Surfaces for Computer Aided Geometric Design: A Practical Guide*," Chapter 4, Third Edition, Academic Press, Inc., 1993.

66. Chima, R. V., "Explicit Multigrid Algorithm for Quasi-Three-Dimensional Viscous Flows in Turbomachinery," *Journal of Propulsion and Power,* Vol. 3, No. 5, Sept. - Oct. 1987, pp. 397-405.

67. Chima, R. V., Turkel, E. and Schaffer, S., "Comparison of Three Explicit Multigrid Methods for the Euler and Navier-Stokes Equations," NASA TM-88878, January 1987.

68. Sorenson, R. L., "A Computer Program to Generate Two-Dimensional Grids About Airfoils and Other Shapes by Use of Poisson's Equations," NASA TM-81198, 1980.

69. Steger, J. L. and Sorenson, R. L., "Automatic Mesh Point Clustering Near A Boundary in Grid Generation with Elliptic Partial Differential Equations," *Journal of Computational Physics*, Vol. 33, No. 3, Dec. 1979, pp. 405-410.

70. Reddy, J. N., "*Mechanics of Laminated Composite Plates, Theory and Analysis*," Chapter 5, CRC Press, Inc., Boca Raton, Florida, 1997.

71. "Documentation of ZONA61 Code, Version C," ZONA 91-8.3, Zona Technology Inc., Mesa, Arizona, October 1994.

72. Hoadley, S. T., Adams, W. M., Jr. and Silva, W. A., "ISACv5 - Interaction Structures, Aerodynamics, and Controls," Version 5.3 User's Manual, NASA TM - 100666, April 1994.

73. Szu, H. and Hartley, R., "Fast Simulated Annealing," *Physical Letters A*, Vol. 122, No. 3, June 1987, pp. 157-162.

74. Chattopadhyay, A., Zhang, S. and Jha, R., "Structural and Aeroelastic Analysis of Composite Wing Box Sections Using Higher-Order Laminate Theory," AIAA 96-1567, *Proc.*, 37th AIAA/ASME/ASCE/AHS/ASC Structures, Structural Dynamics and Materials Conference, Salt Lake City, UT, April 15-19, 1996.

75. Jha, R. and Chattopadhyay, A., "Development of a Comprehensive Aeroelastic Analysis Procedure for Composite Wings Using Laplace Domain Methodology," AIAA 97-1026, *Proc.*, 38th AIAA/ASME/ASCE/AHS/ASC Structures, Structural Dynamics and Materials Conference, Kissimmee, FL, April 7-10, 1997.

76. Jha, R. and Chattopadhyay, A., "Aeroelastic Stability of Composite Wings Using Higher-Order Laminate Theory," *Mathematical Problems in Engineering* (submitted).

77. Chattopadhyay, A., Jha, R. and Seeley, C. E. "Application of Hybrid Optimization Technique for Improved Aeroelastic Performance of Composite Wings," AIAA 96-4015, *Proc.*, Sixth AIAA/NASA/USAF Symposium on Multidisciplinary Analysis and Optimization, Bellevue, WA, September 4-6, 1996.

78. Chattopadhyay, A., Seeley, C. E. and Jha, R., "Aeroelastic Tailoring Using Piezoelectric Actuation and Hybrid Optimization," *Smart Materials and Structures*, February 1999.

79. Jha, R. and Chattopadhyay, A., "Multidisciplinary Optimization of Composite Wings Using Refined Structural and Aeroelastic Analysis Methodologies," *Engineering Optimization* (in press).

80. Jha, R. and Chattopadhyay, A., "Smart Composite Wing Design for Optimal Aeroelastic Control," AIAA 99-1514, *Proc.*, 40th AIAA/ASME/ASCE/AHS/ASC Structures, Structural Dynamics and Materials Conference, St. Louis, MO, April 12-15, 1999.

81. Agarwal, B.D. and Broutman, L. J., "*Analysis and Performance of Fiber Composites*," John Wiley and Sons, Inc., 1990, p. 437.

82. E. H. Dowell, (ed.), "*A Modern Course in Aeroelasticity*," Chapter 3, Kluwer Academic Publishers, The Netherlands, 1995.

83. Weisshaar, T. A. and Foist, B. L., "Vibration and Flutter of Advanced Composite Lifting Surfaces," *Proc*, AIAA/ASME 24th Structures, Structural Dynamics, and Materials Conference, May 1983, pp. 498-508.

84. Tsai, S. W. and Wu, E. M., 1971, "A General Theory of Strength for Anisotropic Materials," *Journal of Composite Materials,* 5, pp. 58-80.

85. Chima, R. V. and Yokota, J. W., "Numerical Analysis of Three-Dimensional Viscous Internal Flows," *AIAA Journal*, Vol. 28, No. 5, May 1990, pp. 798-806.

86. Talya, S. S., Rajadas, J. N. and Chattopadhyay, A., "Multidisciplinary Design Optimization of Film-Cooled Gas Turbine Blades," Seventh AIAA/ASME Joint Thermophysics Conference, Albuquerque, NM, July 10-14, 1998.

87. Jha, R., Chattopadhyay, A. and Rajadas, J. N., "Shape Optimization of Turbomachinery Airfoil ," *Engineering Optimization* (submitted).